Casting light on
the η Carinae puzzle

Proefschrift

door

Nicola Clementel

geboren te Iringa, Tanzania
in 1984

Alla mia famiglia

The greater is the circle of light,
the greater is the boundary of the darkness
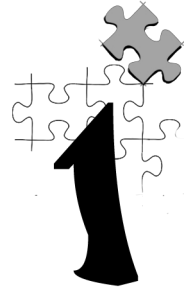*by which it is confined.*
(Joseph Priestley 1781)

Contents

Introduction

The massive binary star Eta Carinae is one of the most fascinating and intensely observed stellar systems in our galaxy. It attracted significant interest in 1837 when its luminosity started fluctuating between magnitude one and zero, briefly turning in March 1843 and January 1845 into the second brightest extra solar system object in the sky. Instead of rapidly fading, the system remained bright for over a decade, and during this event, known as the 'Great Eruption', the bipolar 'Homunculus' nebula was ejected (Figure 1.1). What caused the Great Eruption and the total mass of the Homunculus are only two of the many unanswered questions regarding Eta Carinae.

Over the last two decades, observations and theoretical models have shown evidences that deep inside the Homunculus is a colliding wind binary with a highly eccentric orbit. The extreme luminosity of the system, and the fact that an event of the magnitude of the Great Eruption did not destroy the central star, make Eta Carinae one of the most massive stars in the Galaxy. Several questions concerning the binary system also remain unanswered. What is the total mass of the inner binary system? How did it obtain such an eccentric orbit? What are the orbital parameters and orientation? What are the physical proprieties of the currently-unseen secondary star? What is the influence of the companion on events like the Great Eruption or the current observed time-varying events?

However, the interest in Eta Carinae goes beyond answering these specific questions and provides, for example, an excellent opportunity to study very massive stars. Due to its large variability over time, the primary is considered an extreme example of an evolved massive star called a Luminous Blue Variables (LBV). These massive stars are extremely rare and short-lived, and the relative proximity of Eta Carinae makes it possible to obtain high-quality data that can be used to test and constrain theoretical models. Eta Carinae is likely a supernova progenitor, a possible future gamma-ray burster, and the Great Eruption makes it a candidate supernova impostor. Thus, Eta Carinae provides an unique astrophysical laboratory for the study of star formation and evolution, stellar mass-loss, colliding wind binaries, stellar atmospheres, dust formation, and the chemical enrichment

of the surrounding interstellar medium.

Before further describing Eta Carinae in more detail we briefly summarize some of the relevant aspects of massive stars, binaries, and colliding winds.
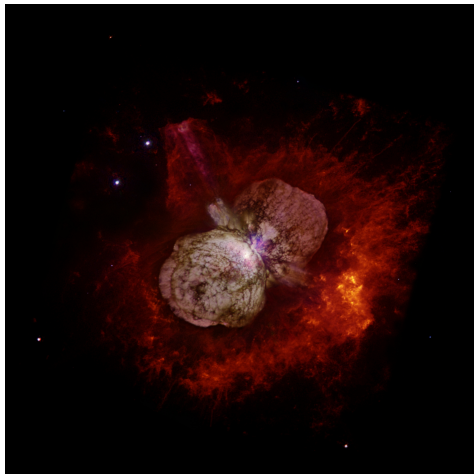
Figure 1.1 – Hubble Space Telescope (Wide Field and Planetary Camera 2) image of Eta Carinae obtained trough a combination of red and near-ultraviolet filters. The image is showing the massive bipolar Homunculus nebula which enshrouds the binary system. Credit: Nathan Smith (University of California, Berkeley), and NASA.

1.1   Massive stars

Stars with masses greater than ten, and up to several hundred solar masses, are referred to as massive stars. Despite the fact that these stars are rare and short lived (a few million years) they play a dominant role in the evolution of the interstellar medium and of the hosting galaxies. Massive stars possess really high luminosities ($L \propto M$; for $M > 20$ M$_\odot$) and, being hot stars for most of their life ($T \gtrsim 10^4$ K), they emit a large number of ionizing photons. Their high luminosity is also the source of powerful radiatively driven stellar winds. During their entire life, and even with their violent death, they enrich the surrounding gas with heavy elements synthesized in the stellar interior. Despite their predominant role both in the kinetics and the chemical evolution of the interstellar medium and galaxies, through massive outflows, UV radiation, stellar winds and, in the end, supernova explosions, our knowledge of the formation and evolution of massive stars is still limited.

1.1.1   Binarity

One of the key factors that influences the evolution and final fate of massive stars is the presence of a companion. The possible binary interaction modes between two stars, such

as tides, stratification changes, winds, mass transfer, or merging, appear to play a special role in the key parameters in the evolution of a star such as rotation, chemical mixing, ionizing flux, and lifetime.

In recent decades, it has become evident that the majority of massive stars are born in binary systems. Recent studies on star populations of nearby Galactic open stellar clusters show that $\sim 71\%$ of all O-type stars born interact with a companion, with more than half of these interactions occurring during the main sequence. A direct consequence of this is that the population of massive stars, even a high percentage of those that currently appear to be single stars, are the product of stellar mergers and binary mass transfer.

Binary interaction is currently one of the favoured mechanisms for a variety of exotic phenomena that encompass a wide range of wavelengths, physical scales and energies. X-ray binaries, millisecond pulsars, gamma-ray bursts, novae, supernovae and formation and shaping of aspherical planetary nebulae are some of the possible outcomes of binary interaction.

1.1.2   Colliding winds

Due to their high luminosities, massive stars possess powerful radiation driven stellar winds. As expected, if the stars are in a binary system and sufficiently close to each other, we have a colliding wind binary. The collision of the two outflows creates a wind–wind interaction region (WWIR) with a complex structure that depends on the wind and orbital parameters, and might vary strongly over the orbit of the system.

In a simple description, as long as the stars are far enough apart that their winds reach terminal speed before they collide, the location and shape of the WWIR is determined by the momentum balance of the two winds. The two winds collide where their wind momentum fluxes, or ram pressures, are equal. If the two stellar winds are unequal, the interaction region will be bent and pushed toward the star with the weaker wind in a cone-like shape (Figure 1.2). The larger the difference between the two winds, the smaller the cone opening angle, and the closer its apex to the weaker-wind star.

Numerous effects such as radiative inhibition (i.e weakening of the initiation of the stellar wind by the companion's radiation) and radiative braking (i.e. sudden deceleration of the wind by the companion's radiation) affect the WWIR structure, temperature, position, or even its existence.

Thermalization of the kinetic energy in the shocks on each side of the contact discontinuity heats the post-shock gas to temperatures $> 10^6$ K, entering the X-ray radiation regime. This emission is strongly affected by factors like the orbital parameters of the binary, the mass loss rates of the stars, and the material interposed between us and the shocked region.
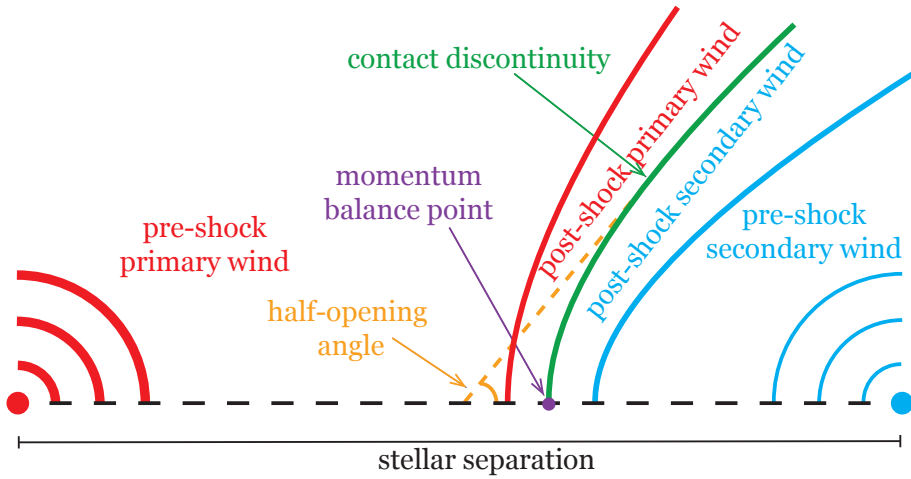
Figure 1.2 – Schematic of a colliding wind binary for a system in which the primary wind (red) is stronger than that of the secondary (light-blue). Along the line of centers (dashed black line), the contact discontinuity occurs at the momentum balance point (purple). Away from this axis, the contact discontinuity (green line) bends toward the secondary star, approaching an asymptotic half-opening angle (orange). Both the momentum balance points and the opening angle depend on the properties of the winds. The location of both primary and secondary pre- and post-shock winds are highlighted.

1.2   Eta Carinae

The Homunculus and its possible formation mechanisms have fascinated astronomers for decades and focused a lot of attention on Eta Carinae. Ironically, this spectacular bipolar nebula is now enshrouding the powerful central source, making any direct observation of the stellar system impossible. Nevertheless over the last decade, a huge effort, both on the observational and the modeling side, has been made in order to uncover Eta Carinae's secrets.

Eta Carinae is considered one of the most luminous and massive binary systems ($L \sim 5 \times 10^6$ L$_\odot$, $M > 100$ M$_\odot$). Its extreme luminosity and the modeling of *Hubble Space Telescope*/Space Telescope Imaging Spectrograph (*HST*/STIS) observations suggest that the primary star (η_A) is an LBV with a current mass $\gtrsim 90$ M$_\odot$. η_A has a powerful radiation-driven stellar wind with mass-loss rate $\dot{M}_{\eta_A} \approx 8.5 \times 10^{-4}$ M$_\odot$ yr^{-1} and terminal velocity $v_\infty \approx 420$ km s^{-1}.

Extensive X-ray monitoring with the Chandra X-ray Observatory and the Rossi X-ray Timing Explorer (RXTE) show periodic 5.54-yr variations in the X-ray light curve (see Figure 1.3). These observations and their modelling provide crucial pieces of evidence for the binary hypothesis, and help constrain the physical parameters of the system and the companion. The sudden and dramatic variation in the X-ray flux is extremely difficult to explain with known variability mechanisms of a single star. Moreover, the observed
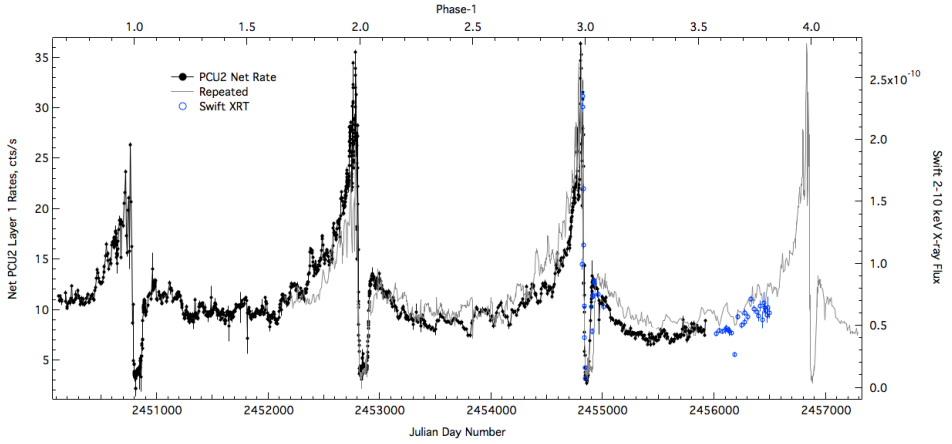
Figure 1.3 – The 2–10 keV RXTE light curve of Eta Carinae for the past three orbital cycles (in black). The grey line is an over-plot of the previous cycle. The data is phased according to a 2024 day ($\sim$ 5.54 yr) period. Credit: Michael Corcoran (NASA/GSFC).

very hard X-rays (2–10 keV) can only form in regions of extremely high temperature. The shocks produced by single stars are not strong enough to generate such X-ray flux. However, the shock-heated gas in the WWIR in colliding wind binaries can reach the necessary temperatures. The RXTE data support the presence of a companion star and also constrain one extremely important parameter of the system. In order to explain the behaviour of the 5.54-yr X-ray flux cycle, the binary system should have a high eccentricity of $e \sim 0.9$ and, as a consequence, a semimajor axis of $\sim$ 15.45 au.

The secondary star has never been directly observed due to the immense brightness of $\eta_{\rm A}$. Therefore, many of its properties are still uncertain. It is thought to be a $\sim$ 30 M$_\odot$ O5 or Wolf-Rayet star with a much faster ($v_\infty \approx 3000 \, {\rm km \, s}^{-1}$), but much lower density ($\dot{M}_{\eta_{\rm B}} \approx 10^{-5}$ M$_\odot$ yr^{-1}) wind compared to that of $\eta_{\rm A}$. The collision and interaction of these stellar winds together with the photoionization by the luminous stars generates several phase-dependent periodic variations observed at multiple wavelengths throughout the entire orbital period.

The ground-based spectrum of Eta Carinae is extremely complex and variable. It consists of a mix of broad and narrow, permitted and forbidden emission lines, some of them displaying P Cygni absorption profiles. Together, the central star and surrounding ejecta produce more than 2000 identified emission lines. Observations with *HST*/STIS also identify spatially extended, velocity-resolved forbidden emission lines from low- and high-ionization species. These lines provide information about different regions and structures within the system, going from the wind of the stars and the WWIR up to the intrinsic emission from the Homunculus nebula. The broad emission lines are mostly formed in the winds of the central object, while the narrow lines are principally from the slow-moving, dense ejecta surrounding the system. The P Cygni absorption components play a particu-

5

larly important role since they sample material in a narrow beam along our line-of-sight to the emitting region. They change with time as the source moves due to the binary orbit and/or because the absorbing material changes its state of excitation.

The global variability of the spectrum can be divided in two main phases. Around apastron, the WWIR has an almost axisymmetric conical shape (see Figure 1.4). For most of the 5.54 yr period η_B, the main source of hard ionizing photons, strongly contributes to the ionization of the system. Most of the X-rays and ionizing photons are able to escape through the less dense secondary wind. This phase is called the 'spectroscopic high state'. Approaching periastron, the orbital speed of η_A relative to η_B increases to a value close to η_A's wind speed. The small stellar separation at periastron causes η_B to become deeply embedded in η_A's dense inner wind and also prevents η_B's wind from reaching its terminal speed before colliding with η_A's wind. The above effects highly distort the WWIR and can lead to a possible 'collapse' of the WWIR apex. This period, during periastron passage and for several months after, is referred to as the 'spectroscopic low state'. In this phase the observed ionization of the system is due mostly to radiation from η_A.
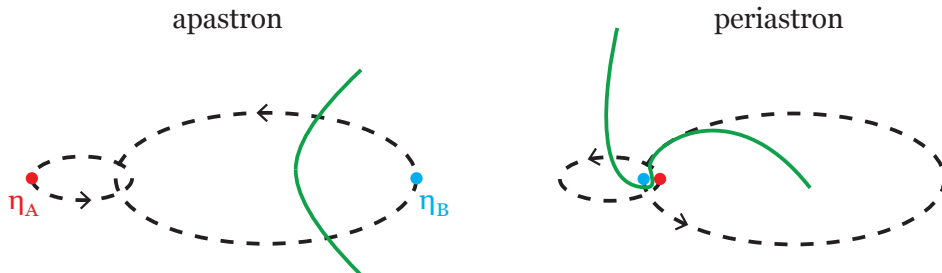
Figure 1.4 – Schematic of the elliptical orbit of the two stars in a binary system. The green line shows the shape of the WWIR at apastron (on the left-hand) and periastron (on the right-hand).

A key feature of the system is the observer's line of sight to the binary. The high eccentricity yields little phase variation for most of the orbit, forcing us to view the system through the same wind for a majority of the orbital period. Since the primary and secondary winds are very different, and the system is highly non-axisymmetric close to periastron, Eta Carinae's perceived observational properties are significantly affected by the location of the observer's line of sight.

Eta Carinae's high eccentricity requires full 3D hydrodynamical and radiative transfer simulations to accurately model the WWIR evolution and to properly compute the effects of the stars ionizing flux.

1.3   Tools

1.3.1   Hydrodynamics

The simulation of colliding winds in binary stars can be done using two different hydrodynamic methods: grid-based hydrodynamics and smoothed particle hydrodynamics (SPH). Both approaches have advantages and disadvantages, whose description is beyond the scope of this work. We will simply highlight why the SPH method was chosen to simulate Eta Carinae's colliding winds.

The main argument in favour of SPH over a grid-based code is the very large dynamical range needed to properly model Eta Carinae. With the aim of modelling the various observed lines, especially the high-ionization forbidden emission lines observed with *HST*/STIS, a computational domain of ~ 3000 au is needed. Furthermore, the high eccentricity causes the distance between the two stars to drastically change along the orbit. At apastron, the stellar separation is ≈ 29 au, while at periastron it is only ≈ 1.5 au. Therefore, in order to properly resolve the stars and colliding wind shocks, but also larger scale structures, a really high number of grid cells in each dimension would be needed. Simulations on this scale with current computational resources are extremely challenging, if not impossible with a reasonable resolution or amount of time on a grid-based code. Being less computationally expensive and naturally adaptive, SPH provides the resolution and computational domain size needed for the modeling of Eta Carinae within a reasonable time frame.

1.3.2   Radiative transfer

Before reaching our eyes or telescopes, the light from stars has to travel trough the interstellar medium and earth's atmosphere. Along the way it interacts with gas and dust, being absorbed and re-emitted, changing in direction and spectral characteristics. Therefore, the light carries not only information on its original source, but also on the material with which it interacts. The importance of emission and absorption of light for many astrophysical problems requires a proper understanding and modelling of the radiative transfer (RT) processes of ionizing photons.

In a 3D space, the RT equation is described by seven variables: three spatial, two angular, one frequency, and one time variable. Even if for specific applications some simplifications can be made on the geometry or on the time and frequency dependence, analytical treatments are basically impossible. Therefore, in order to solve problems requiring complex radiative transfer, it is necessary to use numerical methods. Only in the last decade have computational capabilities reached the level to allow the implementation of the RT equation in numerical codes.

To model the effects of the ionizing photons produced by the luminous stars in Eta Carinae on the surrounding gas, we use the SimpleX algorithm. This method uses a Voronoi-Delaunay unstructured grid as its computational mesh. The scale-free and natural

adaptive resolution of the mesh make SIMPLEX suited to study the RT in a complex system like Eta Carinae. The local nature of the Delaunay transport make it also computationally affordable.

1.3.3 3D printing

Multi-dimensional hydrodynamical or RT simulations play an extremely important role in increasing our understanding of Eta Carinae, as well as many other astrophysical problems. The difficulties connected with the modelling of these complex systems are not solely connected to their numerical aspects. Properly visualizing complicated 3D numerical simulation output is a challenge by itself.

The use of interactive 3D graphics and 3D printing started to appear in the astronomical community over the past few years. Observational data were used to create a 3D printable model that helped in the understanding of complex objects (e.g. the Homunculus nebula). The ability to physically interact with 3D printed models also creates new possibilities to present and explain observations and results from numerical simulations of astrophysical phenomena to non-experts, non-scientists and even the blind or visually-impaired.

1.4 This thesis

The numerous emission and absorption lines observed in Eta Carinae and their time-dependent variability are key to understanding the geometry and parameters of the binary system, as well as the physical proprieties of the individual stars. Information about the ionization state of the gas, and therefore where the lines form, is essential to properly model these lines. In this thesis we post-process 3D SPH simulations of Eta Carinae's interacting winds by means of the SIMPLEX RT algorithm, creating ionization maps of hydrogen and helium. We also present 3D prints of output from SPH simulations of Eta Carinae's inner WWIR at multiple orbital phases.

Chapter 2 presents the SIMPLEX RT algorithm and the methods used for post-processing 3D SPH simulations of Eta Carinae's interacting winds. We show initial results from full 3D radiative transfer simulations computing the ionization fractions of hydrogen and helium assuming different primary mass-loss rates. The importance of including collisional ionization to achieve a better description of the ionization states is also discussed. We investigate the effects of reducing the primary mass-loss rate on areas where the observed forbidden emission lines form. Our results show that using SIMPLEX is a viable method to investigate the ionization state of the gas in complex colliding wind binaries like Eta Carinae.

In **Chapter 3** we focus on the ionization structure of helium during apastron, the spectroscopic high state. We present helium ionization maps of the inner 150 au of the system for different $\dot{M}_{\eta_A}$ mass-loss rates. The location and extent of the region of ionized He and how this might relate with available observations is discussed. Our simulations show that

lowering the primary mass-loss rate strongly affects the volume of He$^+$ in the pre-shock η_A wind on the periastron side of the system. Looking at our results, a binary orientation in which apastron is on our side of the system is more consistent with available observations. We also suggest that small variations in $\dot{M}_{\eta_A}$ might explain the observed increase in He I absorption in recent decades.

Chapter 4 follows directly from Chapter 3, but addresses the ionization structure of helium during periastron, the spectroscopic low state. We compute 3D helium ionization maps using the results from Chapter 3 as a guide for the initial conditions in order to achieve a better description of the ionization states at this important phase of the orbit. The extra complexities introduced by the highly asymmetric scenario and fast orbital motion are also discussed. We show that, with apastron on our side of the system, our results are qualitatively consistent with the observed variations in strength and radial velocity of the helium emission and absorption lines. Our results favour a scenario in which a combination of a wind-eclipse by η_A and a 'collapse' of the WWIR are responsible for the observed drop in the helium emission at periastron.

In **Chapter 5** we present the first 3D prints of SPH simulations of Eta Carinae's colliding winds. The methodology used to generate the 3D printable files and 3D interactive graphics is described. We demonstrate the benefit of using 3D visualization and 3D printing as tools to analyze output from numerical simulations. The identification of previously unknown physical features highlights the important role that 3D printing can play in the visualization and understanding of complex 3D time-dependent numerical simulations of astrophysical phenomena.

1.5 Future

The work described in this thesis lays the foundation for future work aimed at generating synthetic spectra for comparison to data obtained with *HST*/STIS as part of a multicycle programme to map changes in Eta Carinae's extended wind structures across one binary cycle from 2009 through 2015. Comparison of the observations to the models should ultimately lead to more accurate constraints on the binary orientation, $\dot{M}_{\eta_A}$, and η_B's luminosity and temperature. Our numerical work also sets the stage for future efforts to couple SimpleX with modern 3D SPH and grid-based hydrodynamics codes. The use of 3D time-dependent radiation-hydrodynamics simulations will allow one to more properly follow the ionization and recombination of the gas.

While this thesis focuses specifically on the case of Eta Carinae, the described numerical methods and future prospects can be applied to numerous other colliding wind binaries, dusty 'pinwheels', and similar systems of astrophysical interest. The study of these systems might provide answers to several important general questions. How can dust form and survive in such systems that usually contain a hot, luminous O star? What is the relation between binary interaction and the formation of bipolar outflows, supernovae, and gamma-ray bursts? What is the effect of mass transfer between binary companions in the

evolution and final fate of the stars?

In order to develop a better understanding of these phenomena, we need to combine reliable hydrodynamical and radiative transfer simulations with detailed observations. This is a perfect time for research of such complex radiation-hydrodynamical mechanisms. Modern supercomputers allow us to perform high-resolution simulations. On the observational side, large telescopes, for example ALMA, are providing new possibilities to study stellar outflows and binary interactions with an unprecedented level of detail.

3D radiative transfer in η Carinae: application of the SimpleX algorithm to 3D SPH simulations of binary colliding winds
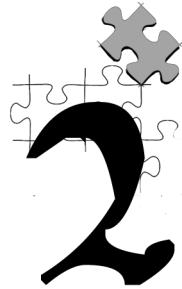
Eta Carinae is an ideal astrophysical laboratory for studying massive binary interactions and evolution, and stellar wind–wind collisions. Recent three-dimensional (3D) simulations set the stage for understanding the highly complex 3D flows in η Car. Observations of different broad high- and low-ionization forbidden emission lines provide an excellent tool to constrain the orientation of the system, the primary's mass-loss rate, and the ionizing flux of the hot secondary. In this work we present the first steps towards generating synthetic observations to compare with available and future *Hubble Space Telescope*/Space Telescope Imaging Spectrograph data. We present initial results from full 3D radiative transfer simulations of the interacting winds in η Car. We use the SimpleX algorithm to post-process the output from 3D smoothed particle hydrodynamics (SPH) simulations and obtain the ionization fractions of hydrogen and helium assuming three different mass-loss rates for the primary star. The resultant ionization maps of both species constrain the regions where the observed forbidden emission lines can form. Including collisional ionization is necessary to achieve a better description of the ionization states, especially in the areas shielded from the secondary's radiation. We find that reducing the primary's mass-loss rate increases the volume of ionized gas, creating larger areas where the forbidden emission lines can form. We conclude that post processing 3D SPH data with SimpleX is a viable tool to create ionization maps for η Car.

N. Clementel, T. I. Madura, C. J. H. Kruip, V. Icke and T. R. Gull

2.1   Introduction

Eta Carinae (η Car) is an extremely luminous ($L_{\text{Total}} \gtrsim 5 \times 10^6$ L$_\odot$) colliding wind binary with a highly eccentric (e $\sim$ 0.9), 5.54 yr orbit (Davidson & Humphreys 1997; Damineli, Conti & Lopes 1997; Hillier et al. 2001; Damineli et al. 2008a,b; Corcoran et al. 2010). η_{A}, the primary of the system, is our closest (2.3 ± 0.1 kpc; Smith 2006) example of a very massive star (~ 100 M$_\odot$; Davidson & Humphreys 1997). A luminous blue variable, η_{A} has an extremely powerful stellar wind with $\dot{M}_{\eta_{\text{A}}} \approx 8.5 \times 10^{-4}$ M$_\odot$ yr^{-1} and $v_\infty \approx 420$ km s^{-1} (Hillier et al. 2001, 2006; Groh et al. 2012a). Observations over the last two decades indicate that η_{A}'s dense stellar wind interacts with the hotter, less-luminous companion star η_{B} and its much faster ($v_\infty \approx 3000$ km s^{-1}, Pittard & Corcoran 2002), but much lower density ($\dot{M}_{\eta_{\text{B}}} \approx 10^{-5}$ M$_\odot$ yr^{-1}), wind (Damineli et al. 2008a; Corcoran et al. 2010; Gull et al. 2009, 2011). These wind–wind interactions lead to various forms of time-variable emission and absorption seen across a wide range of wavelengths (Damineli et al. 2008a).

Observational signatures that arise as a result of the wind–wind interactions are important for studying η Car as they provide crucial information about the physical properties of the as-yet unseen η_{B} and the system as a whole. Three-dimensional (3D) hydrodynamical simulations show that the fast wind of η_{B} carves a low-density cavity out of the slower, denser inner wind of η_{A} for most of the orbit (Okazaki et al. 2008; Parkin et al. 2011; Madura & Groh 2012; Madura et al. 2012, 2013; Russell 2013). The same simulations indicate that the hot post-shock gas in the inner wind–wind interaction region (WWIR) gives rise to hard (up to 10 keV) X-ray emission that varies over the 5.54 yr period. Together with the models, spatially unresolved X-ray (Hamaguchi et al. 2007; Henley et al. 2008; Corcoran et al. 2010), optical (Damineli et al. 2008a,b), and near-infrared (Whitelock et al. 2004; Groh et al. 2010b) observations have helped constrain the geometry and physical conditions within the inner WWIR.

In addition to the 'current' interaction between the two winds that occurs in the inner regions (at spatial scales comparable to the semi-major axis length $a \approx 15.4$ au $\approx$ 0.0067 arcsec at 2.3 kpc), larger scale (≈ 3250 au ≈ 1.4 arcsec in diameter) 3D hydrodynamical simulations exhibit outer WWIRs that extend thousands of au from the central stars (Madura et al. 2012, 2013, hereafter M12 and M13, respectively). Long-slit spectral observations of η Car with the *Hubble Space Telescope*/Space Telescope Imaging Spectrograph (*HST*/STIS) reveal these spatially-extended WWIRs, seen via emission from multiple low- and high-ionization forbidden lines (Gull et al. 2009, 2011; Teodoro et al. 2013).

Using a 3D dynamical model of the broad, extended [Fe III] emission observed in η Car by the *HST*/STIS, M12 confirmed the orbital inclination and argument of periapsis that Okazaki et al. (2008) and Parkin et al. (2009) derived using X-ray data. More importantly, M12 broke the degeneracy inherent to models based solely on X-rays or other spatially-unresolved data and constrained, for the first time, the 3D orientation of η Car's binary orbit. M12 find that the system has an argument of periapsis $\omega \approx 240°$–285°, with

the orbital axis closely aligned with the Homunculus nebula's polar axis at an inclination $i \approx 130°–145°$ and position angle on the sky PA $\approx 302°–327°$, implying that apastron is on the observer's side of the system and that η_B orbits clockwise on the sky. The dynamical model of M12 was based on 3D smoothed particle hydrodynamics (SPH) simulations of η Car's colliding winds. A simple radiative transfer (RT) code was used to integrate the optically thin [Fe III] emission and generate synthetic slit-spectra for comparison to the available *HST*/STIS data. Although very successful, M12 used a semi-analytic approach to compute the volume of wind material photoionized by η_B. Furthermore, the fraction of Fe^{2+} as a function of T was estimated assuming collisional ionization equilibrium and available ion fraction data. Due to the lack, at the time, of a suitable code, proper 3D RT simulations of η_B's ionizing radiation were not performed. The location and strength of the [Fe III] emission was thus based on geometrical criteria, while in reality, the population of forbidden states depends on the local ionization state of the medium.

The goal of this paper is to improve considerably the modelling approach of M12 by computing full 3D RT simulations of the effects of η_B's ionizing radiation on η Car's spatially-extended WWIRs. We accomplish this by applying the SIMPLEX algorithm for 3D RT on an unstructured Delaunay grid (Ritzerveld & Icke 2006; Ritzerveld 2007; Paardekooper, Kruip & Icke 2010; Paardekooper et al. 2011; Kruip et al. 2010) to recent 3D SPH simulations of η Car's binary colliding winds (M13). We use SIMPLEX to obtain detailed ionization fractions of hydrogen and helium at the resolution of the original SPH simulations. This should allow us to predict much more precisely where, and to what extent, various observed forbidden emission lines form. This paper lays the foundation for future work aimed at generating synthetic spectral data cubes for comparison to data obtained with *HST*/STIS as part of a multicycle programme to map changes in η Car's extended wind structures across one binary cycle from 2009 through 2015 (Gull et al. 2011; Teodoro et al. 2013). Comparison of the observations to the models should ultimately lead to more accurate constraints on the orbital, stellar, and wind parameters of the η Car system, such as η_A's mass-loss rate and η_B's temperature and luminosity (Mehner et al. 2010, 2012; M13).

While we focus specifically on the case of η Car, the numerical methods in this paper can be applied to numerous other colliding wind (e.g. WR 140, WR 137, WR 19; Fahed et al. 2011; Lefèvre et al. 2005; Williams, Rauw & van der Hucht 2009) and dusty 'pinwheel' (WR 104, WR 98a, Tuthill, Monnier & Danchi 1999; Monnier, Tuthill & Danchi 1999) binary systems. One of the biggest remaining mysteries is how dust can form and survive in such systems that contain a hot, luminous O star. Coupled with 3D hydrodynamical simulations, SIMPLEX simulations have the potential to help determine the regions where dust can form and survive in these unique objects.

In the following section, we describe our numerical approach, including the SPH simulations, the SIMPLEX code, and the RT simulations. Section 2.3 describes the results. A discussion of the results and their implications follows in Section 2.4. Section 2.5 summarizes our conclusions and outlines the direction for future work.

2.2 Codes and Simulations

2.2.1 The 3D SPH Simulations

The hydrodynamical simulations were performed with the same SPH code used in M13, to which we refer the reader for details. Optically thin radiative cooling is implemented using the Exact Integration Scheme of Townsend (2009), with the radiative cooling function $\Lambda(T)$ calculated using Cloudy 90.01 (Ferland et al. 1998) for an optically thin plasma with solar abundances. The pre-shock stellar winds and rapidly-cooling dense gas in the WWIR are assumed to be maintained at a floor temperature $= 10^4$ K due to photoionization heating by the stars (Parkin et al. 2011). The same initial wind temperature (T_{wind}) is assumed for both stars. The effect of T_{wind} on the flow dynamics is negligible (Okazaki et al. 2008).

Radiative forces are incorporated in the SPH code via an 'antigravity' formalism, the details of which can be found in M13 and Russell (2013). The individual stellar winds are parametrized using the standard 'beta-velocity law' $v(r) = v_\infty(1 - R_\star/r)^\beta$, where v_∞ is the wind terminal velocity, $R_\star$ the stellar radius, and β (set $= 1$) a free parameter describing the steepness of the velocity law. Effects due to 'radiative braking' (Gayley, Owocki & Cranmer 1997; Parkin et al. 2011), photospheric reflection (Owocki 2007), and self-regulated shocks (in which ionizing X-rays from the WWIR inhibit the wind acceleration of one or both stars, leading to lower pre-shock velocities and lower shocked plasma temperatures; Parkin & Sim 2013), are not included. These effects are not expected to play a prominent role in η Car at the orbital phases near apastron considered in this work (Parkin et al. 2009, 2011; Russell 2013; M13).We include the more important velocity-altering effects of 'radiative inhibition', in which one star's radiation field reduces the net rate of acceleration of the opposing star's wind (Stevens & Pollock 1994; Parkin et al. 2009, 2011). However, because we fix the mass-loss rates in our antigravity approach, possible changes to the mass-loss due to radiative inhibition are not included. These changes are not expected to be significant in η Car and should not greatly affect our results or conclusions (M13).

Using an *xyz* Cartesian coordinate system, the binary orbit is set in the *xy* plane, with the origin at the system centre of mass and the major axis along the *x*-axis. The two stars orbit counter-clockwise when viewed from the $+z$-axis. By convention, $t = 0$ ($\phi = t/2024 = 0$) is defined as periastron. Simulations are started at apastron and run for multiple consecutive orbits. Orbits are numbered such that $\phi = 1.5, 2.5$ and 3.5 correspond to apastron at the end of the second, third, and fourth full orbits, respectively.

The outer spherical simulation boundary is set at $r = 100\,a$ from the system centre of mass, where $a = 15.45$ au is the length of the orbital semimajor axis. Particles crossing this boundary are removed from the simulations. The computational domain is comparable in size to past and planned *HST*/STIS mapping observations of the interacting stellar winds in η Car's central core ($\sim \pm 0.67$ arcsec $\simeq \pm 1540$ au; Gull et al. 2011; M12; Teodoro et al. 2013). As demonstrated by Gull et al. (2011) and M12, 3D simulations at this scale

Table 2.1 – Stellar, wind, and orbital parameters of the 3D SPH simulations

Parameter	η_{A}	η_{B}	Reference
$M_\star$ ($\mathrm{M}_\odot$)	90	30	H01; O08
$R_\star$ ($\mathrm{R}_\odot$)	60	30	H01; H06
T_{wind} (10^4 K)	3.5	3.5	O08; M13
$\dot{M}$ (10^{-4} $\mathrm{M}_\odot\,\mathrm{yr}^{-1}$)	8.5, 4.8, 2.4	0.14	G12; P09
v_∞ ($\mathrm{km\,s}^{-1}$)	420	3000	G12; P02
P_{orb} (d)	2024		D08a
e	0.9		C01; P09
a (au)	15.45		C01; O08

Notes: $M_\star$ and $R_\star$ are the stellar mass and radius. T_{wind} is the initial wind temperature. $\dot{M}$ and v_∞ are the stellar-wind mass-loss rate and terminal speed, respectively. P_{orb} is the period, e is the eccentricity, and a is the length of the orbital semimajor axis.

References: C01 = Corcoran et al. (2001); H01 = Hillier et al. (2001); P02 = Pittard & Corcoran (2002); H06 = Hillier et al. (2006); D08a = Damineli et al. (2008b); O08 = Okazaki et al. (2008); P09 = Parkin et al. (2009); G12 = Groh et al. (2012a).

are necessary for understanding and modelling the extended, time-variable forbidden line emission structures that are spatially and spectrally resolved by *HST*/STIS.

The total number of SPH particles used in the simulations is roughly between 5×10^5 and 9×10^5, depending on the value of $\dot{M}_{\eta_{\mathrm{A}}}$. The adopted simulation parameters (Table 2.1) are consistent with those derived from the available observations, although there has been some debate on the exact present day value of $\dot{M}_{\eta_{\mathrm{A}}}$ (see M13 for details). In an effort to better constrain η_{A}'s current $\dot{M}$, M13 performed multiple 3D SPH simulations assuming different $\dot{M}_{\eta_{\mathrm{A}}}$. We use the same naming convention as M13 when referring to the simulations in this paper for the different $\dot{M}_{\eta_{\mathrm{A}}}$, namely, Case A ($\dot{M}_{\eta_{\mathrm{A}}}$ = 8.5×10^{-4} $\mathrm{M}_\odot\,\mathrm{yr}^{-1}$), Case B ($\dot{M}_{\eta_{\mathrm{A}}}$ = 4.8×10^{-4} $\mathrm{M}_\odot\,\mathrm{yr}^{-1}$), and Case C ($\dot{M}_{\eta_{\mathrm{A}}}$ = 2.4×10^{-4} $\mathrm{M}_\odot\,\mathrm{yr}^{-1}$). We discuss the effects of the three values of $\dot{M}_{\eta_{\mathrm{A}}}$ on the RT calculations in Section 2.3.2.

2.2.2   The SimpleX algorithm for RT on an unstructured mesh

The SimpleX algorithm, conceived by Ritzerveld & Icke (2006), implemented by Ritzerveld (2007), and further improved by Paardekooper, Kruip & Icke (2010) and Kruip et al. (2010), is designed to solve the general equations of particle transport by expressing them as a walk on a graph. At the basis of the method lies the unstructured grid on which the photons are transported. A given medium (e.g. a density or optical-depth field) is typically sampled with a Poisson point process and the resulting point distribution is used to tessellate space according to the Voronoi recipe: all points in a cell are closer to the nucleus of that cell than to any other nucleus. The Voronoi nuclei are then connected by a Delaunay triangulation. The grid is constructed to describe the properties of the underlying

physical medium, through which the photons travel, in such a way that more grid points are placed in regions with a higher opacity. The result is a higher resolution in places where it is needed most, i.e. where the optical depth is highest.

Photons are transported from node to node along the edges of the Delaunay triangulation, where each transition has a given probability. In one computational cycle, every nucleus in the grid transports its content to neighbouring nuclei, optionally absorbing or adding photons. Which neighbours are selected for transport depends on the specific process. Even though SimpleX was originally developed for application in cosmological RT, its properties are still well suited for our purpose.

In Section 2.2.2.1 we present the construction procedure for the SimpleX RT mesh starting from the SPH particle distribution. Section 2.2.2.2 describes the processes that determine the ionization state of the gas, such as collisional- and photo-ionization and recombination, plus the specifics of their implementation in SimpleX (for further details see chapters 4 and 5 of Kruip 2011).

2.2.2.1 Grid Construction

The 3D SPH simulations provide the time-dependent 3D density, temperature, and velocity structure of η Car's interacting winds on the spatial scales of interest, thus forming the basis of our model. As in M12, the RT calculations are performed as post-processing of the 3D SPH output. The hydrodynamic influence of the radiation on the gas is thereby neglected. We do not expect this to have a very large influence on the results since the material photoionized by η_B responds nearly instantaneously to its UV flux, i.e. the recombination time-scale is very small relative to the orbital time-scale, especially around apastron (M12).

The first step is to convert the SPH particle distribution to a SimpleX mesh. Since the density field is given by discrete particles, we might obtain an estimate of the density at any position in the domain using a typical SPH kernel function $W(r, h)$ with

$$\rho(r) = \sum_j m_j W(|r - r_j|, h_i) \tag{2.1}$$

where h is the smoothing length and m_j is the mass of particle j. Using this kernel function one can then sample the data using the sampling functions described in e.g. Paardekooper, Kruip & Icke (2010) and Kruip et al. (2010). However, given the fact that the original data are already particle-based, it is more natural for us to use the SPH particles themselves as the generating nuclei for the Voronoi-Delaunay mesh. This leads to a more direct estimate of the density, given by the division of the particle mass by the Voronoi volume of its corresponding cell. Another advantage is that, due to pressure forces, the particles in an SPH simulation are in general positioned more regularly than for a pure Poisson process. Finally, we note that with future applications of 3D time-dependent radiation-hydrodynamics in mind, a coupling of SimpleX with an SPH method is most natural when the radiation transport is applied directly to the SPH particles so that no spurious

interpolation is needed. For these reasons we use every SPH particle as the nucleus of a Voronoi cell. This procedure yields density estimates that are less smooth than those obtained with typical kernel functions of the type of Equation (2.1), but guarantees mass conservation and represents small scale structures in the density field more accurately.

Figure 2.1 presents an example of the resulting SimpleX mesh and number density at apastron for a typical 3D SPH simulation of η Car. The first row shows the original number density from the SPH simulation for slices in the *xy*, *xz*, and *yz* planes for the Case A simulation. The SimpleX mesh (second row) reproduces everywhere the features present in the original SPH data. The resulting SimpleX number density (third row) follows extremely well the SPH one in shape, resolution, and value.

Paardekooper, Kruip & Icke (2010) and Kruip et al. (2010) discussed how undersampling can have a negative effect on the outcome of an RT simulation that uses grid-based data. In principle, the same problem holds for particle-based data in areas where sharp gradients are present in the number density of SPH particles. To ensure that our results are not prone to such issues, we developed a method to increase the resolution of any sparsely sampled regions. We begin with the triangulation of the SPH particles. For every tetrahedron in this triangulation that is larger than a tolerance volume, an additional vertex is placed in the centre of the tetrahedron, and 1/5 of the mass of the four vertices that constitute the tetrahedron is given to the new vertex. This procedure is manifestly mass conserving and regularizes the mesh in low resolution regions.

To study the influence this procedure has on the RT results, we performed test RT simulations with and without resolution enhancements in normally sparsely-sampled regions. For these tests we used a characteristic η Car SPH simulation snapshot in which the densities span roughly ten orders of magnitude (i.e. the top row of Figure 2.1). If the RT results are sensitive to sharp gradients, we expect significant differences between the RT simulation with increased resolution and the original non-enhanced simulation.

Although the difference is not large, the overall density in the affected regions is slightly enhanced by the new interpolation. However, we find that the overall shape and spatial extent of the ionized regions does not change. The ionization fraction in the local region most affected by the increased resolution is somewhat lower after the procedure though. This is consistent with the notion that the interpolation increases slightly the density in the higher resolution region, resulting in a slightly higher recombination rate. The difference, however, is negligible. These results suggest that locally increasing the resolution does not change the overall shape and size of the ionized regions. We are therefore confident that our RT results are not susceptible to systematic effects related to strong gradients in the SPH particle number density (for further detail see chapters 3 and 4 of Kruip 2011).

2.2.2.2   Ionization State and Chemistry of the Gas

In a gas with cross-section for photoionization $\sigma(\vec{x}, \nu)$ at position $\vec{x}$, the local photoionization rate, $\Gamma_{P, i}(\vec{x})$ (which gives the number of photoionizations per second per
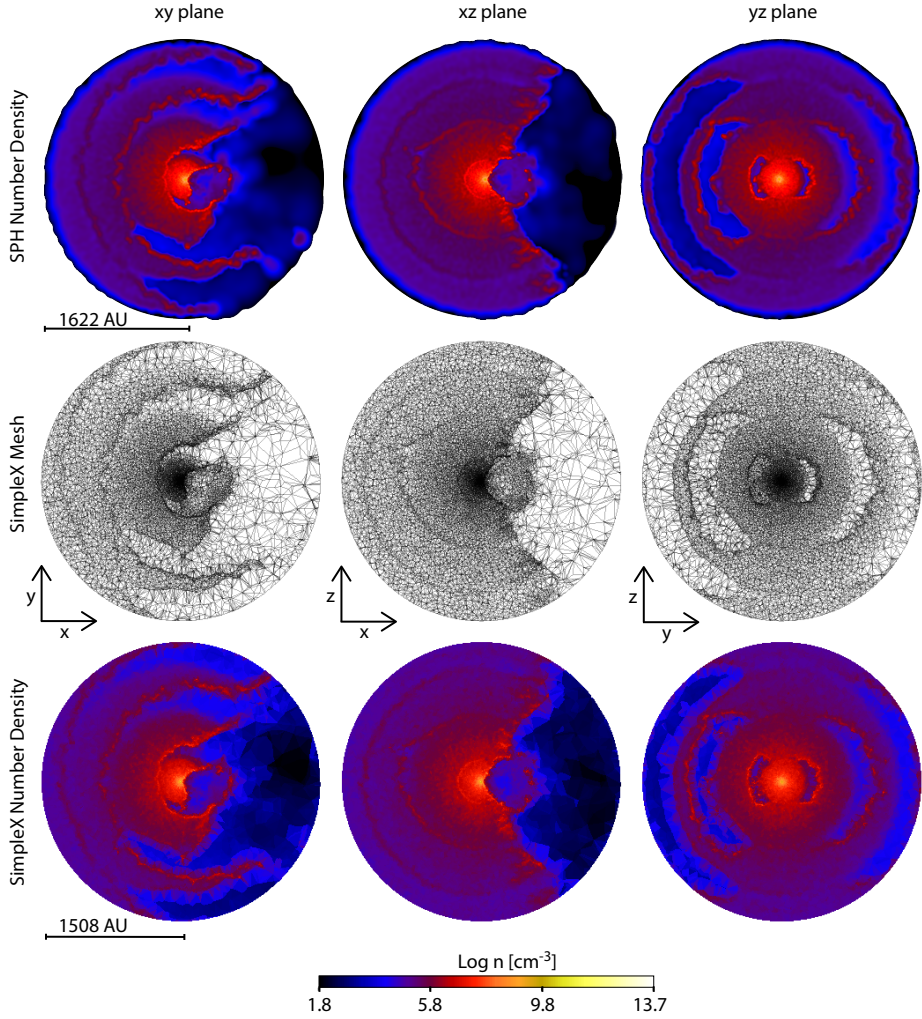
Figure 2.1 – Slices in the *xy* (left-hand column), *xz* (middle column) and *yz* (right-hand column) planes through the 3D simulation volume for the Case A simulation at apastron. Rows show, from top to bottom, the original SPH number density distribution (log scale, cgs units), the SIMPLEX mesh, and the resulting SIMPLEX number density (same log scale, cgs units). The resolution of the SIMPLEX mesh, as well the number density, follow well the resolution of the original SPH data. In the first column (i.e. the orbital plane) η_{A} is to the left and η_{B} is to the right. The length scales are shown under the top and bottom left-hand panels. Note that the domain size in the SIMPLEX snapshots is slightly smaller than that of the SPH simulations only because we have, for visualization purposes, removed the border points used to generate the SIMPLEX mesh.

atom of species i in units $[\,\mathrm{s}^{-1}\,]$), is given by (Osterbrock & Ferland 2006):

$$\Gamma_{P,\,i}(\vec{x}) \equiv \int_0^\infty \frac{4\pi J_\nu(\vec{x})}{h\nu} \sigma_i(\vec{x},\nu)\,\mathrm{d}\nu, \tag{2.2}$$

where $J_\nu(\vec{x})$ is the local mean intensity and the three species capable of absorbing ionizing photons in the code are H^{0+}, He^{0+} and He^+. For simplicity, we only consider the ionization of hydrogen and helium atoms. Implementing ionization processes in a numerical code requires that the relevant equations be expressed in a discretized form. In particular, we need to know the ionization rate per species in each cell of our computational grid. In SIMPLEX, ionizing radiation travels from cell to cell along the Delaunay edges. At the nucleus of each Voronoi cell, photons are taken away from the incoming radiation field and their energy is used to ionize the neutral atoms of that Voronoi cell. Given the number densities of these species ($n_{H^{0+}}$, $n_{He^{0+}}$ and n_{He^+}), and the path length through the cell l, the monochromatic optical depth of ionizing radiation τ_ν is

$$\tau_\nu \equiv (n_{H^{0+}}\sigma_{H^{0+}} + n_{He^{0+}}\sigma_{He^{0+}} + n_{He^+}\sigma_{He^+})l. \tag{2.3}$$

The total number of ionizations per unit time, $\dot{N}_{ion}$ for a cell with optical depth τ_ν is then given by

$$\dot{N}_{ion} = \int_0^\infty \dot{N}_\gamma(\nu)[1 - \exp(-\tau_\nu)]\, d\nu, \tag{2.4}$$

where $\dot{N}_\gamma(\nu)$ is the number of ionizing photons per unit time streaming into the cell. To quantify how much of the resulting ionizations is due to a particular species, we use the contribution to the total optical depth of that species. The number of ionizations of species i per unit time is

$$\dot{N}_{ion,\, i} = \dot{N}_{ion} \int_0^\infty \frac{\tau_{\nu,\, i}}{\tau_\nu}\, d\nu \tag{2.5}$$

Dividing by the number of neutral atoms of species i in the cell, N_i, then gives the spatially discretized equivalent of Equation (2.2)

$$\Gamma_{P,\, i} = \frac{\dot{N}_{ion,\, i}}{N_i}. \tag{2.6}$$

In numerical simulations involving radiation, it is often necessary to approximate the continuous spectrum of radiation with a finite number of discrete frequency bins due to memory requirements. The extreme (but often employed) limit of one single frequency bin is commonly referred to as the 'grey approximation'. Although in the grey approximation all spectral information is lost, it is still possible to enforce the conservation of a quantity of importance such as the number of ionizations per unit time or the energy deposition into the medium per unit time. For simplicity, we employ the grey approximation in this work.

The conservation of ionizations is accomplished by defining the effective cross-section for species i, $\sigma_{I,\, i}$, as

$$\sigma_{I,\,i} = 4\pi \int_0^\infty \frac{\sigma_i(\nu) J_\nu}{h\nu} \, \mathrm{d}\nu \Big/ \dot{N} \tag{2.7}$$

where $\dot{N}$ is the rate of ionizing photons per surface area defined by

$$\dot{N} \equiv 4\pi \int_0^\infty \frac{J_\nu}{h\nu} \, \mathrm{d}\nu. \tag{2.8}$$

The photoionization rate is thus given by

$$\Gamma_{P,\,i} = \sigma_{I,\,i} \dot{N}. \tag{2.9}$$

In addition to photoionization, we include collisional ionization due to the interaction of free electrons and neutral atoms. As this is a kinetic process, the collisional ionization rate, Γ_C, depends on the thermal state of the electrons and is given by

$$\Gamma_C = n_e \sum_i \Gamma_i(T) n_i, \tag{2.10}$$

where $\Gamma_i(T)$ are the collisional ionization rates and n_e is the electron number density. The total ionization rate is the sum of photo- and collisional ionization rates, $\Gamma = \Gamma_P + \Gamma_C$.

The inverse process of ionization is recombination. This free–bound interaction of electrons and ions depends on temperature and number density of ions and electrons. The number of recombinations per unit time per hydrogen atom $[\,\mathrm{s}^{-1}\,]$ is

$$R_i = n_e \alpha_i(T), \tag{2.11}$$

where $\alpha_i(T)$ is the recombination coefficient of species i.

We note that we use the 'case B' recombination coefficient where the recombination transition to the ground-state is excluded under the assumption that the radiation associated with this transition is absorbed nearby, resulting in a new ionization. This is referred to as the 'on-the-spot' approximation. Details on the implementation of these processes, as well as the various rates and cross-sections used can be found in chapter 5 of Kruip (2011).

Together, ionizations and recombinations determine the ionization-state of the gas, described by the following three coupled differential equations and three closure relations

$$\begin{aligned}
\dot{n}_{H^{0+}} &= n_{H^+}R_{H^+} - n_{H^{0+}}\Gamma_{H^{0+}} \\
\dot{n}_{He^{0+}} &= n_{He^+}R_{He^+} - n_{He^{0+}}\Gamma_{He^{0+}} \\
\dot{n}_{He^+} &= n_{He^{2+}}R_{He^{2+}} - n_{He^+}\Gamma_{He^+} \\
n_H &= n_{H^{0+}} + n_{H^+} \\
n_{He} &= n_{He^{0+}} + n_{He^+} + n_{He^{2+}} \\
n_e &= n_{H^+} + n_{He^+} + 2n_{He^{2+}}.
\end{aligned} \tag{2.12}$$

This set of equation does not have a general analytical solution and must be solved numerically. For this purpose, we adopt the sub-cycling scheme described in Pawlik & Schaye (2008). In this scheme, ionizations and recombinations are evolved on a time-scale that is smaller than the ionization or recombination time-scales t_{ion} and t_{rec}. During a RT time-step, the ionizing flux is assumed to be constant, making the procedure manifestly photon-conserving. This allows for radiative time-steps Δt_{rt} that are much larger than the dominant time-scale governing the evolution of the ionization state. The sub-cycling time-step for both ionization and recombination is

$$\Delta t_{sub} \equiv \frac{t_{ion}t_{rec}}{t_{ion} + t_{rec}}. \tag{2.13}$$

Because the procedure is analogous for each species, we give here only the explicit example for the integration step for hydrogen. At time $t_{sub} \in (t_{rt}, t_{rt} + \Delta t_{rt})$ the rate equation is given by

$$dn_{H^+}^{(t_{sub})} = n_{H^{0+}}^{(t_{sub})}\Gamma_H^{(t_{sub})}\Delta t_{sub} - n_e^{(t_{sub})}n_{H^+}^{(t_{sub})}\alpha_H(T)\Delta t_{sub}, \tag{2.14}$$

where the photoionization rate at t_{sub} is

$$\Gamma_H^{(t_{sub})} = \Gamma_H \left(\frac{1 - e^{-\tau^{(t_{sub})}}}{1 - e^{-\tau}} \right) \frac{n_{H^{0+}}}{n_{H^{0+}}^{(t_{sub})}}, \tag{2.15}$$

where Γ_H and τ are the photoionization rate and optical depth at the beginning of the sub-cycling and $\tau^{(t_{sub})} = \tau n_{H^{0+}}^{(t_{sub})}/n_{H^{0+}}$. By defining the photoionization rate in this way, the ionizing flux in the cell is constant during the RT time-step. This sub-cycling scheme becomes computationally expensive when $\Delta t_{sub} \ll \Delta t_{rt}$, but photoionization equilibrium is generally reached after a few sub-cycles. It is then no longer necessary to explicitly integrate the rate equation, but instead use the values of the preceding sub-cycle step. This way of sub-cycling ensures photon conservation even for large RT time-steps.

2.2.3   Application of SimpleX to η Car

Since the SimpleX calculations are performed as post-processing on the 3D SPH simulation output, we use snapshots corresponding to an orbital phase of apastron (Figure 2.1). The reason for this choice lies in the slow dynamical changes that the system undergoes around apastron. This 'stable' situation allows us to run RT simulations for a sufficiently long time without worrying about important changes to the 3D structure of the system that occur around periastron (Okazaki et al. 2008, Parkin et al. 2011; M12, M13). Moreover, the *HST*/STIS mapping data currently in-hand to be modelled was taken at phases around apastron during η Car's orbital cycle (Gull et al. 2011; Teodoro et al. 2013). Detailed modelling of future (late 2014 through early 2015) *HST* observations obtained across η Car's periastron event is deferred to future work.

We focus on the ionization of H and He due to η_B, assuming the same abundance by number of He relative to H as Hillier et al. (2001), $n_\mathrm{He}/n_\mathrm{H} = 0.2$. The reasons for this single-source approximation are discussed in Section 2.2.3.1. We performed tests to determine the correct time-step for accurate RT calculations of the ionization volumes and fractions, and find that a simulation time-step of ~ 3 s is required. The SPH output is post-processed with SimpleX until the ionization state reaches an equilibrium value. This typically happens within ~ 3 months for the SPH snapshots investigated. We thus set the total SimpleX simulation time to three months. Because the gas is assumed to be initially almost fully neutral, this provides an upper limit on the time it takes before convergence is reached. Since this limit is well within the orbital time-scale around apastron, this is another indication that post-processing of the SPH simulations does not significantly alter our results.

2.2.3.1   Influence of the Primary Star η_A

Detailed fitting of the optical and UV spectra of η Car by Hillier et al. (2001, 2006) and Groh et al. (2012a) shows that for $\dot{M}_{\eta_\mathrm{A}} \approx 8.5 \times 10^{-4}$ M$_\odot$ yr^{-1}, the region of fully ionized H around η_A extends radially ~ 120 au, while the region of doubly-ionized He extends ~ 0.7 au, and that of singly-ionized He from ~ 0.7 to 3 au. Assuming a constant spherical mass-loss rate, the density in the η_A wind is expected to fall off as r^{-2}. To explore the dependence of the position of the ionization fronts on the ionizing luminosity of η_A, we performed 1D calculations using an equilibrium chemistry solution where the ionization fractions of hydrogen and helium are set to their equilibrium values under the assumption that the incoming flux of ionizing photons is constant. As mentioned in Section 2.2.2.2, the ionization state of the gas is described by the first three equations in set (2.12). We can derive the equilibrium equations by setting $\dot{n}_{\mathrm{H}^{0+}} = \dot{n}_{\mathrm{He}^{0+}} = \dot{n}_{\mathrm{He}^+} = 0$. After some algebra this yields

$$
\begin{aligned}
x_{H^{0+}} &= \left(1 + \Gamma_{H^{0+}}/R_{H^+}\right)^{-1} \\
x_{H^+} &= 1 - x_{H^{0+}} \\
x_{He^{0+}} &= \left[1 + \Gamma_{He^{0+}}/R_{He^+} \times \left(1 + \Gamma_{He^+}/R_{He^{2+}}\right)\right]^{-1} \\
x_{He^+} &= x_{He^{0+}} \Gamma_{He^{0+}}/R_{He^+} \\
x_{He^{2+}} &= x_{He^+} \Gamma_{He^+}/R_{He^{2+}},
\end{aligned}
\tag{2.16}
$$

where x_i is the fraction of species i and we have used $n_i = x_i n_j$ where $j \in (H, He)$. These equations are coupled by the free electron density given by the last equation in (2.12).

Unfortunately, the set of equations (2.16) cannot be solved analytically due to the non-linear dependence on ionization fractions of the photoionization rate through the optical depth. More specifically, the photoionization rate in a cell is given by Equation (2.6), where the monochromatic analog of Equation (2.4) is

$$
\dot{N}_{ion} = \dot{N}_\gamma [1 - \exp(-\tau)],
\tag{2.17}
$$

with $\tau = (x_{H^{0+}} n_H \sigma_{H^{0+}} + x_{He^{0+}} n_{He} \sigma_{He^{0+}} + x_{He^+} n_{He} \sigma_{He^+})l$. Because of this non-linear dependence, the equilibrium fractions must be solved iteratively. If the iterative procedure converges, the neutral fractions are assigned to the cell under treatment and the flux is diminished by the number of absorptions during that time-step Δt ($n_{H^{0+}} \Gamma_{H^{0+}} \Delta t$).

The density profile used in the 1D code is obtained from $\rho(r) = \dot{M}_{\eta_A}/4\pi r^2 v(r)$, where $v(r) = v_\infty (1 - R_\star/r)^\beta$ (see M13, equation A1). The 1D code simulates radiation travelling through spherically symmetric shells with a maximal radius of the simulation, ≈ 1622 au. The radiation is injected in the first shell and then travels outwards until it is either absorbed or exits the last shell. For the results shown we used $\sim 3 \times 10^4$ shells. We note that time-stepping is arbitrary because of the equilibrium chemistry. The only variable is therefore the luminosity of the source η_A.

Using $\dot{M}_{\eta_A} \approx 8.5 \times 10^{-4}$ M$_\odot$ yr^{-1}, for luminosities below a critical value (1.9×10^{53} s^{-1}), the computational box is neutral and the Strömgren radii are confined to the central 0.7 au (top panel, Figure 2.2). The H ionization front is located somewhere between the centre and the outside of the box for a very small range of luminosity values (centred around 1.91756×10^{53} s^{-1}, centre panel, Figure 2.2). The slightest increase in luminosity results in a completely ionized box, while further increase results only in a lower neutral fraction throughout the simulation volume (bottom panel, Figure 2.2). This behaviour is completely expected, however, for ionization fronts in power-law density profiles with powers less than $-2/3$ (Franco, Tenorio-Tagle & Bodenheimer 1990; Shapiro et al. 2006). For such profiles, the circumstellar medium simply cannot support stable ionization fronts.

For these reasons, constraining the ionization fronts in η_A's wind to the values derived by Hillier et al. (2001, 2006) and Groh et al. (2012a) using SIMPLEX is practically
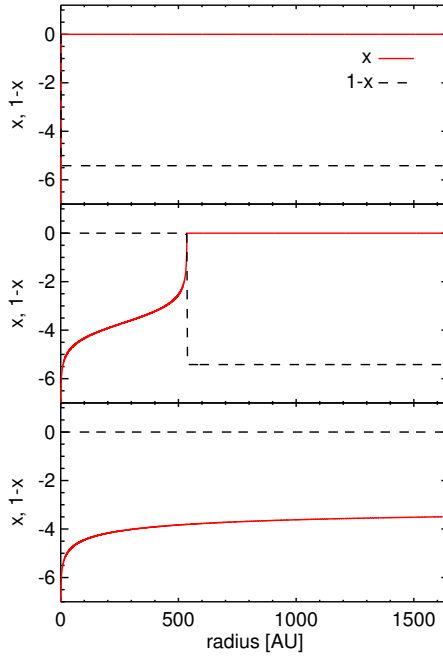
Figure 2.2 – Neutral (x, solid lines) and ionized ($1-$ x, dashed lines) fractions of H (log scale) as a function of distance for the 1D RT simulations of η_A described in Section 2.2.3.1 and luminosities of Top: 1.9×10^{53} s^{-1}, Centre: 1.91756×10^{53} s^{-1}, and Bottom: 1.91758×10^{53} s^{-1}. This behaviour signifies that the H ionization front is highly unstable and thus changes qualitatively with small perturbations in either the density or the luminosity.

impossible given the fronts' intrinsically unstable nature. We realize this 1D result is over-simplified since the instability is real in a pure H or H + He gas, but will disappear with the introduction of the myriad of spectral lines, mostly by Fe, that have a so-called 'line blanketing' effect on the stellar spectra. However, the inclusion of such additional species and blanketing effects is beyond the scope of this paper.

Given the above difficulties, the most sensible choice for an initial effort to model the ionized WWIRs is to omit η_A's radiation altogether. This may seem an oversimplification at first, but there are several arguments for this approximation. First, for the high $\dot{M}_{\eta_A}$ Case A and B simulations, 1D CMFGEN models by Hillier et al. (2001, 2006) show that the primary source will sustain an ionized hydrogen region that spans roughly 240–260 au in diameter, ~ 0.04–0.05% of the volume of the SPH and SimpleX simulations. The same models show that the total sum volume of singly plus doubly ionized helium in the central η_A wind accounts for $\sim 10^{-6}\%$ and $10^{-5}\%$ of the SimpleX simulation volume for Cases A and B, respectively. These volumes are too close to the primary and too small to directly affect the ionization fronts and fractions at the locations where the spatially-extended, high-velocity forbidden line emission forms, especially at orbital phases near

apastron (Gull et al. 2009, 2011; M12; M13). They may, however, influence the ionization structure further away indirectly by reducing the opacity for photons from the secondary source. This may be especially true very close to periastron. We expect that this would primarily result in UV flux from η_A penetrating the WWIR more easily, effectively increasing the ionized fraction on the far side of the primary source. For an observer on Earth though, this region is, at periastron, located behind η_A and therefore likely obscured by the dense primary wind.

Secondly, although extremely luminous, because it is enshrouded by a dense, optically-thick wind, η_A has a spectrum representative of a much cooler star than η_B (Hillier et al. 2001, 2006). The effective temperature of η_A at optical depth $\tau = 2/3$ ($r \approx 4$ au) is predicted to be ~ 9200 K for Cases A and B (Hillier et al. 2001, 2006). The ionizing flux from η_A is thus substantially diminished before reaching the WWIR, located ~ 20–22 au from η_A when the system is near apastron. Since essentially zero photons with energies above 13.6 eV from η_A reach the WWIRs on the apastron side of the system at times near apastron, omission of the η_A source is a justifiable simplification when the focus is on forbidden emission lines with ionization potentials above 13.6 eV.

One might try to argue that because the ionized hydrogen and helium volumes in the inner primary wind extend far enough to encompass both stars and the WWIR at phases close to periastron, photons from η_A will also reach the apastron side of the simulation volume. This argument relies, however, on the assumption that the ionized regions are indeed spherical and therefore penetrate the WWIR towards the secondary star. This assumption is likely incorrect given the high density of the WWIR. In other words, we would be applying a model based on spherical symmetry to a region that clearly has a very asymmetrical geometry.

The exception to the above arguments is the Case C simulation. In this instance, according to 1D CMFGEN models (Hillier et al. 2006; M13), H is fully ionized in the pre-shock η_A wind throughout the entire simulation domain. Moreover, the He$^+$ region in the inner η_A wind extends radially ~ 120 au. While neglecting the η_A ionizing source in this case likely produces incorrect RT results in the regions of η_A wind on the periastron side of the system, for our purposes, the situation is actually not so bad. First, we note that, based on previous works, the mass-loss rate of η_A is very likely not as low as the value assumed in the Case C situation (see arguments in e.g. Hillier et al. 2006; Parkin et al. 2009; Teodoro et al. 2012, 2013; Russell 2013; M12; M13), and so we will not be using the SimpleX results obtained here for Case C to model the observed broad, high-ionization forbidden line emission. Rather, in addition to investigating how a reduced $\dot{M}_{\eta_A}$ affects the ionization structure on the apastron side of the system, we use Case C as an illustrative example to determine whether η_B's ionizing radiation can penetrate the dense WWIRs and further affect the ionization state of η_A's wind. Having H initially ionized in the pre-shock η_A wind would primarily influence the ionization structure indirectly by reducing the opacity for photons from η_B (assuming they can penetrate the WWIR), increasing the ionized fraction of H in the pre-shock η_A wind, but having little effect on the overall ionization volume.

Regarding the He ionization structure in Case C, because the inner He^+ region extends ~ 120 au, the innermost WWIR penetrates η_A's He^+ zone, even at apastron. However, the total volume of this inner He^+ region is still only $\sim 0.04\%$ of the total SimpleX simulation volume, again too small to directly affect the ionization fronts and fractions at the locations where the high-ionization forbidden lines of interest form. Assuming He is neutral in the η_A wind at the start of the SimpleX simulations also allows us to more easily determine whether He-ionizing photons from η_B can penetrate the WWIRs and affect the pre-shock η_A wind. If so, the primary effect will be an increased fraction of He^+ in the innermost η_A wind, with little to no effect on the shape or extent of the He^+ ionization volume. Moreover, since η_B is thought to be an O- or WR-type star with $T_{eff} \simeq 36{,}000$–$41{,}000$ K (Verner, Bruhweiler & Gull 2005; Hillier et al. 2006; Teodoro et al. 2008; Mehner et al. 2010), the number of photons it produces capable of ionizing He^+ to He^{2+} is effectively zero. Thus, there will be no He^{2+} region created by η_B beyond the WWIR zone, even if η_B's radiation can penetrate the dense post-shock gas. Therefore, even for simulation Case C, the neglecting of η_A's radiation is a justifiable simplification for the purposes of our work. The only caveat is that we do not account for any possible ionization of η_A's pre-shock wind to He^{2+} by soft X-rays produced in the $420\ km\,s^{-1}$ η_A shock. However, any such He^{2+} region near the WWIR zone at times around apastron is very likely to be negligible in extent, if it exists at all, as evidenced by the absence of any significant detectable He II $\lambda 4686$ emission in η Car during its spectroscopic high state (Mehner et al. 2011; Teodoro et al. 2012).

Based on the above considerations, we neglect the η_A ionizing source in this work and focus on the influence of η_B.

2.2.3.2 The Ionizing Source η_B

For the RT calculations, we place a spherical ionizing source centred at the location of η_B. This 'source' is composed of a series of individual points randomly distributed about the sphere that defines the injection radius used in the SPH simulations for the wind of η_B ($30\ R_\odot$). We use a total of 50 source points, which is large enough to result in a nearly isotropic photoionizing source. We find that using more points has little effect on the RT results. The total luminosity is divided among all 50 points, forming the nodes of the grid that emit radiation. These nodes are also capable of absorbing any radiation emitted by neighbouring points in the SimpleX grid. Based on the work of Mehner et al. (2010), Verner, Bruhweiler & Gull (2005) and M12, we assume for η_B a total ionizing flux for hydrogen and helium of 3.58×10^{49} photons s^{-1} (3.02×10^{49} capable of ionizing H^{0+} and 5.62×10^{48} for ionizing He^{0+}), consistent with an O5 giant with $T_{eff} \approx 40{,}000$ K (Martins, Schaerer & Hillier 2005).

2.3   Results

To provide context for interpreting the RT results below, we begin with a brief description of the density and temperature structure of the system in the orbital plane for the Case A simulation (Figure 2.3). Example number density slices in the *xz* and *yz* planes, plus number density slices in each plane for the Case B and C simulations, can be found in Figures 2.5, 2.7, and 2.9. Example slices showing temperature for each case can be found in M13. We focus on the Case A simulation as the $\dot{M}_{\eta_A}$ assumed in this case most likely represents η_A's current observed mass-loss rate (Groh et al. 2012a; M13).
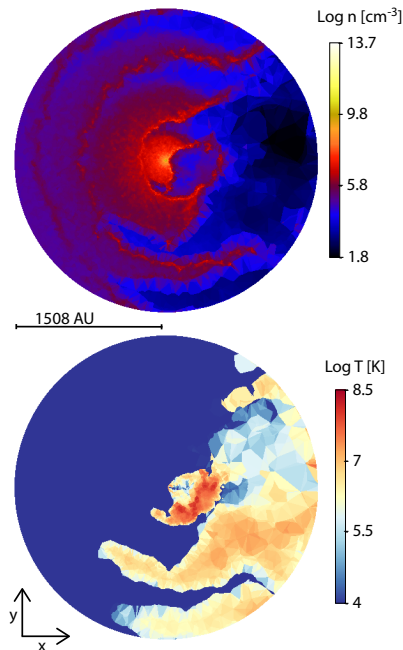
Figure 2.3 – Slices in the *xy* orbital plane through the 3D simulation volume for the Case A simulation at apastron. The top plot shows the number density (log scale, cgs units), while the bottom shows log temperature (K). The lower density η_B wind is shock-heated by the wind–wind interaction to temperatures up to $\sim 10^{8.5}$ K. On the periastron (left-hand) side the denser η_A wind and compressed shells formed at periastron radiatively cool to $T \sim 10^4$ K.

Pittard et al. (1998), Pittard & Corcoran (2002), Okazaki et al. (2008), Parkin et al. (2009, 2011), Madura et al. (2012), and Russell (2013) showed that η_B is between the observer and η_A at apastron. Due to the highly eccentric binary orbit, η_B spends most of its time near apastron (right-hand side of panels in Figure 2.3), so that the relatively undisturbed wind of η_A is located on the far (periastron) side of the system. Across every periastron passage, the hot and low density wind of η_B pushes outward into the slow, high-density η_A wind, leading to the formation of a thin, high-density wall surrounding the

lower density, trapped wind of η_B (Parkin et al. 2011; M13). This dense wall is accelerated to a velocity higher than the normal terminal velocity of η_A's wind and expands creating a thin, high-density sheet of trapped primary wind material. During periastron passage the arms of the WWIR become extremely distorted by orbital motion as the binary stars move towards their apastron positions. Moving back towards apastron, orbital speeds decrease and the η_B wind cavity regains its axisymmetric conical shape (Okazaki et al. 2008, Parkin et al. 2011; M13).

Dense arcs and shells of η_A wind visible in the outer regions on the apastron side of the system in the top panel of Figure 2.3 highlight the fact that the binary has already undergone multiple orbits. Narrow cavities carved by η_B in η_A's dense wind during each periastron passage also exist on the periastron side of the system. Bordering these narrow cavities are the compressed, density-enhanced shells of primary wind formed as a result of the rapid wind–wind collision during each periastron.

While the periastron side of the system is dominated by the dense wind of η_A, the apastron side is dominated by the much lower-density, faster wind of η_B, although arcs of compressed η_A wind also extend to the apastron side. These arcs are the remnants of the shells of η_A wind that flow in the apastron direction when η_B is at periastron (M13). The partially intact, most recent shell is visible just to the right of the centre of the image in the top panel.

There is also a clear temperature asymmetry between the apastron and periastron sides of the system (bottom panel of Figure 2.3). The gas on the periastron side is much colder at $T \approx 10^4$ K. The various wind–wind collisions on the apastron side produce large volumes of gas shock-heated to temperatures between 10^6 and $10^{8.5}$ K. Because the gas on the apastron side is composed mostly of η_B wind material of low density, it cools slowly and adiabatically, allowing it to remain hot throughout the 5.54 yr orbital cycle. In contrast, the dense shells of post-shock primary wind cool radiatively very quickly down to $T \sim 10^4$ K (Parkin et al. 2011; M13). The innermost region of the system where the current WWIR is located, and the region where η_B's wind collides with the latest ejected shell of primary wind, have the highest temperatures and are responsible for the observed time-variable X-ray emission (Hamaguchi et al. 2007; Okazaki et al. 2008; Corcoran et al. 2010; Parkin et al. 2011).

2.3.1   The Importance of Collisional Ionisation

The bottom panel of Figure 2.3 shows that the shocks induced by the violent wind–wind collisions heat the gas in the system to very high temperatures. Since the lower-density material from η_B cools adiabatically, this gas remains extremely hot for most of the orbit, at temperatures well above those where collisional ionizations become important ($\gtrsim 10^6$ K). The collisional ionization fraction depends strongly on the temperature of the gas, which is in principle a function of the hydrodynamical motion, photoheating, and multiple cooling terms. In this initial study, as a first approximation we use the temperature calculated by the SPH code to estimate the importance of collisional ionizations. In or-

der to assess which process dominates, we performed a series of simulations with/without collisional-/photoionization. For brevity, we discuss here only the results for hydrogen for simulation Case A. Results for helium and Cases B and C are qualitatively similar.

Figure 2.4 summarizes the results. The three panels represent the SIMPLEX output if we include, respectively, only collisional ionization, only photoionization, or both. For the only collisional ionization case, we assume collisional ionization equilibrium as an initial condition to the RT, as described in Section 2.2.2.2. In this case, the overall ionization structure unsurprisingly follows the plot of the temperature in Figure 2.3. The cold, dense primary wind on the periastron side of the system, and the dense WWIRs of compressed primary wind that extend to the apastron side of the system (both in black in the first panel of Figure 2.4), remain mostly neutral. However, hydrogen in the hot, lower density regions of shocked secondary wind are collisionally ionized (in blue and purple in the first panel of Figure 2.4). The η_B wind in the outermost parts of the system is the most highly ionized due to the much lower density of the gas there, which results in less recombination. We also note in particular the two 'fingers' of highly ionized η_B gas that extend into the primary wind, located at the bottom of the panel. More importantly, we see that when only collisional ionizations are used, the dense WWIRs remain almost entirely neutral.
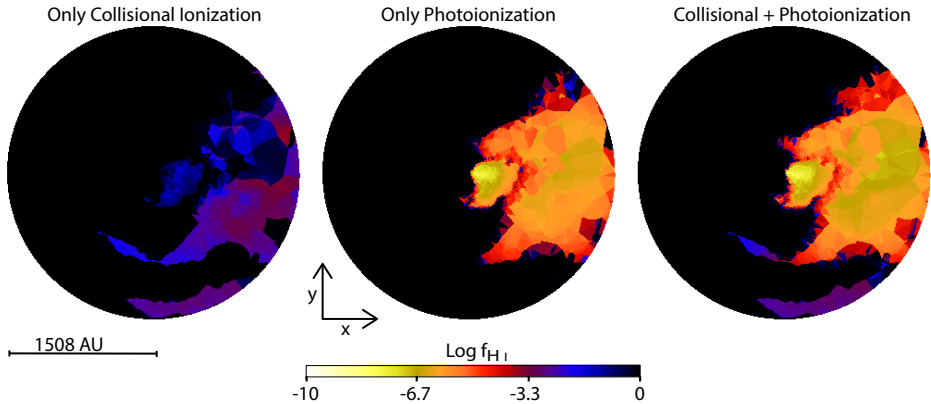

Figure 2.4 – Slices in the *xy* orbital plane through the 3D SIMPLEX simulation volume for Case A at apastron showing the logarithm of the fraction of neutral hydrogen assuming Left: collisional ionization only, Centre: photoionization only, and Right: collisional- and photo-ionization. Including collisional ionization is necessary to ionize the small cavities in the primary wind and the 'fingers' of low-density η_B wind trapped between the higher density walls of η_A wind that form around periastron.

In the case of only photoionizations from η_B (middle panel of Figure 2.4), mainly the lower-density η_B wind on the apastron side of the system is highly ionized (in yellow and orange). The lower-density hot fingers of η_B wind trapped between the high-density walls of η_A wind show no ionization. These regions are effectively shielded from the ionizing flux of η_B. Another important difference is the level of ionization in the η_B wind. Photoionizations are capable of reducing the fraction of neutral hydrogen by roughly four

more orders of magnitude, compared to the case with only collisional ionization. Additionally, the η_B wind closest to the centre of the simulation is the most highly ionized since, even though the density is higher there, the material is much closer to the luminous ionizing source. This is the exact opposite of what was observed in the case of only collisional ionizations. We also see that photons from η_B are capable of penetrating the innermost wall of η_A wind material on the apastron side of the system, thus also highly ionizing it and the outer portions of η_B's wind. Detailed examination further shows that when photoionizations are used, the edges of the WWIRs facing η_B can be significantly ionized ($\log f_{H^{0+}} \lesssim -3$; see Chapter 3).

Using both collisional- and photoionizations results in a situation that resembles a superposition of the first two panels (right-hand panel of Figure 2.4). The η_B wind on the apastron side remains highly ionized, but collisional ionization helps ionize the fingers of η_B wind located at the bottom of the panel. Interestingly, the H^{0+} in the fingers is slightly more ionized now compared to the case with only collisional ionizations. This is because, due to the now reduced opacity caused by including collisional ionization, photons from η_B can more easily penetrate into the fingers and increase the overall level of ionization. A similar effect is seen in/near the WWIRs, which are also slightly more ionized when both collisional- and photo-ionizations are included, compared to the case with only photoionization. However, even when both collisional- and photoionizations are used, the dense η_A wind on the periastron side of the system remains neutral.

Given all of these results, we consider both collisional- and photoionizations as necessary for any proper RT simulations of η Car. The remainder of the results in this paper are based on simulations that accordingly incorporate both.

2.3.2   Overall ionization structure and influence of $\dot{M}_{\eta_A}$

2.3.2.1   The orbital plane

The top row of Figure 2.5 shows the SIMPLEX number density in the orbital plane for simulation Cases A–C. As demonstrated by M13, $\dot{M}_{\eta_A}$ determines the overall shape of the WWIRs and the stability of the arcuate shells expanding on the apastron side of the system. Lowering $\dot{M}_{\eta_A}$ increases the opening angle of the shock cone created by η_B, increasing the volume of low-density η_B wind. This is particularly noticeable in the size of the low-density fingers of η_B wind that strongly reduce the volume of unperturbed primary wind. The lower the $\dot{M}_{\eta_A}$, the wider and more extended the fingers. In Cases B and C, the fingers extend to the back (periastron) side of η_A's wind. The dense shells of η_A wind on the apastron side are also more stable and remain intact longer for higher values of $\dot{M}_{\eta_A}$ (M13). As a consequence, we expect that the 3D shape, position, intensity, and variability of the ionization depend strongly on $\dot{M}_{\eta_A}$.

The middle and bottom rows of Figure 2.5 present, respectively, the computed fractions of H^{0+} and H^+ in the orbital plane. The WWIRs and high-density walls surrounding the lower-density trapped wind of η_B define the separation between the neutral and
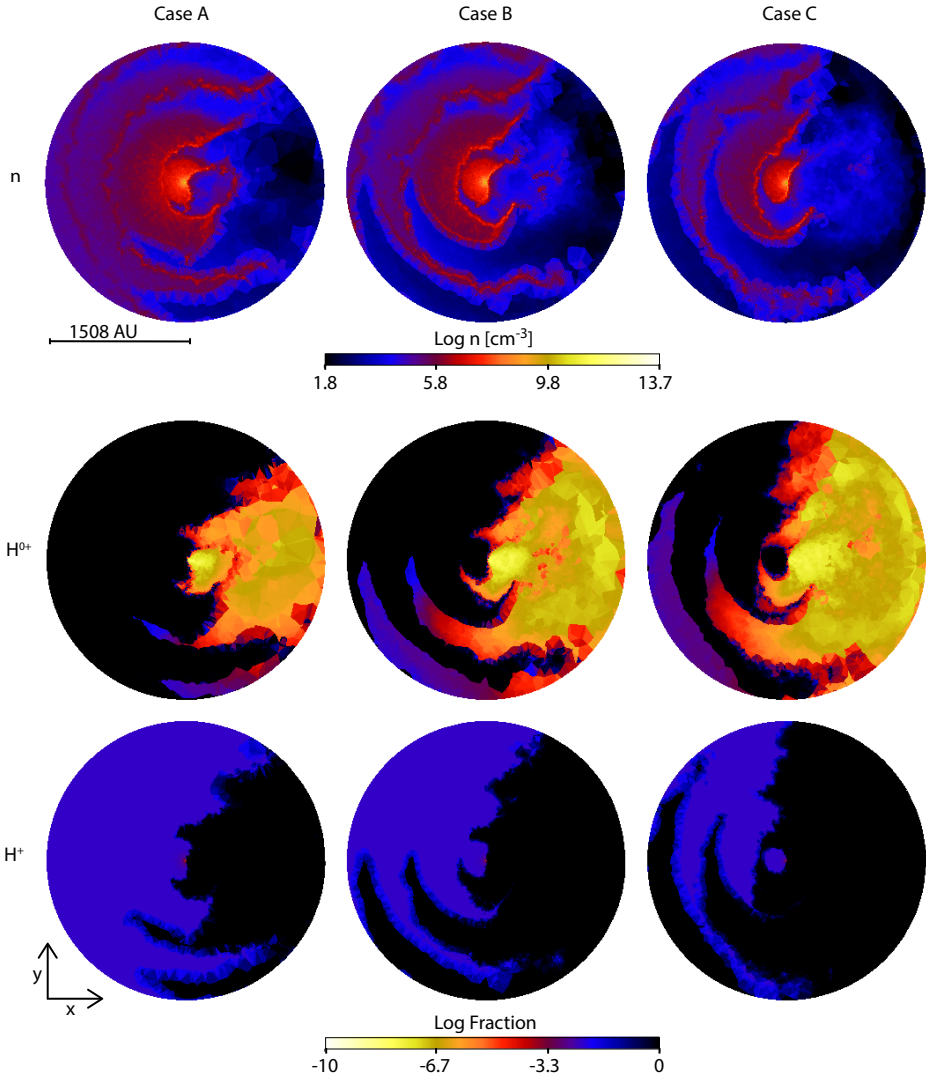
Figure 2.5 – Slices in the *xy* orbital plane through the 3D SimpleX simulation volume for the three different assumed $\dot{M}_{\eta_A}$. Columns illustrate, from left to right, Cases A to C. Rows show, from top to bottom, the SimpleX number density (log scale, cgs units) and the computed fractions of H^{0+} and H^+ (log scale).

ionized-hydrogen regions. These high-density η_A wind structures are able to trap the hydrogen ionizing photons from η_B. We also see that as $\dot{M}_{\eta_A}$ decreases, the volume of ionized hydrogen increases greatly on both the apastron and periastron sides of the system. The larger fingers for Cases B and C allow the ionizing radiation from η_B to penetrate into the low-density cavities that are carved within the back side of the primary wind every periastron passage.

In the H^+ maps of Figure 2.5 it is possible to see a large fraction of neutral hydrogen at and to the periastron side of η_A. As described in Section 2.2.3.1, in reality, the hydrogen in this inner region should be ionized by η_A out to a radius of $\sim$ 120 au in Cases A and B, and everywhere in Case C. However, the absence of an η_A ionizing source in our simulations prevents this from occurring. Nonetheless, the absence of an η_A source in our simulations reveals an important result that may otherwise be missed, namely, that the high optical depth of the inner WWIR prevents any η_B ionizing photons from penetrating into the inner η_A wind. The lack of any regions of ionized hydrogen in the unshocked primary wind on the periastron side of the system implies that regardless of the ionization structure of η_A's innermost wind, ionizing photons from η_B cannot penetrate the inner WWIR or significantly affect the dense η_A wind on the periastron side of the system at times around apastron.

Figure 2.6 illustrates the fractions of He^{0+}, He^+ and He^{2+} in the orbital plane for the three $\dot{M}_{\eta_A}$ simulations. Comparing to Figure 2.5, we see that the regions of He^{2+} correlate strongly with the regions of H^+. As expected, the regions of H^{0+} and He^{0+} are also correlated. The fully-ionized nature of helium in the lower density η_B wind is due to the presence of large volumes of very high temperature shocked gas, plus the relatively close proximity of such gas to the hot, luminous η_B ionizing source. As with hydrogen, the helium in the denser primary wind is neutral. The trends as a function of $\dot{M}_{\eta_A}$ seen in Figure 2.5 for the hydrogen ionization structure are also apparent in the plots of He^{0+} and He^{2+}. This is a key result, as it implies that even with the lower $\dot{M}_{\eta_A}$ of Case C, η_B's He-ionizing radiation cannot penetrate significantly the dense WWIRs.

The structure of He^+ (middle row of Figure 2.6) is more involved than that of He^{0+} and He^{2+}. Interestingly, significant fractions of He^+ are principally located in the high-density walls of the WWIRs and outer edges of the dense fingers of η_A wind that define the low-density fingers of η_B wind. Regions of lower temperature unshocked η_B wind also consist of mostly He^+. The He^+ is seen primarily as a marker for the transition between the regions of He^{0+} and He^{2+}. For this reason He^+ appears to be an excellent tracer for the high-density compressed post-shock η_A gas.

2.3.2.2 The *xz* and *yz* planes

To help the reader more fully appreciate the complex 3D structure of the simulation results, Figures 2.7–2.10 present slices showing the number density and H and He ionization structures in the *xz* and *yz* planes for each $\dot{M}_{\eta_A}$. The differences in ionization structure between the three $\dot{M}_{\eta_A}$ are even more apparent in these two planes. There is a clear left–right asymmetry in the density and ionization structure in each panel of the figures. As in Figures 2.5 and 2.6, the regions of He^{2+} correlate strongly with the regions of H^+, while regions of He^{0+} correlate with those of H^{0+}. The overall volume of ionized material increases with decreasing $\dot{M}_{\eta_A}$.

Figure 2.7 shows that the higher the value of $\dot{M}_{\eta_A}$, the smaller the wind cavities carved by η_B on the left-hand (periastron) side of the system. They are practically invisible for
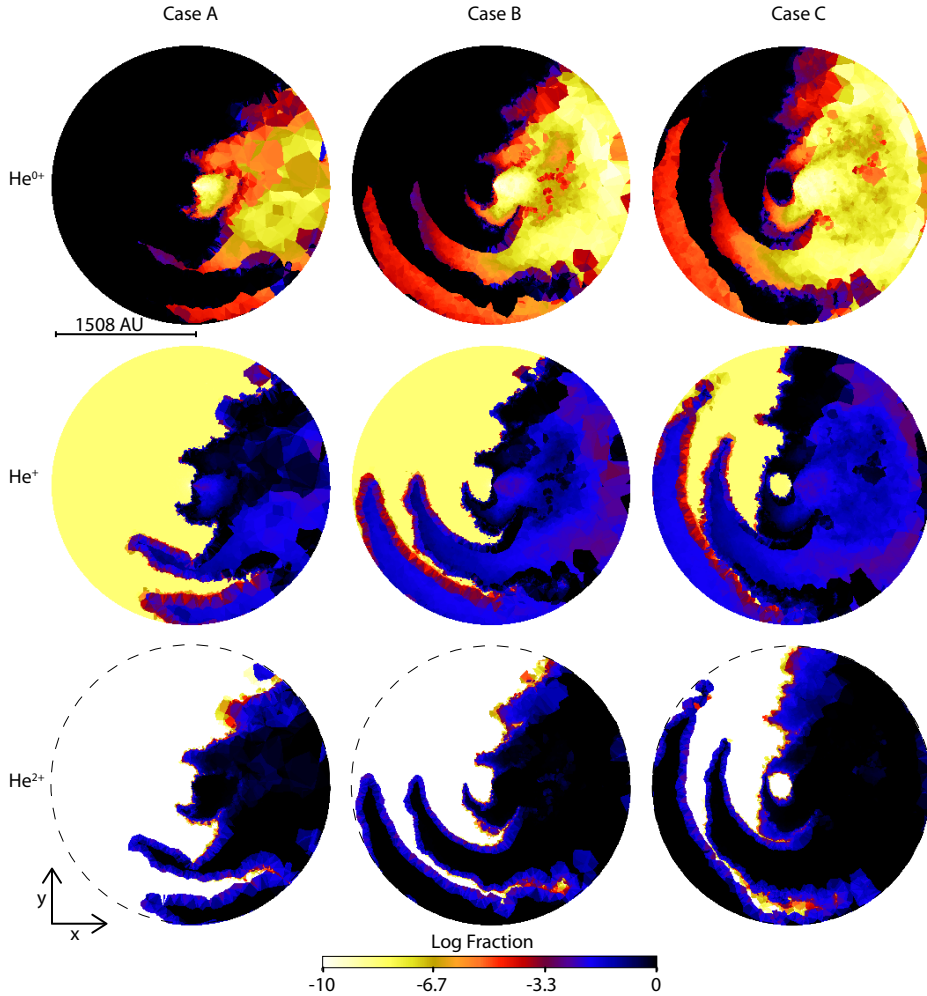
Figure 2.6 – Same as Figure 2.5, but with rows showing, from top to bottom, the computed fractions of He^{0+}, He^+ and He^{2+} (log scale). In this and future plots of He^{2+}, the dashed circle marks the edge of the spherical computational domain.

Case A. As a result, hydrogen and helium both appear neutral on the left in the Case A panels. Only the large η_B wind cavity on the apastron side of the system is ionized in Case A. Figures 2.7 and 2.8 illustrate how the wind cavities on both the periastron and apastron sides of the system are much larger and remain hot for Cases B and C, resulting in well defined regions of ionized hydrogen and helium.

The top row of Figure 2.7 also shows clear differences with $\dot{M}_{\eta_A}$ in the density and fragmentation of the dense shell of η_A wind material on the right-hand (apastron) side of the system. In Case A, the dense shell is more or less intact, while in Cases B and C
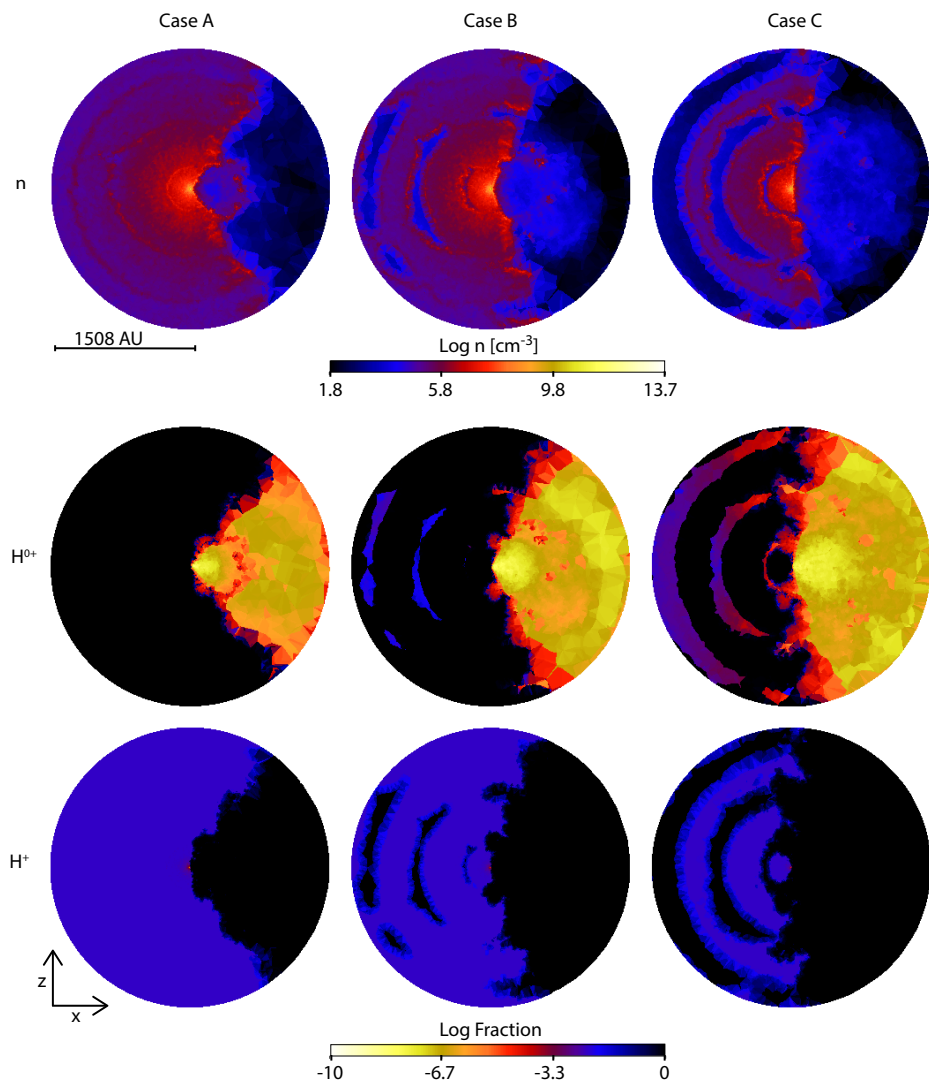
Figure 2.7 – Same as Figure 2.5, but for slices centred in the *xz* plane.

it has fragmented considerably and started to mix with the lower density η_B wind. This fragmenting shell produces an interesting hydrogen ionization structure on the right-hand (apastron) side of the system that consists of an inner and outer region of low-density, highly ionized η_B wind (in yellow/orange, middle row of Figure 2.7) separated by a diffuse shell of denser, less-ionized η_A wind (in red). The middle row of Figure 2.8 again shows that the He$^+$ is located in the high-density walls of the WWIRs and outer edges of the dense fingers of η_A wind that define the low-density fingers of η_B wind, thus tracing the
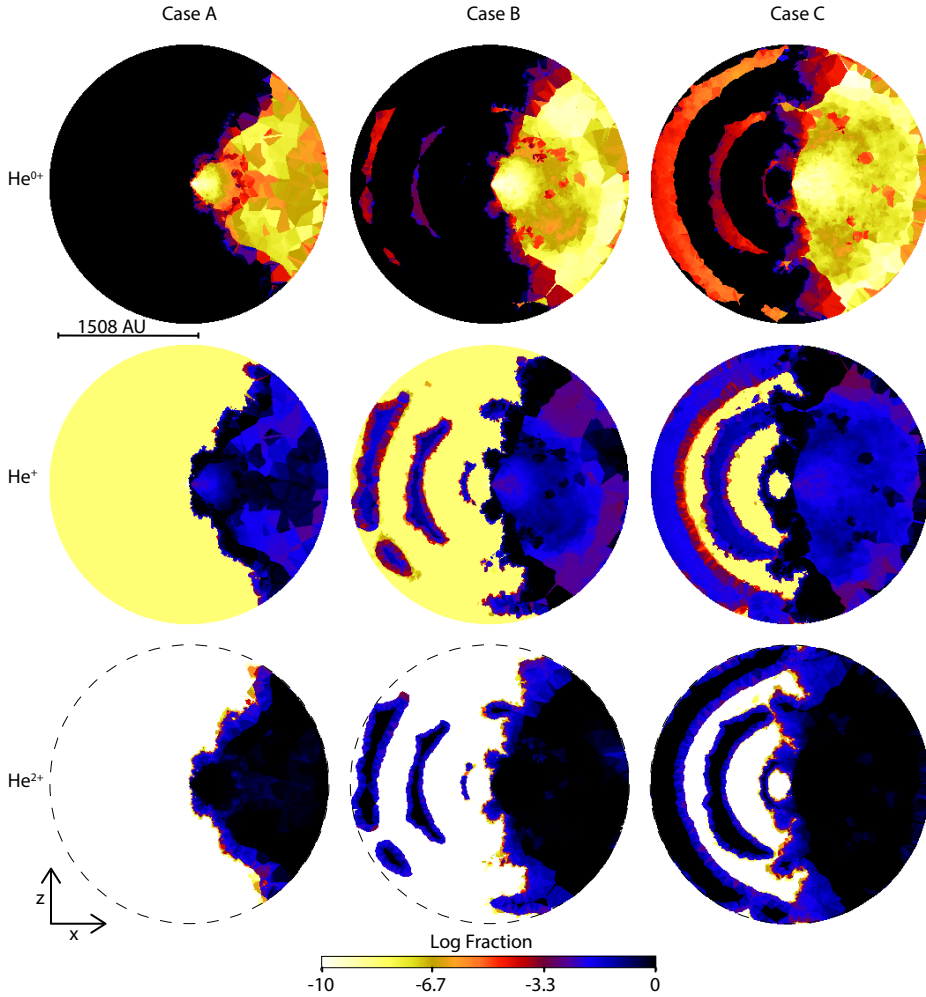
Figure 2.8 – Same as Figure 2.6, but for slices centred in the *xz* plane.

compressed post-shock η_A gas.

Figure 2.9 shows that the cavities carved on the right-hand ($+y$) side are always smaller than the ones carved on the left-hand ($-y$), regardless of the value of $\dot{M}_{\eta_\text{A}}$. However, the difference in cavity size between the $+y$ and $-y$ sides increases with decreasing $\dot{M}_{\eta_\text{A}}$. The larger cavities on the left-hand ($-y$) side are also hotter, resulting in well-defined regions of ionized H and He concentrated on the left-hand side. Finally, we see that the shells of dense, compressed η_A wind on the left are thicker and remain intact longer the higher the $\dot{M}_{\eta_\text{A}}$, reducing the overall volume of ionized material. We note that in reality, H should be ionized everywhere in Case C.
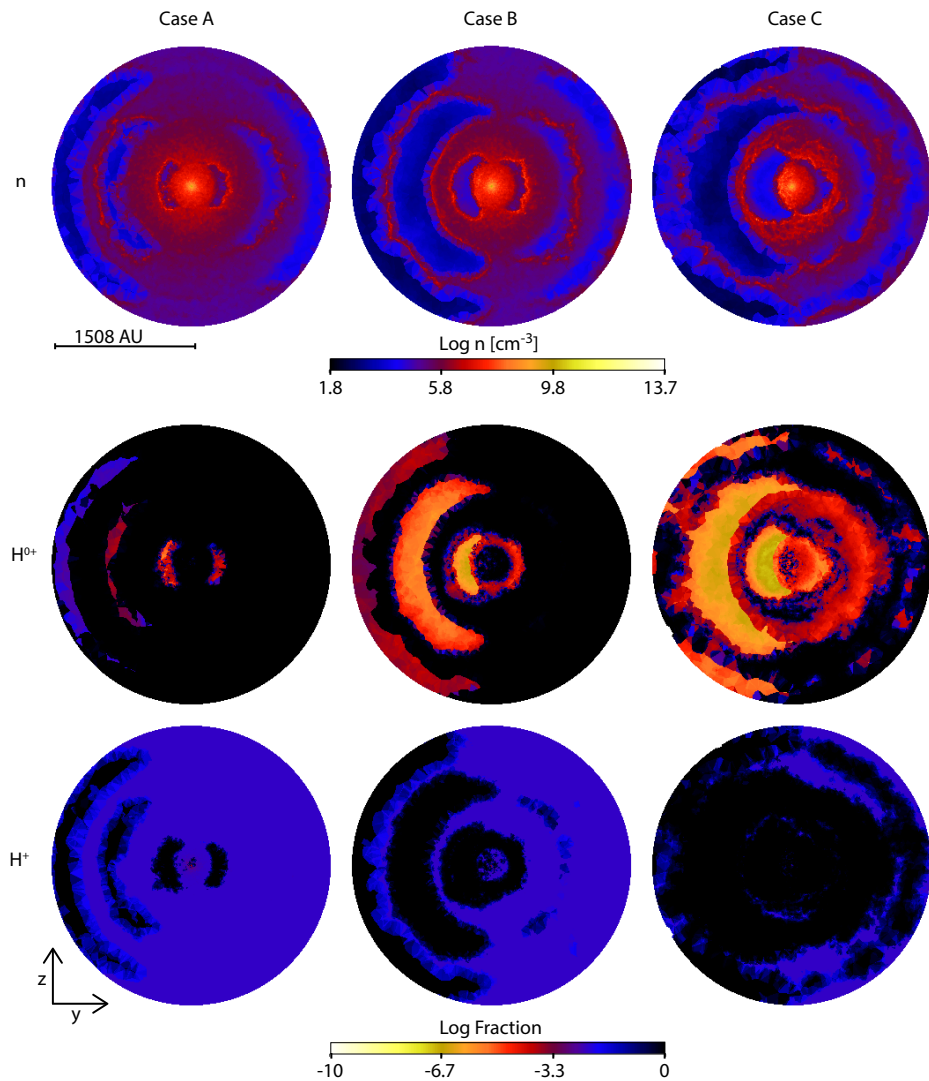
Figure 2.9 – Same as Figure 2.5, but for slices centred in the *yz* plane.

2.4 Discussion

A major goal of this work was to improve upon the simple approach of M12 for computing the highly-ionized regions in the η Car system where various observed forbidden emission lines form. The ionization volumes in M12 were based on geometrical criteria combined with a density threshold, and considered only photoionization of hydrogen due to η_B. Figure 2.11 shows an example of the photoionization region in the orbital plane
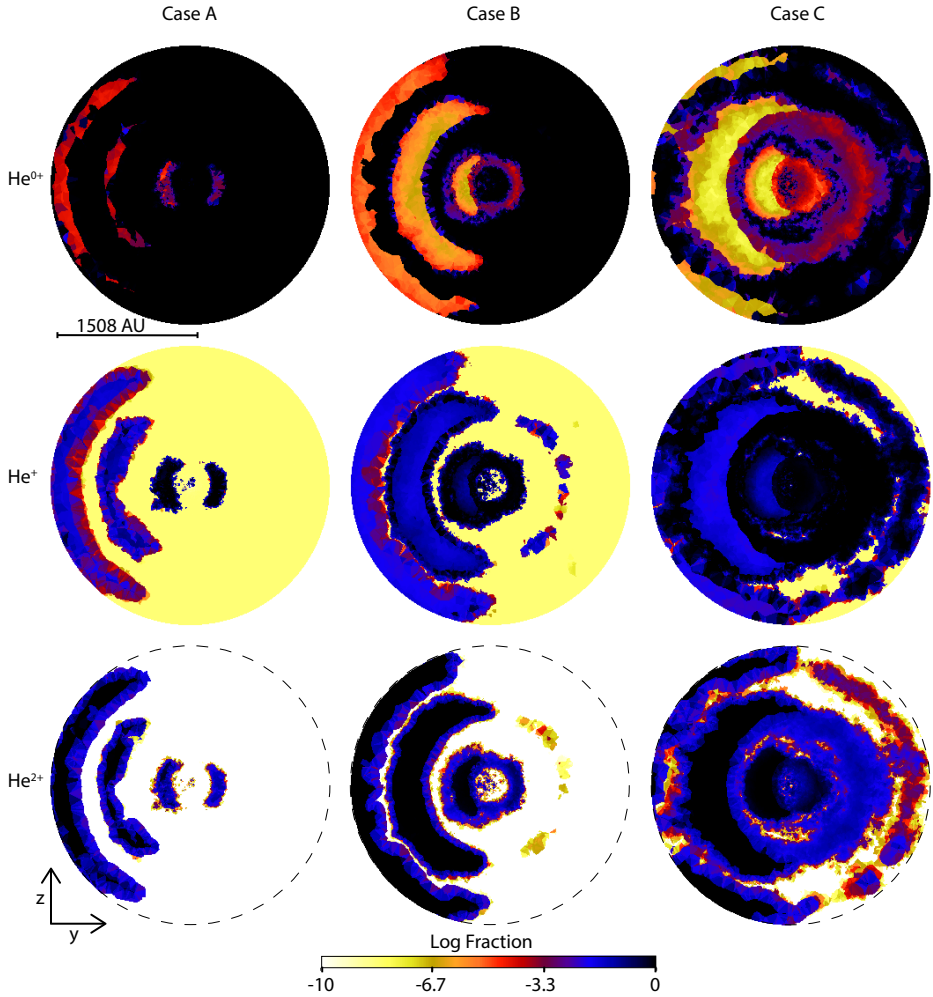
Figure 2.10 – Same as Figure 2.6, but for slices centred in the *yz* plane.

for Case A at a phase near apastron, computed using the methods of M12. The result is a rather large Strömgren-sphere-like volume that predicts the distance that H^{0+} ionizing photons from η_B can travel. Comparing this to the SIMPLEX results in Figures 2.5 and 2.6 we clearly see that the SIMPLEX method does a significantly improved job at computing the detailed structure of the various ionization volumes, including the penetration of η_B's photons into the fingers of low-density wind carved within the optically-thick wind of η_A. The approach of M12 does not account for the extended WWIR arcs on the apastron side and thus overestimates the ionization extent in these regions.

Effects due to collisional ionization and recombination were also not considered by M12. In addition to missing details in the ionization of the low-density fingers of η_B wind

Figure 2.11 – Slice in the *xy* orbital plane showing the hydrogen photoionization region created by η_B (white = ionized) for the Case A simulation at apastron, computed using the approach in M12.
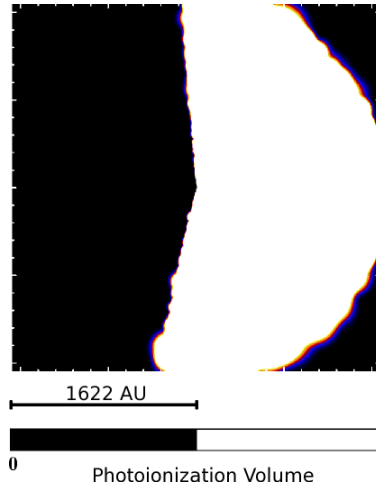
on the apastron side, subtle variations in the ionization of η_A's wind and the WWIRs on the periastron side, due to recombination, are also absent in the M12 results. More importantly, the M12 model does not compute any ionization fractions. The ion fraction is estimated using tables and assuming collisional ionization equilibrium. In contrast, the SimpleX method computes detailed ionization fractions for both hydrogen and helium. This provides estimates of the extent and magnitude of the ionization as a function of energy, previously unavailable information that is important for determining where the forbidden lines of different ionization potential form. Such information is also crucial for placing constraints on η_B's ionizing flux.

M12 found that the observed broad forbidden line emission (Gull et al. 2009, 2011) depends strongly on $\dot{M}_{\eta_A}$ and the ionizing flux from η_B. M13 suggested that if the flux from η_B remains constant, but $\dot{M}_{\eta_A}$ drops by a factor of 2 or more from an initial value of $\approx 8.5 \times 10^{-4}$ M$_\odot$ yr^{-1}, then the photoionization region created by η_B should increase considerably in size. The results of the SimpleX simulations in Figures 2.5–2.10 confirm this, implying that any recent decrease in $\dot{M}_{\eta_A}$ (as speculated by e.g. Mehner et al. 2010, 2011, 2012) should greatly change the spatial extent, location, and flux of the observed broad high-ionization forbidden emission lines. The results of this paper will be used in future work to compute synthetic slit-spectral observations of various forbidden lines (e.g. [Fe ii], [Fe iii]) for comparison to recent (Gull et al. 2011; Teodoro et al. 2013) and planned observations of η Car from *HST*/STIS. Comparison of the synthetic and observational data can be used to place additional constraints on any recent changes in $\dot{M}_{\eta_A}$, important for determining η Car's near- and long-term fates (M13). The improved SimpleX models will also be useful for refining the orbital orientation parameters obtained by M12, and possibly also the stellar wind parameters and/or wind momentum ratio.

2.5   Summary and Conclusion

We showed that using SIMPLEX for the post-processing of 3D SPH simulation output is a viable method to investigate the ionization state of the gas in a complicated colliding wind binary like η Car. SIMPLEX provides detailed 3D results of the ionization volumes and fractions for various species of interest, in this case hydrogen and helium, and improves greatly upon simpler approaches such as that in M12. Below, we summarize our most important results.

1. The unstructured SIMPLEX mesh reproduces everywhere the features present in the original 3D SPH simulation data, leading to a density map that is in excellent agreement with the original SPH one, even where sharp gradients are present. SIMPLEX also preserves the high spatial resolution of the original SPH data.

2. The inclusion of collisional ionization changes the ionization structure of hydrogen and helium most notably in the underdense fingers of η_B wind that form between the dense shells of η_A wind created every periastron passage. Since these regions are typically shielded from η_B's ionizing flux, including collisional ionization is important to achieve a more complete description of the total ionized volume.

3. Collisional ionization is important in reducing the total optical depth within regions composed of hot η_B wind that are heated to high temperatures by the various wind–wind collisions. This increases the efficiency of photoionization by η_B, allowing portions of the dense areas of post-shock η_A wind and WWIRs on the apastron side of the system to be ionized to varying degrees.

4. The SIMPLEX simulations show that the dense, innermost WWIR prevents the η_B ionizing radiation from penetrating far into the inner wind of η_A. At phases near apastron, hydrogen and helium ionization are concentrated on the apastron side of the system, with the periastron side consisting of mostly neutral η_A wind. However, as $\dot{M}_{\eta_A}$ is decreased, low-density fingers of ionized η_B wind penetrate the dense η_A wind on the periastron side.

5. We find regions of He^{2+} correlate strongly with regions of H^+, while regions of H^{0+} strongly correlate with those of He^{0+}. He^+ is more complex and primarily marks the transition between the regions of He^{0+} and He^{2+}. He^+ appears to be an excellent tracer for the dense, compressed post-shock η_A gas and WWIRs.

6. Changing $\dot{M}_{\eta_A}$ results in quite different ionization volumes, with much more ionized gas present for lower $\dot{M}_{\eta_A}$. Significant variations in ionization structure due to changes in $\dot{M}_{\eta_A}$ are clearly apparent in the *xz* and *yz* planes as well as the orbital plane.

7. The large apparent changes in ionization volume with decreasing $\dot{M}_{\eta_A}$ imply that any major decrease in $\dot{M}_{\eta_A}$ should lead to significant observable changes in the spatial extent, location, and flux of the broad high-ionization forbidden emission lines. Future

models based on the SıмρLeX results may be used to constrain any such potential changes.

In addition to helping us understand η Car's recent mass-loss history, the past (Gull et al. 2011; Teodoro et al. 2013) and future *HST*/STIS spatial maps of η Car's high-ionization forbidden emission lines are a powerful tool that can potentially be used to better determine the nature of the unseen companion star η_B. Specifically, detailed 3D models of the forbidden line emission based on SıмρLeX results like those presented here may allow us to place tighter constraints on η_B's ionizing flux. This could then be compared to stellar models for a range of O (Martins, Schaerer & Hillier 2005) and WR (Crowther 2007) stars, providing a more accurate estimate of η_B's luminosity and temperature.

While applied here to the specific case of η Car, SıмρLeX can be used to study numerous other colliding wind binaries or similar systems of astrophysical interest. Application of the SıмρLeX algorithm is also not limited to the post-processing of SPH simulation data, output from grid-based codes that use adaptive mesh refinement may also be analysed using SıмρLeX (Kruip 2011). And although SıмρLeX has been used in this paper to post-process hydrodynamical simulation data, this work helps set the stage for a future coupling of SıмρLeX with the SPH method in order to perform 3D time-dependent radiation-hydrodynamics simulations of complex astrophysical phenomena (see e.g. Pelupessy et al. 2013).

3D radiative transfer simulations of η Carinae's inner colliding winds – I: Ionization structure of helium at apastron

The highly eccentric binary system Eta Carinae shows numerous time-variable emission and absorption features. These observational signatures are the result of interactions between the complex three-dimensional (3D) structure due to the wind–wind collision and photoionization by the luminous stars. Specifically, helium presents several interesting spectral features that provide important clues on the geometry and physical proprieties of the system and the individual stars. We use the SimpleX algorithm to post-process 3D smoothed particle hydrodynamics simulation output of the interacting winds in η Car, to obtain the fractions of ionized helium assuming three different primary star (η_A) mass-loss rates. The resultant ionization maps constrain the regions where helium is singly and doubly-ionized. We find that reducing η_A's mass-loss rate ($\dot{M}_{\eta_A}$) increases the volume of singly-ionized He. Lowering $\dot{M}_{\eta_A}$ produces large variations in the volume of He^+ in the pre-shock η_A wind on the periastron side of the system. Our results shows that binary orientations in which apastron is on our side of the system are more consistent with available observations. We suggest that small variations in $\dot{M}_{\eta_A}$ might explain the observed increase in He I absorption in recent decades, although numerous questions regarding this scenario remain open. We also propose that the absence of broad He I lines in the spectra of η Car between its 1890's eruption and $\sim$ 1944 might be explained by η_B's He^{0+}-ionizing photons not being able to penetrate the wind-wind interaction region, due to a higher $\dot{M}_{\eta_A}$ at that time (by a factor $\gtrsim 2$, compared to the present value).

N. Clementel, T. I. Madura, C. J. H. Kruip, J.-P. Paardekooper and T. R. Gull

3.1 Introduction

Eta Carinae (η Car) is probably most famous for its 'Great Eruption' in the 1840s, when it temporarily became the second brightest non-solar-system object in the sky and ejected ~ 10–40 M$_\odot$, forming the dusty bipolar 'Homunculus' nebula (Davidson & Humphreys 1997; Smith et al. 2003; Gomez et al. 2010; Steffen et al. 2014). Near the center of the Homunculus lies η Car itself, an extremely luminous ($L_{\text{Total}} \gtrsim 5 \times 10^6$ L$_\odot$) and highly eccentric ($e \sim 0.9$) binary with a 5.54 yr orbit (Damineli, Conti & Lopes 1997; Hillier et al. 2001; Damineli et al. 2008a,b; Corcoran et al. 2010). The primary component, η_{A}, is a Luminous Blue Variable (LBV) and our closest example of a supermassive star ($D = 2.3$ kpc, $M_\star \sim 100$ M$_\odot$, $T_{\text{eff}} \simeq 9400$ K; Hillier et al. 2001; Smith 2006). The secondary, η_{B}, is thought to be a hotter ($T_{\text{eff}} \simeq 36{,}000$–$41{,}000$ K), but less luminous ($L_\star / $ L$_\odot \approx 10^5$–10^6), O- or Wolf Rayet-type star (Pittard & Corcoran 2002; Verner, Bruhweiler & Gull 2005; Hillier et al. 2006; Teodoro et al. 2008; Mehner et al. 2010).

Because they are so luminous, both components of η Car have powerful radiation-driven stellar winds. Multiwavelength observations obtained over the last two decades (Corcoran 2005; Hamaguchi et al. 2007; Damineli et al. 2008b; Henley et al. 2008; Groh et al. 2010b; Corcoran et al. 2010; Gull et al. 2009, 2011; Teodoro et al. 2013) indicate that η_{A}'s slow, extremely dense wind ($v_\infty \approx 420$ km s^{-1}, $\dot{M}_{\eta_{\text{A}}} \approx 8.5 \times 10^{-4}$ M$_\odot$ yr^{-1}; Hillier et al. 2001; Groh et al. 2012a) collides with η_{B}'s less dense ($\dot{M}_{\eta_{\text{B}}} \approx 1.4 \times 10^{-5}$ M$_\odot$ yr^{-1}), but much faster ($v_\infty \approx 3000$ km s^{-1}; Pittard & Corcoran 2002; Parkin et al. 2009), wind. This wind–wind collision (WWC) produces the shock-heated gas responsible for the observed time-variable 2–10 keV X-ray emission (Pittard & Corcoran 2002; Corcoran 2005; Hamaguchi et al. 2007; Okazaki et al. 2008; Corcoran et al. 2010; Parkin et al. 2009, 2011; Hamaguchi et al. 2014) that is a key signature of a colliding wind binary (Luo, McCray & Mac Low 1990; Stevens, Blondin & Pollock 1992).

The WWC, orbital motion, and presence of η_{B} lead to numerous other forms of time-variable emission and absorption seen across a wide range of wavelengths (see e.g. Damineli et al. 2008a). Observational signatures that arise as a result of the WWC and η_{B}'s ionizing radiation are important for studying η Car as they provide crucial information about the physical properties of the stars and the system as a whole. Three-dimensional (3D) hydrodynamical simulations show that the fast wind of η_{B} has a significant impact on shaping the wind of η_{A} (Okazaki et al. 2008; Madura 2010; Parkin et al. 2011; Madura & Groh 2012; Madura et al. 2012, 2013; Russell 2013), affecting greatly the observed optical and ultraviolet (UV) spectra of the system, as well as the interpretation of various line profiles and interferometric observables (Groh et al. 2010a,b, 2012a,b). Recently, Clementel et al. (2014a, hereafter Chapter 2) presented 3D radiative transfer (RT) simulations that illustrate the effects of η_{B}'s ionizing radiation on the outer regions of η Car's extended ($r \approx 1500$ au) colliding winds. However, to date there has been no detailed 3D RT modelling to determine the effects of η_{B}'s ionizing radiation on η_{A}'s inner wind, the inner wind–wind interaction region (WWIR), or the numerous observed emission and absorption lines that arise in the inner ~ 150 au of the system.

A very important series of spectral features that have fascinated and perplexed researchers of η Car for decades are those due to helium. It was the periodic variation of the He I $\lambda 10830$ emission line that originally led to the discovery of binarity in η Car (Damineli 1996; Damineli, Conti & Lopes 1997), and it is the disappearance of the narrow emission-line component of He I $\lambda 6678$ that is typically used to define the starting point of a 5.54 yr spectroscopic cycle (Damineli et al. 2008b). Present-day broad wind lines of He I, most notably $\lambda 7067$, are thought to be excited by the UV radiation of η_B and arise somewhere in/near the WWIR between the stars (Nielsen et al. 2007; Damineli et al. 2008b). Since the He I lines are recombination lines, they are produced in regions of He^+ rather than regions of neutral He. The locations of the strongest broad He I emission features are spatially unresolved in *Hubble Space Telescope* (*HST*) data, and almost certainly originate less than ~ 100–200 au from η_A (Humphreys, Davidson & Koppelman 2008). The broad He I emission lines are consistently blueshifted throughout most of the 5.54 yr orbit and exhibit an interesting double peak profile that varies in intensity and velocity, especially across periastron passage (Nielsen et al. 2007).

The broad He I P Cygni absorption components also vary in velocity and strength over η Car's entire 5.54 yr period. The He I absorption is strongest in the two-year interval centered on periastron, and relatively weak at other phases (Nielsen et al. 2007). The absorption is always blueshifted, and hence must be produced by material between the observer and the continuum source η_A, although there is still some debate over whether the absorption is directly related to material in the WWIR (Damineli et al. 2008b) or produced by the pre-shock wind of η_A (Nielsen et al. 2007).

Further complicating the story is the observed gradual increase in the amount of P Cygni absorption over the last ~ 10 yr. Since 1998, and most especially after the 2009 event, the strength of the He I absorption has increased compared to similar phases of previous cycles, while the emission strength has remained essentially unchanged (Groh & Damineli 2004; Mehner et al. 2010, 2012). Mehner et al. (2012) attribute this and other recent observed changes to a gradual decrease of η_A's mass loss rate by a factor of ~ 2–3 between 1999 and 2010. It is hypothesized that this decrease in η_A mass loss rate led to important changes in the ionization structure of η_A's wind and the WWIRs, as caused by the presence of η_B (see e.g. Figure 5 of Mehner et al. 2012). However, this idea has yet to be quantitatively tested or modelled, and the results of 3D smoothed particle hydrodynamic (SPH) simulations appear to argue against such a large, gradual change in η_A's mass loss rate (see Madura et al. 2013, hereafter M13).

Finally, there is the mystery regarding the origin of η Car's He II $\lambda 4686$ emission, which is only seen strongly around periastron (between phases ~ 0.98 and 1.03; Steiner & Damineli 2004; Martin et al. 2006; Mehner et al. 2011; Teodoro et al. 2012). The locations and physical mechanisms that give rise to this emission in η Car are not completely agreed upon, although several possible scenarios have been proposed (Steiner & Damineli 2004; Martin et al. 2006; Mehner et al. 2011; Teodoro et al. 2012; M13). The key difficulty with determining which scenario, if any, is correct is the lack of any detailed quantitative modelling of the 3D ionization structure of the innermost stellar winds and WWIR.

The goal of this paper is to compute full 3D RT simulations of the effects of η_B's ionizing radiation on η Car's inner winds and WWIR, focusing on the ionization structure of helium at orbital phases around apastron (i.e. the spectroscopic high state; Gull et al. 2009). The ionization structure of helium at periastron (the spectroscopic low state) is investigated in a subsequent paper (Chapter 3). We apply the SimpleX algorithm for 3D RT on an unstructured Delaunay grid (Ritzerveld & Icke 2006; Ritzerveld 2007; Paardekooper, Kruip & Icke 2010; Paardekooper et al. 2011; Kruip et al. 2010) to recent 3D SPH simulations of η Car's binary colliding winds that include orbital motion, radiative cooling, and radiative forces (M13). Using SimpleX we obtain detailed ionization fractions of helium at the resolution of the original SPH simulations. This should help us determine much more precisely where, and to what extent, the various emission and absorption components of the observed broad helium lines can form. This paper lays the foundation for future work aimed at generating synthetic spectra for comparison to observational data. We note that we focus solely on interpreting the *broad* emission and absorption features of helium that arise in the stellar winds and WWIRs, and not the much narrower ($\lesssim 50\,\mathrm{km\,s^{-1}}$) features that form in the Weigelt blobs and other dense, slow-moving near-equatorial circumstellar ejecta (Weigelt & Ebersberger 1986; Damineli et al. 2008b).

We describe our numerical approach, including the SPH simulations, the SimpleX code, and the RT simulations in Section 3.2. Section 3.3 describes the results. A discussion of the results and their implications is in Section 3.4. Section 3.5 summarizes our conclusions and outlines the direction of future work.

3.2   Methods

3.2.1   The 3D SPH simulations

The hydrodynamical simulations used in this work correspond to the three small-domain ($r = 10a = 155$ au) 3D SPH simulations of M13. This computational domain size was chosen in order to investigate, at sufficiently high resolution, the structure of η Car's inner WWIRs and their effects on η_B's ionizing radiation since the 'current' interaction between the two winds occurs at spatial scales comparable to the semi-major axis length $a \approx 15.4$ au ≈ 0.0067 arcsec at $D = 2.3$ kpc. In the following, we briefly describe only the essential aspects of the SPH code and setup. We refer the reader to M13 and references therein for further details.

Radiative cooling is implemented using the Exact Integration Scheme of Townsend (2009), with the radiative cooling function $\Lambda(T)$ calculated using Cloudy 90.01 (Ferland et al. 1998) for an optically thin plasma with solar abundances. The pre-shock stellar winds and rapidly-cooling dense gas in the WWIRs are assumed to be maintained at a floor temperature $= 10^4$ K due to photoionization heating by the stars (Parkin et al. 2011). Radiative forces are incorporated via the 'antigravity' formalism described in M13 and Russell (2013). We parametrize the stellar winds using the standard 'beta-velocity law' $v(r) = v_\infty(1 - R_\star/r)^\beta$, where v_∞ is the wind terminal velocity, $R_\star$ the stellar radius, and

Table 3.1 – Stellar, wind, and orbital parameters of the 3D SPH simulations

Parameter	η_A	η_B
$M_\star$ (M$_\odot$)	90	30
$R_\star$ (R$_\odot$)	60	30
$\dot{M}$ (10^{-4} M$_\odot$ yr^{-1})	8.5, 4.8, 2.4	0.14
v_∞ (km s^{-1})	420	3000
η	0.12, 0.21, 0.42	
P_{orb} (d)	2024	
e	0.9	
a (au)	15.45	

Notes: $M_\star$ and $R_\star$ are the stellar mass and radius. $\dot{M}$ and v_∞ are the stellar-wind mass-loss rate and terminal speed, respectively. $\eta \equiv (\dot{M}v_\infty)_{\eta_B}/(\dot{M}v_\infty)_{\eta_A}$ is the secondary/primary wind momentum ratio, P_{orb} is the orbital period, e is the eccentricity, and a is the length of the orbital semimajor axis.

β ($= 1$) a free parameter describing the steepness of the velocity law. Effects due to radiative braking (Gayley, Owocki & Cranmer 1997; Parkin et al. 2011), photospheric reflection (Owocki 2007), and self-regulated shocks (Parkin & Sim 2013), are not included since such effects are not expected to play a prominent role in η Car (Parkin et al. 2009, 2011; Russell 2013; M13). We include the more important velocity-altering effects of 'radiative inhibition' (Stevens & Pollock 1994; Parkin et al. 2009, 2011). However, possible changes to the mass-loss rates due to radiative inhibition are not included. These are not expected to be significant in η Car and should not greatly affect our results or conclusions (M13).

We use a standard *xyz* Cartesian coordinate system and set the orbit in the *xy* plane, with the origin at the system centre of mass and the major axis along the *x*-axis. The stars orbit counter-clockwise when viewed from along the $+z$-axis. By convention, $t = 0$ ($\phi = t/2024 = 0$) is defined as periastron. Simulations are started at apastron and run for multiple consecutive orbits.

The outer spherical simulation boundary is set at $r = 10a$ from the origin. Particles crossing this boundary are removed from the simulations. The adopted simulation parameters (Table 3.1) are consistent with those derived from the available observations, although there is some debate on the present-day value of $\dot{M}_{\eta_A}$ (see M13 for details). In an attempt to better constrain $\dot{M}_{\eta_A}$, M13 performed a series of 3D SPH simulations assuming three different $\dot{M}_{\eta_A}$. We use the same naming convention as M13 when referring to the SPH and S_IMPLE_X simulations in this paper, namely, Case A ($\dot{M}_{\eta_A} = 8.5 \times 10^{-4}$ M$_\odot$ yr^{-1}), Case B ($\dot{M}_{\eta_A} = 4.8 \times 10^{-4}$ M$_\odot$ yr^{-1}), and Case C ($\dot{M}_{\eta_A} = 2.4 \times 10^{-4}$ M$_\odot$ yr^{-1}).

3.2.2 The SimpleX algorithm for RT on an unstructured mesh

For the RT calculations, we post-process the 3D SPH simulation output using the S_IMPLE_X algorithm (Ritzerveld & Icke 2006; Ritzerveld 2007; Paardekooper, Kruip &

Icke 2010; Kruip et al. 2010; Kruip 2011). We employ a methodology nearly identical to that in Chapter 2, but use an updated version of SimpleX, which contains several important improvements over the version used in Chapter 2. We discuss the relevant differences in the following sections, and briefly describe the key aspects of the code and their relevance to this work. We refer the reader to Chapter 2 and references therein for further details on SimpleX and its applications.

3.2.2.1 Grid construction and density distribution

As in Chapter 2, we use the SPH particles themselves as the generating nuclei for the Voronoi–Delaunay mesh. We assign to the nucleus of each Voronoi cell the corresponding SPH density, computed using the standard SPH cubic spline kernel (Monaghan 1992). This helps ensure that the number density used in the SimpleX calculations closely matches that of the original SPH simulations. Note that this approach differs from that used in Chapter 2, wherein the SimpleX density is obtained by dividing the SPH particle mass by the corresponding Voronoi cell volume. Using the SPH kernel produces smoother densities than the Voronoi cell-volume approach, since the SPH kernel samples a larger number of particles over a larger volume, resulting in densities that are less affected by local differences in the SPH particle distribution (see Figure 3.1). Comparison with a direct visualization of the SPH density output (using splash, Price 2007, left-hand panel of Figure 3.1) shows that the SPH kernel approach indeed matches better the density distribution of the original SPH simulations. Figure 3.2 shows an example of the SimpleX mesh and number density at apastron for a representative 3D SPH simulation of η Car.
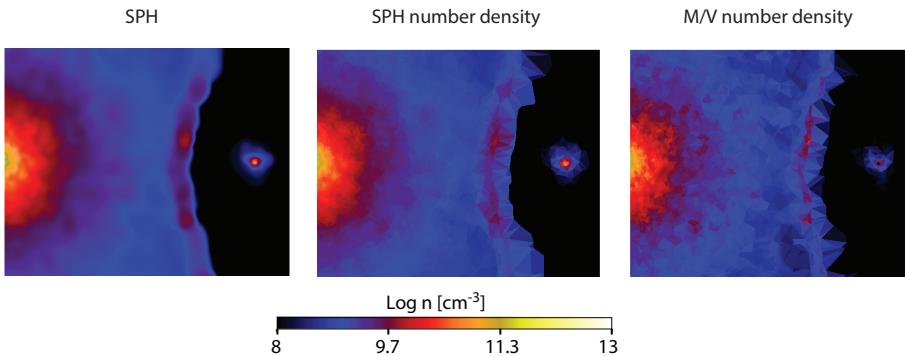

Figure 3.1 – Zoom of the central region for a slice in the *xy* orbital plane through the 3D simulation volume for the Case A simulation at apastron. Color shows number density on a logarithmic scale (cgs units) using three different visualization approaches (see Section 3.2.2.1). Left-hand panel: Direct visualization using splash. Middle panel: SPH kernel approach. Right-hand panel: SPH particle mass divided by Voronoi cell volume approach.
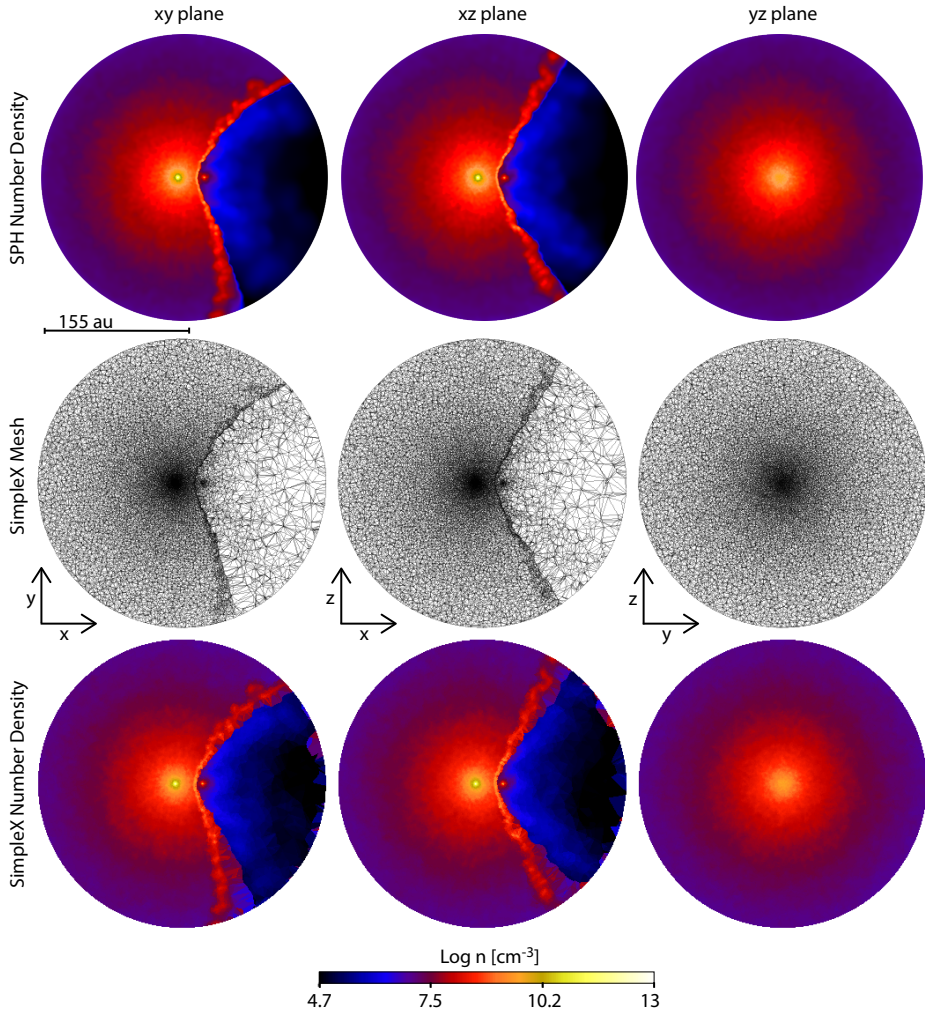
Figure 3.2 – Slices in the *xy* (left-hand column), *xz* (middle column) and *yz* (right-hand column) planes through the 3D simulation volume for the Case A simulation at apastron. Rows show, from top to bottom, the original SPH number density distribution (log scale, cgs units), the SIMPLEX mesh, and the resulting SIMPLEX number density (same log scale, cgs units). The resolution of the SIMPLEX mesh, as well the number density, follow well the resolution of the original SPH data. The length scale is shown under the top left-hand panel. In the first column (i.e. the orbital plane) η_A is to the left and η_B is to the right.

3.2.2.2 Ionization state and chemistry of the gas

As in Chapter 2, we perform the RT calculations in post-processing. We consider the ionization of hydrogen and helium atoms by both photo- and collisional ionization. The ionization rate equations are solved on a time-step smaller than the RT time-step to ensure photon conservation (Pawlik & Schaye 2008; Paardekooper, Kruip & Icke 2010). This can

lead to very small time-steps in cells where the photoionization time-scale is very small. To speed up the computation in these cells, we instead use the time-averaged optical depth to compute the photoionization rate and iterate for convergence (Mellema et al. 2006; Friedrich et al. 2012).

3.2.2.3   Treatment of the ionizing spectrum and transport method

In numerical simulations involving radiation it is necessary to approximate the continuous spectrum of radiation with a finite number of discrete frequency bins due to memory requirements. In Chapter 2 the extreme limit of a single frequency bin, commonly referred to as the 'grey approximation', was used. Although in the grey approximation all spectral information is lost, it is still possible to enforce the conservation of a quantity of importance such as the number of ionizations per unit time or the energy deposition into the medium per unit time. However, since in this work we are interested in the detailed ionization structure of He, and we want to capture the behaviour of the product of the spectrum and cross-sections in sufficient detail, we now employ three frequency bins.

The width of each frequency bin is set by the ionization energy of each species. The first bin ranges from the ionization frequency of H^{0+} ($\nu_{H^{0+}} = 3.28 \times 10^{15}$ Hz) to that of He^{0+} ($\nu_{He^{0+}} = 5.93 \times 10^{15}$ Hz), the second from $\nu_{He^{0+}}$ to ν_{He^+} (1.31×10^{16} Hz), and the third from ν_{He^+} to a maximum frequency equal to ten times $\nu_{H^{0+}}$. We use an effective cross-section representation to determine the correct number of absorptions within each frequency bin. In this case, the limits of integration in equations (2.7) and (2.8) of Chapter 2 are over the frequency range of the bin of interest.

In Chapter 2, photons were transported across the SimpleX grid using ballistic transport. With this method, the incoming direction of the photons is used to define the outgoing direction, and the outgoing photons are distributed in 3D over the three most forward edges of the Delaunay triangulation. One drawback of this approach is that, due to the random nature of the outgoing directions in the Delaunay grid, the radiation may lose track of the original incoming direction after many steps. If the cells are optically thin, this can result in a radiation field that is too diffusive, leading to overestimates of the ionization fractions. To solve this problem, the original direction of the photons is preserved by confining them to solid angles corresponding to global directions in space. This is known as direction-conserving transport (DCT) (Kruip et al. 2010; Paardekooper 2010).

In DCT, if a photon is emitted in a certain direction associated with a solid angle, it will remember this direction and, unless it interacts with atoms on the grid, it will stay in the same solid angle as it travels through the grid. This effectively decouples the directionality of the radiation field from the directions present in the grid. In this work, we use 84 directions with DCT, implying a solid angle of $\pi/21$ sr for each unit vector.

3.2.2.4   The ionizing source η_B

Based on Mehner et al. (2010), Verner, Bruhweiler & Gull (2005) and Madura et al. (2012), we consider η_B to be an O5 giant with $T_{eff} \approx 40,000$ K. We assume a total ionizing

flux for H and He of 3.58×10^{49} photons s^{-1} (Martins, Schaerer & Hillier 2005).

As described in Section 3.2.2.3, we use three bins to sample the spectrum, which we approximate with a black body. We are therefore interested in the number of ionizing photons in each bin, photons$_i$, which depends on the black body temperature:

$$\text{photons}_i = \int_0^{\lambda_i} B_\lambda (T) \mathrm{d}\lambda, \tag{3.1}$$

where the λ_i are the limiting wavelengths for the ionization of H^{0+} ($\lambda = 912$ Å), He^{0+} ($\lambda = 504$ Å) and He$^+$ ($\lambda = 228$ Å), and B_λ is the Planck spectrum

$$B_\lambda (T) \propto (\lambda^5 \exp[hc/(\lambda k_B T)])^{-1}. \tag{3.2}$$

In Martins, Schaerer & Hillier (2005), the fluxes able to ionize H and He are defined as

$$q_i = \int_0^{\lambda_i} \frac{\pi \lambda F_\lambda}{hc} \mathrm{d}\lambda, \tag{3.3}$$

where F_λ is the flux expressed in erg/s/cm^2/Å. We set the black body temperature to the value that produces the correct ratio photons$_{\text{H}^{0+}}$/photons$_{\text{He}^{0+}}$ (in this case $T_{\text{bb}} = 49,000$ K), in accordance to the $q_{\text{H}^{0+}}/q_{\text{He}^{0+}}$ ratio in Martins, Schaerer & Hillier (2005). q_{He^+} is effectively zero for η_{B}.

3.2.2.5 Visualization of the unstructured mesh results

When visualizing the SIMPLEX simulation output, we would ideally like to render physical quantities that are centred on the original Voronoi cells that compose our 3D unstructured grid. Unfortunately, the Voronoi cells consist of a series of irregular n-sided polygons, which makes their visualization quite complex. Instead, it is much more straightforward to visualize the corresponding Delaunay triangulation. In 3D, the Delaunay cells are tetrahedra, which can be visualized using standard visualization tools such as VisIt[1]. Since the Delaunay cells are tetrahedra, the quantity we visualize is the average of the four vertices that define the tetrahedron cell (i.e. the average of the four Voronoi nuclei). This approach works well for visualizing most physical quantities (e.g. temperature, density, velocity). However, if neighbouring Voronoi nuclei have values which are significantly different (i.e. by several orders of magnitude), this 'volume-average' approach may lead to tetrahedral-cell values that are difficult to interpret.

Unfortunately, the fractions of He^{0+}, He$^+$, and He^{2+} can span ten or more orders of magnitude across the WWIR in η Car. The volume-averaged fractions in the larger grid cells that define the post-shock secondary wind can therefore be difficult to understand, especially when a logarithmic color scale is used (see Figure 3.3). As an example, consider
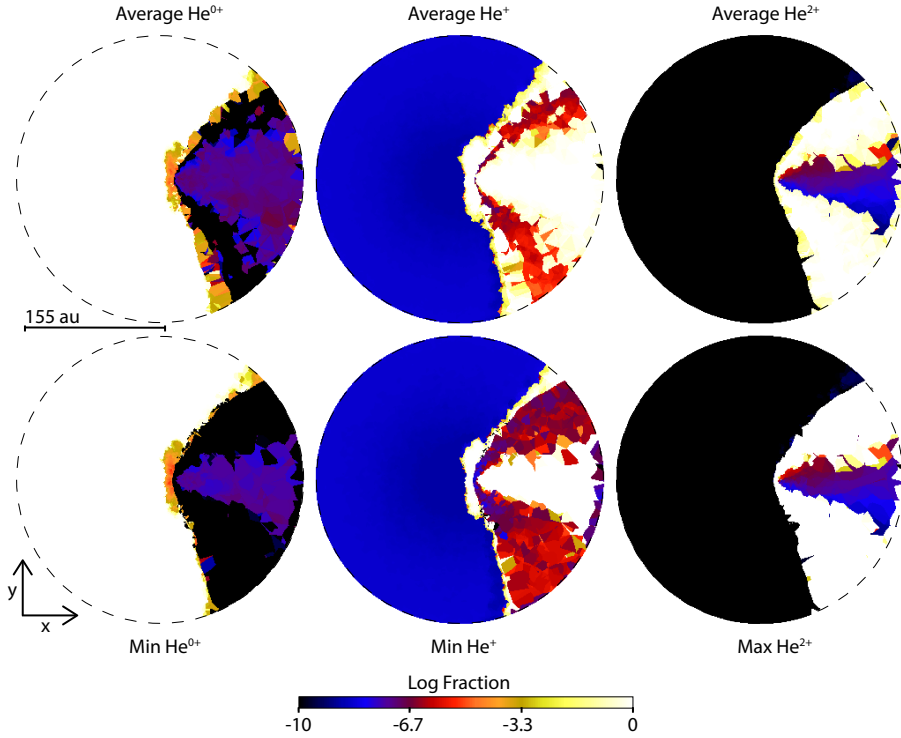
---

[1]https://wci.llnl.gov/codes/visit/home.html

Figure 3.3 – Slice in the *xy* orbital plane through the 3D simulation volume for the Case A simulation at apastron. Columns show, from left to right, the computed fractions of He^{0+}, He^+ and He^{2+} (log scale). Images in the top row were computed using the volume average approach (see Section 3.2.2.5). Images in the bottom row show, from left to right, the minimum He^{0+}, minimum He^+ and maximum He^{2+} values and extents. In this and future plots, the dashed circle marks the edge of the spherical computational domain.

the fraction of He^+ near the contact discontinuity in the WWIR. If three of the vertices of a tetrahedron cell are highly ionized and have extremely low fractions of He^+ ($\lesssim 10^{-10}$), while the fourth vertex has a large fraction of He^+ (≈ 1), the final He^+ fraction visualized over the *entire* cell will be ~ 0.25. This simply tells us that $\sim 25\%$ of the cell's volume is He^+. The problem is that the visualization of the He^+ fraction alone tells us nothing about *which* $\sim 25\%$ of the cell volume is He^+, nor does it tell us directly what percentage of the remaining $\sim 75\%$ of the cell volume is He^{0+} or He^{2+}. Therefore, while correct, the visualized plots of various ionization fractions can be deceiving, since for certain species they give the appearance of physically incorrect locations for the ionization fronts. In our He^+ example, there appears to be a thick region of He^+ near the contact discontinuity in the hot, post-shock secondary wind (top middle panel of Figure 3.3), even though the gas in this region is extremely hot ($\gtrsim 10^6$ K, see Figure 3.5), and should consist entirely of He^{2+}.

Therefore, instead of the average, we show the minimum vertex value for the fraction

of He^{0+} and the maximum vertex value for the fraction of He^{2+}. For He^+, we show the maximum value whenever the tetrahedron consists of vertices that are only from the primary wind, and the minimum otherwise (if we were to simply show the minimum of the He^+ fraction everywhere, we would underestimate the penetration of η_B's He-ionizing radiation into η_A's pre-shock wind). This choice for visualizing our simulations shows an *upper* limit to the ionization state of He, in the sense that it shows the maximum extent of the ionization front (bottom row of Figure 3.3). By using this approach, the ionization structure of He much better follows the temperature structure of the gas (Figure 3.5) in places where collisional ionization dominates. Therefore, the physics in our simulations is more truthfully represented. We emphasize that the visualizations are merely to help guide the reader, and neither the physics nor the conclusions of our work depend on them.

3.2.3 Application to η Car

We focus on the ionization of He at an orbital phase of apastron assuming the same abundance by number of He relative to H as Hillier et al. (2001), $n_{He}/n_H = 0.2$. We employ a single photoionizing source located at the position of η_B. Details on the nature and implementation of the η_B spectrum are described in Section 3.2.2.4.

Collisional ionization equilibrium of the SPH simulation snapshot is used as an initial condition for the SimpleX simulations. The SPH output is post-processed with SimpleX until the ionization state reaches an equilibrium value (this typically happens within ~ 1–2 months of simulation time). We use a simulation time-step of ~ 5 min, which is sufficiently small for accurate RT calculations of the ionization volumes and fractions.

For simplicity, we neglect the influence of the WWIR X-rays on the He ionization structure at times around apastron since they are highly inefficient at ionizing He (see Chapter 2).

3.2.3.1 Influence of η_A

As in Chapter 2, we neglect the η_A ionizing source for simplicity. We also do not consider the ionization structure of hydrogen (although it is included in our calculations). In this work, we focus on the influence of η_B's He-ionizing radiation on the WWIRs and η_A's pre-shock wind. Hillier et al. (2001, 2006) and Groh et al. (2012a) fitted the optical and UV spectra of η_A and computed the ionization structure of H and He within the optically-thick wind of η_A for different $\dot{M}_{\eta_A}$. They found that the H^+ region around η_A extends radially ~ 120–125 au for simulation Cases A ($\dot{M}_{\eta_A} = 8.5 \times 10^{-4}$ $M_\odot \, yr^{-1}$; see e.g. the yellow line in Figure 3.4) and B ($\dot{M}_{\eta_A} = 4.8 \times 10^{-4}$ $M_\odot \, yr^{-1}$). For Case C ($\dot{M}_{\eta_A} = 2.4 \times 10^{-4}$ $M_\odot \, yr^{-1}$), hydrogen is fully ionized throughout the entire η_A wind ($r \gtrsim 5500$ au).

Due to the smaller domain size of the simulations used in this paper ($r = 155$ au), and because η_B will fully ionize H^{0+} throughout its wind, little information is gained by examining the ionization structure of hydrogen in our simulations. In principle, we might gain information about the ionization state of H in the cold, post-shock η_A gas, but this
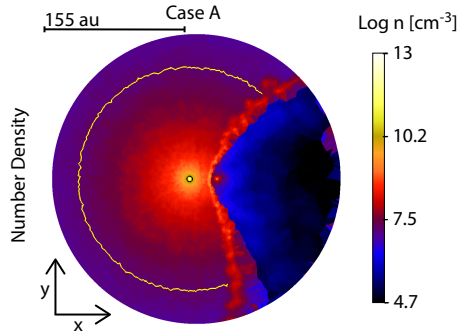
Figure 3.4 – Slice in the *xy* orbital plane through the 3D simulation volume for the Case A simulation at apastron. The black ($r = 3$ au) and yellow ($r = 120$ au) lines indicate the He^+ and H^+ ionization radii in the pre-shock η_A wind for simulation Case A, based on the `CMFGEN` models of Hillier et al. (2001, 2006) and Groh et al. (2012a). Radii for Case B are only marginally larger than shown. For Case C, the He^+ radius is comparable to the yellow line (see Figure 3.7) while H is H^+ throughout the entire simulation domain.

depends strongly on the population of the $n = 2$ state of H^{0+} in this region and the η_A ionizing source. Lower energy (10.2 eV) photons could populate the $n = 2$ state of any H^{0+} in the post-shock η_A gas, which could then be ionized to H^+ by 3.4 eV photons. Thus, it is possible that H is ionized everywhere in the inner ~ 120–150 au region around η_A, including the WWIRs.

In contrast, He is mainly neutral in the wind of η_A. As shown in Figure 3.4 (black line), the extent of the He^+ region in η_A's wind, for Cases A ($r \sim 3$ au) and B ($r \sim 7.5$ au), is much smaller (Hillier et al. 2001, 2006; Groh et al. 2012a). The energy level structure of He is such that high-energy photons (~ 19.8 eV) are needed to populate even the lowest excited states (Nielsen et al. 2007). η_B is the only known source of such photons in η Car. He I lines are thought to represent the highly excited regions of η_A's wind and/or the WWIR (Nielsen et al. 2007). It may be the case that He^{0+}-ionizing photons from η_B are able to penetrate the WWIRs and reach the He^+ region deep within η_A's wind. The inner η_A He^+ region would be effectively transparent to such photons, which may allow them to pass through to the He^{0+} zone on the back side of η_A (the side facing away from η_B). Thus, determining the correct overall He ionization structure requires some method of mimicking the internal ionization structure of He in η_A's pre-shock wind due solely to η_A itself.

The simplest method, which we employ for this work, is to set as an initial condition to the SIMPLEX simulations the ionization structure of He^+ in η_A's inner wind. To do this, we set the temperature in the innermost η_A wind to 50,000 K, which is hot enough to fully singly-ionize He^{0+} to He^+, but not He^{2+}. The outer radius of this inner He^+ region for each simulation case is set to the appropriate value based on the 1D `CMFGEN` models of η Car by Hillier et al. (2001, 2006), namely, 3 au, 7.5 au, and 120 au for Cases A, B, and C, respectively (see Figure 3.7). We do not include the inner He^{2+} zone in η_A's wind

since in most cases it is of negligible size ($r < 1$ au), and because η_B produces essentially zero He^+-ionizing photons.

3.3 Results

Figures 3.5 and 3.6 display the number density and temperature in the orbital and *xz* planes for simulation Cases A–C. Due to the smaller spatial size of these simulations, the density and temperature structures are less complex than those described in Chapter 2. As shown by Okazaki et al. (2008), Parkin et al. (2011), Madura & Groh (2012), Madura et al. (2012, 2013), the lower-density faster η_B wind carves a large cavity out of the slower, denser wind of η_A for the majority of the orbital period. Around apastron, this cavity and the WWIR have an nearly axisymmetric conical shape, with the opening angle increasing as the value of $\dot{M}_{\eta_A}$ decreases. The apex of the WWIR also moves closer to η_A as $\dot{M}_{\eta_A}$ is lowered, due to the change in wind momentum balance. The WWIR consists, on the secondary side of the contact discontinuity (CD; right-hand side of the panels), of a distended shock containing hot ($T \gtrsim 10^6$–10^8 K) low-density η_B wind material. On the primary side of the CD, the post-shock η_A gas (green contours) is much thinner and colder ($T \approx 10^4$ K).

The bottom row of Figures 3.5 and 3.6 show that, in the orbital plane, the overall fraction of η_B's wind that is shock heated increases with $\dot{M}_{\eta_A}$, while the hottest areas (in red) increase in size as $\dot{M}_{\eta_A}$ decreases. This happens because, for a given pre-shock wind speed, more oblique shocks (i.e. Case A versus Cases B and C) produce lower post-shock temperatures (Pittard 2009; M13). It is also possible to observe an asymmetry in the temperature of the post-shock η_B gas in the leading arm of the WWIR, which is warmer in comparison to the gas in the trailing arm. This is a result of the increased pre-shock wind speed due to orbital motion. The post-shock η_A wind region appears to become slightly thinner and less dense the lower the value of $\dot{M}_{\eta_A}$, and the WWIR seems to become more unstable. However, the standard SPH schemes are known for under resolving certain hydrodynamic instabilities (Agertz et al. 2007; Price 2008), so these results should be interpreted with caution. For further details on the density and temperature structures of the winds and the effects of different $\dot{M}_{\eta_A}$, see M13.

To help provide a scale comparison with the larger domain simulations used in Chapter 2, we point out that the remnant of the expanding shell of η_A wind created during the previous periastron passage (as described in M13) is visible at the outer edge of the simulation domain on the apastron side of the system (see the shock-heated gas in the bottom row of Figures 3.5 and 3.6). Furthermore, to assist the reader in interpreting the He ionization plots, we have outlined the location of the cold, dense, post-shock η_A wind in Figures 3.5–3.8 using a green contour. Finally, we note that, as illustrated in the rightmost column of Figure 3.2, on this simulation scale, slices in the *yz* plane through the system centre of mass only sample the pre-shock wind of η_A. They thus provide little new relevant information on the ionization structure of He at apastron. Hence, we focus our
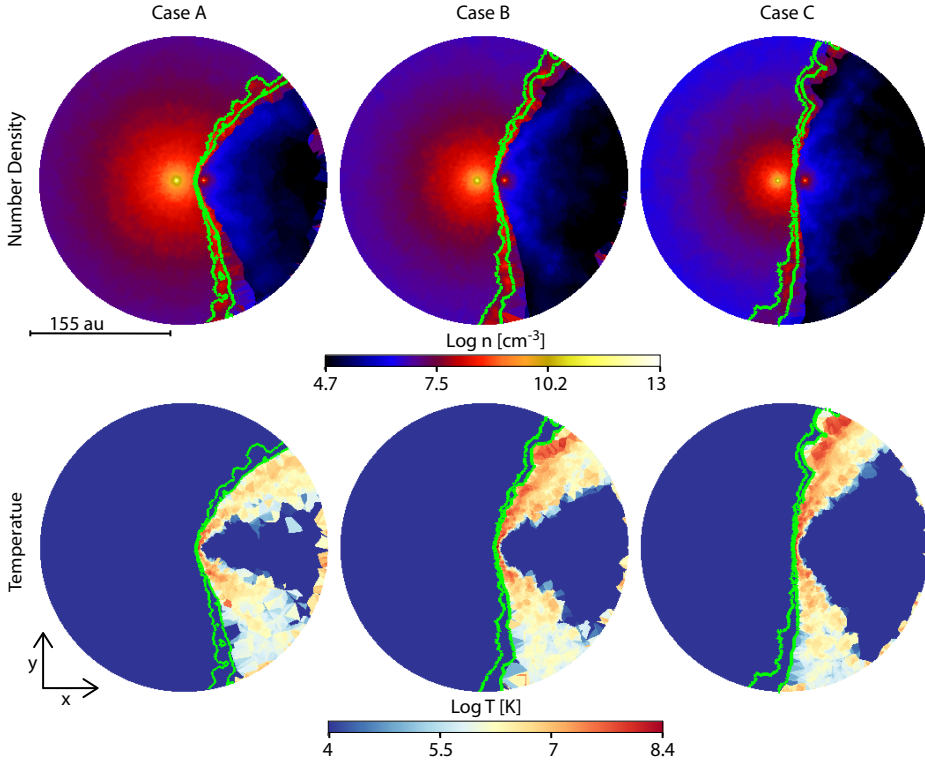
Figure 3.5 – Slices in the orbital plane through the 3D SIMPLEX simulation volume for the three different assumed $\dot{M}_{\eta_A}$ (columns, left to right; Case A $= 8.5 \times 10^{-4}$ $M_\odot$ yr^{-1}, Case B $= 4.8 \times 10^{-4}$ $M_\odot$ yr^{-1}, and Case C $= 2.4 \times 10^{-4}$ $M_\odot$ yr^{-1}). Top row shows the SIMPLEX number density (log scale, cgs units), while the bottom row shows the temperature (log scale, K). In this and future plots, the green contour highlights the location of the cold, dense, post-shock primary wind region.

discussion on the results in the orbital (*xy*, Figure 3.7) and *xz* (Figure 3.8) planes.

3.3.1 Overall He Ionization Structure and Influence of $\dot{M}_{\eta_A}$

3.3.1.1 The orbital plane

Figure 3.7 illustrates the fractions of He^{0+}, He$^+$ and He^{2+} (rows, top to bottom) in the orbital plane for the three $\dot{M}_{\eta_A}$ simulations (Cases A–C, from left to right). In all three cases, on the secondary side of the WWIR, the ionization state of the high temperature shock-heated gas is dominated by collisional ionization. At such high temperatures ($T \gtrsim 10^6$ K) helium is fully-ionized to He^{2+} (white area in the bottom row). The unperturbed expanding secondary wind located between the two arms of the WWIR is, instead, principally composed of He$^+$ due to photoionization by η_B. This is an expected difference, compared to the results in Chapter 2, connected with the better approximation of the η_B
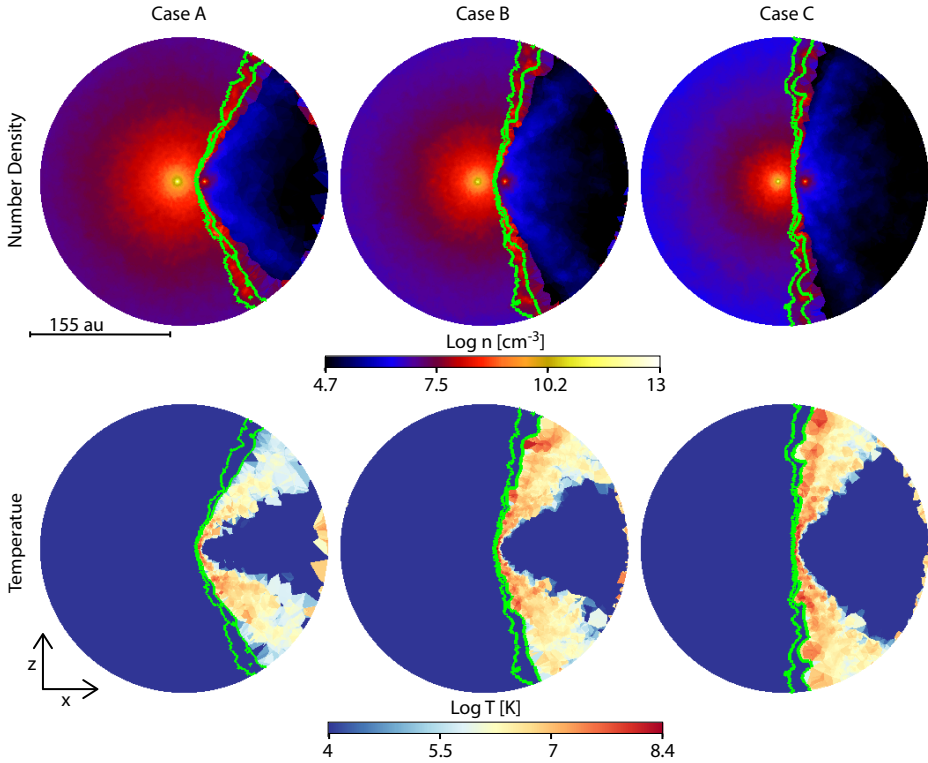
Figure 3.6 – Same as Figure 3.5, but for slices centred in the *xz* plane.

spectrum using three frequency bins. As discussed in Section 3.2.3.1, η_B should not produce many He^+-ionizing photons. Therefore, the low fraction of He^{2+} in its unshocked wind is expected. Note also that there is no He^{2+} in the pre- and post-shock primary wind, as expected. He^{2+} thus appears to be an excellent tracer of the hot, post-shock η_B wind region. One important consequence of the larger opening angle of the WWIR for lower $\dot{M}_{\eta_A}$ is an increase in the volume of the He^+ region in η_B's wind on the apastron side of the system, and an increase in the angle between the two arms of He^{2+}.

While the situation on the η_B-side of the system does not depend strongly on the value of $\dot{M}_{\eta_A}$, the He structures on the periastron (η_A) side of the system are quite different for the three $\dot{M}_{\eta_A}$. Our simulations show that the He^{0+}-ionizing photons are able to penetrate into the unperturbed primary wind to varying degrees for all $\dot{M}_{\eta_A}$, but the detailed results depend drastically on $\dot{M}_{\eta_A}$. In Case A, the He^+ structure is much smaller and closer to the WWIR apex than in Cases B–C. Aside from this central area around the apex of the WWIR, the He^+ front appears to extend only about half way into the post-shock primary wind. *Most importantly, there is no layer of He^+ in the pre-shock η_A wind that borders the entire WWIR.* This is in contrast to the simple models proposed by e.g. Martin et al. (2006),
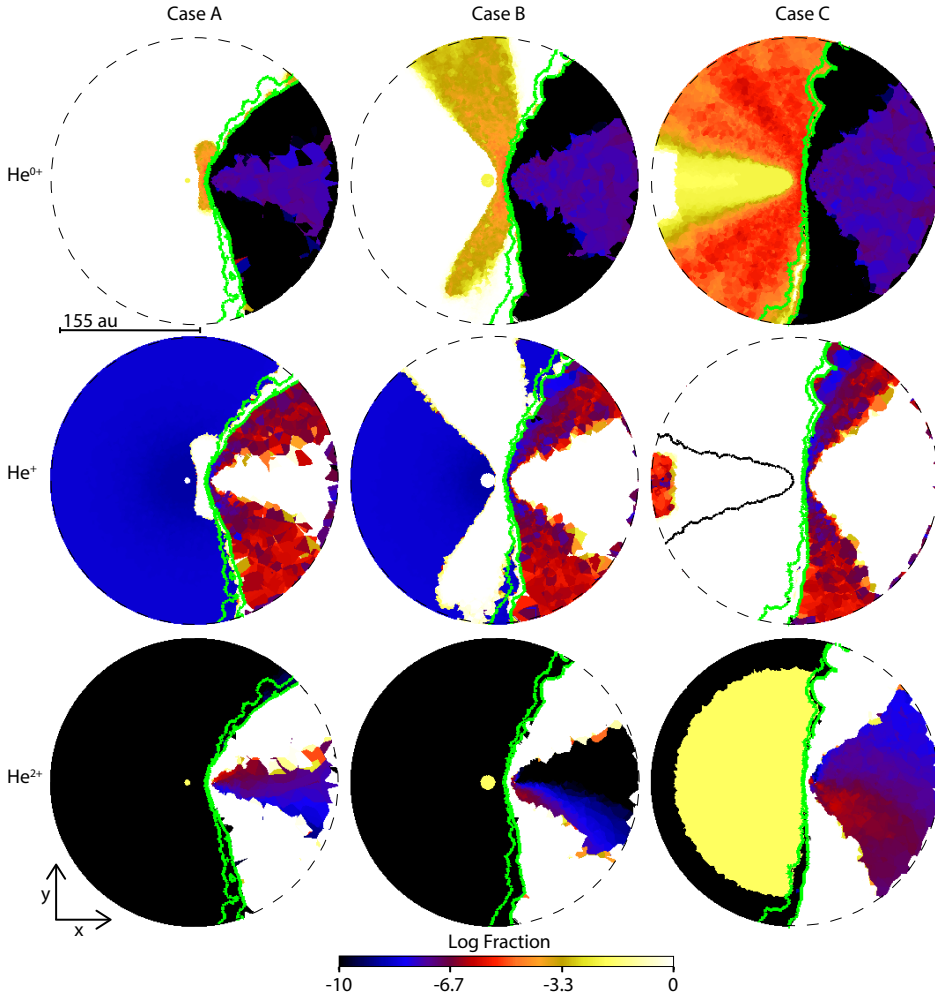
Figure 3.7 – Slices in the orbital plane through the 3D SimpleX simulation volume for the three different assumed $\dot{M}_{\eta_A}$ (columns, left to right). Rows show, from top to bottom, the computed fractions of He^{0+}, He^+ and He^{2+} (log scale). The circular ionization structure around η_A (i.e. the yellow circular areas in the He^{0+} and He^{2+} rows) is the region where we have set He to He^+ in the pre-shock primary wind (see Section 3.2.3.1). The black contour in the right-hand panel of the middle row (Case C, He^+) marks the location of the He^+ ionization front when the ionization structure of η_A's inner wind is excluded in the calculations.

Humphreys, Davidson & Koppelman (2008) and Mehner et al. (2012). The cold, dense, post-shock η_A wind, in our simulation, absorbs most of the He^{0+}-ionizing photons from η_B.

The middle row of Figure 3.7 shows that a decrease in $\dot{M}_{\eta_A}$ leads to a deeper penetration of the He^{0+}-ionizing photons into the primary wind and, consequently, a much larger volume of He^+ on the primary side of the system. η_B is able to effectively ionize a

significant volume of the primary wind in Case B, while in Case C, η_B is able to ionize He in nearly the entire pre- and post-shock primary wind (on this simulation domain scale). Note also the 'bent wing' geometry of the He^+ ionization front that penetrates into η_A's pre-shock wind in Case B, which is caused by the radial dependence of the density in η_A's wind.

The introduction of the inner He^+ region (due to η_A photoionization; Section 3.2.3.1) has no noticeable effect on the He ionization structure for Cases A and B (middle row of Figure 3.7). In both cases, He^{0+}-ionizing photons from η_B are unable to reach the deepest parts of the pre-shock primary wind. On the other hand, the much larger ionized sphere in Case C ($r = 120$ au) further increases the volume of He^+ in η_A's wind. The black line, in the right-hand panel of the middle row of Figure 3.7, marks the area that is He^{0+} when the ionization due to η_A is excluded from our calculations. As one would expect, when the influence of η_A is neglected, as $\dot{M}_{\eta_A}$ decreases, a larger volume is ionized. Only a narrow column focused directly behind and away from η_A remains neutral.

In Cases A and B, there is also a noticeable asymmetry in ionization between the leading and trailing arms of the WWIR. The leading arm shows a higher (in value) and wider (in spatial extent) presence of He^+, both in the post-shock primary wind and the unperturbed primary wind. A possible explanation for this difference might be found in the slight differences in temperature and density between the two arms. Since the leading arm of the WWIR has higher gas temperatures, He^{0+}-ionizing photons may be able to more easily penetrate the post-shock η_B gas in the leading arm, causing more ionization of the pre- and post-shock η_A wind.

3.3.1.2   The *xz* plane

Figure 3.8 shows the fractions of He^{0+}, He^+ and He^{2+} in the *xz* plane for Cases A–C. The ionization structure in this plane exhibits the same trends, as a function of $\dot{M}_{\eta_A}$, as the orbital plane. This is expected due to the nearly axisymmetric nature of the WWIR around apastron. However, there is one striking difference, namely, the structure of He^+ in the Case B simulation. In this case, the He^+ structures on the primary side of the CD are much smaller in the *xz* plane than those in the orbital plane. We speculate that this may be due to the the less turbulent nature of the WWIR in the plane perpendicular to the orbital motion. Instabilities in the WWIR may be more prevalent in the orbital plane, causing gaps to arise in the post-shock η_A wind that allow He^{0+}-ionizing photons from η_B to more easily penetrate into the pre-shock η_A wind. However, detailed studies of the 3D structure of WWIRs in regions above and below the orbital plane, and how various instabilities affect this structure, currently do not exist in the literature. Future detailed simulations of 3D WWIRs are necessary to determine if our interpretation is correct.
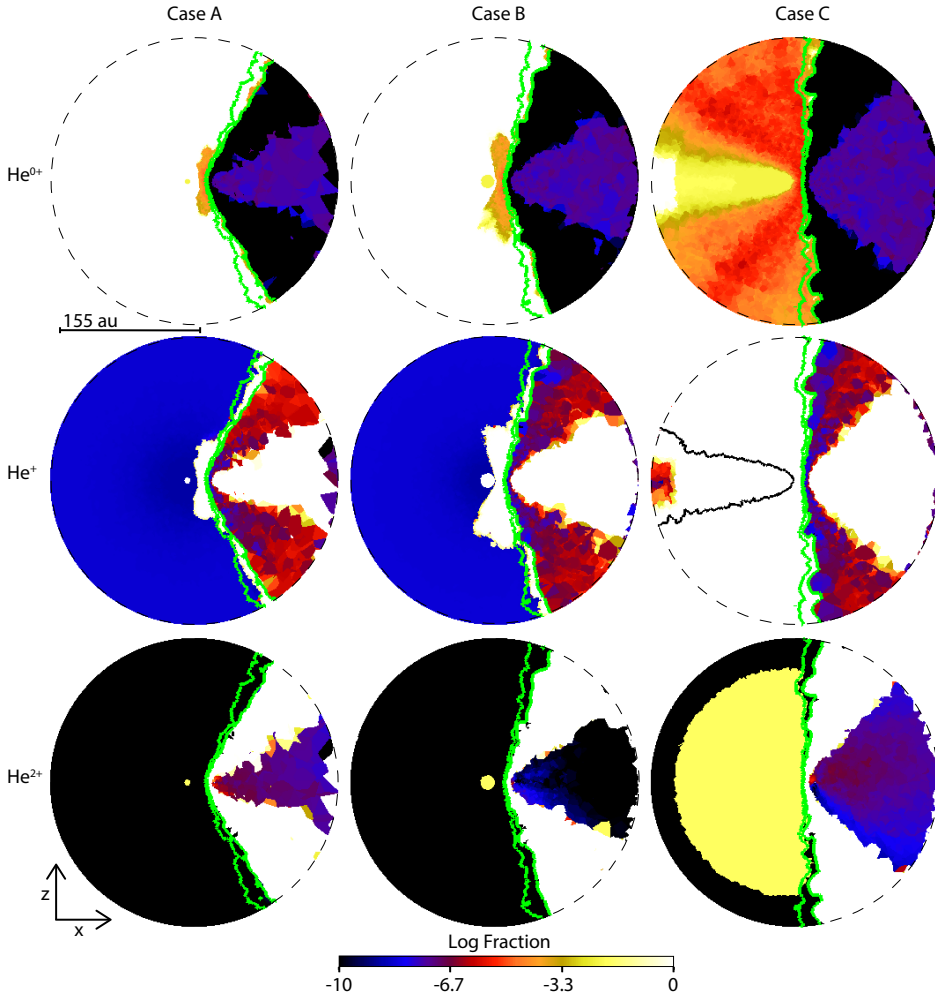
Figure 3.8 – Same as Figure 3.7, but for slices centred in the *xz* plane.

3.4   Discussion

Our Simplex results show that, assuming for η_{B} a typical ionizing flux appropriate for an O-type star with $T_{\mathrm{eff}} \approx 40{,}000$ K, η_{B} singly-ionizes He throughout its unshocked wind, as expected. Moreover, extremely high temperatures ($\gtrsim 10^6$ K) cause He to be doubly-ionized in the post-shock η_{B} gas. Our results also help rule out very low values of $\dot{M}_{\eta_{\mathrm{A}}}$ approaching 2.4×10^{-4} $M_{\odot}\,\mathrm{yr}^{-1}$. Our Case C simulations show that for such low $\dot{M}_{\eta_{\mathrm{A}}}$, η_{B} is able to singly-ionize He throughout practically our entire computational domain, including the dense pre- and post-shock primary wind regions. The ionized volume is even bigger if one includes the He ionization structure of η_{A}'s inner wind, wherein

η_A already singly-ionizes He out to a radius of ~ 120 au in its wind (Hillier et al. 2001, 2006). This makes it easier for ionizing photons from η_B to penetrate η_A's wind and enlarge the He ionization zone. In such a scenario, one would expect a significant amount of He II $\lambda 4686$ emission from the dense, ionized primary wind and WWIR, even around apastron, which is not observed (Hillier et al. 2006; Teodoro et al. 2012). The strength of the emission in the broad He I lines is also expected to be much stronger than observed if $\dot{M}_{\eta_A}$ were so low (Hillier et al. 2006).

A similar situation is envisioned in Case B, namely, stronger He I and He II emission lines compared to Case A. This is true even though the inner He^+ ionization radius produced by η_A in its wind is much smaller than in Case C. However, He^{0+}-ionizing photons are still able to penetrate the dense WWIR and ionize a significant volume of η_A's preshock wind. Determining the strength of such He emission lines in Case B is beyond the scope of this paper, so we unfortunately cannot rule out at this time that such emission would be in direct disagreement with observations. Still, we would naively expect, based on our results, significant detectable He II emission at times around apastron, which is currently not observed. Thus, Case B (4.8×10^{-4} $M_\odot \, yr^{-1}$) may represent a lower limit on the current value of $\dot{M}_{\eta_A}$.

The location of the He^+ region in our simulations provides further support for binary orientations in which apastron is on our side of the system (e.g. Damineli et al. 2008a; Okazaki et al. 2008; Parkin et al. 2009, 2011; Madura et al. 2012). The observed He I emissions in η Car are primarily blueshifted along most of the 5.5 yr cycle, and the P Cygni absorptions (which must be formed on our side of η_A, the continuum source) are weak for most of the cycle (Hillier et al. 2001, 2006; Nielsen et al. 2007; Damineli et al. 2008a). Both of these facts indicate that the side of the system facing us is more ionized than the far side of η_A's wind. Figures 3.7 and 3.8 show that this is true only if η_B, and hence apastron, is on the observer's side of the system for most of the binary orbit.

The S IMPLE X results appear to favor a formation scenario for the He I lines that is more-or-less consistent with that proposed by e.g. Nielsen et al. (2007), Damineli et al. (2008a), with some modifications. In the following, we consider the Case A simulation results, which most likely represent η_A's current mass loss rate (M13). The simulations clearly show that with apastron on the observer's side of the system, η_B ionizes portions of the WWIR and pre-shock η_A wind flowing toward the observer. Thus, for most of the orbit, the He I emission lines would form mostly in the blueshifted part of η_A's wind, consistent with the observations. The double, and sometimes multiple, peak profiles observed in He I emission are consistent with emission arising from spatially separated regions in the WWIR. The two ionized dense arms of post-shock η_A wind (Figures 3.7 and 3.8) are very likely the sources of these emission peaks. The broader general component of the He I emission likely arises in both the central η_A wind (due to ionization by η_A itself) and the larger ionization zone within the pre-shock η_A wind located near the WWIR apex.

The observed He I absorption is also blueshifted over η Car's entire spectroscopic cycle, but is relatively weak around apastron (Nielsen et al. 2007). Based on our modeling, this is consistent with the idea that the absorption arises in the ionized pre-shock primary

wind located near the WWIR apex, and the ionized portions of the WWIR (specifically, the dense post-shock η_A wind). The gas velocities in these two regions, which are approximately equal to the terminal velocity of η_A's wind, are consistent with the observed velocity of the P Cygni absorption in the He I lines (~ -300 to $-600 \, \mathrm{km \, s^{-1}}$). Which region dominates the He I absorption in line-of-sight is uncertain at this point, but the much denser (by at least an order of magnitude) WWIR likely dominates, especially if one considers sight lines that are nearly parallel to and intersecting the WWIR surface (which is likely the case since the binary is inclined by $\sim 45°$ away from the observer; see Madura et al. 2012, 2013). Thus, contrary to the assumption by Nielsen et al. (2007), the observed He I absorption is very likely dominated by material in the post-shock η_A wind, rather than in the pre-shock η_A wind. This is the scenario favored by Damineli et al. (2008a).

Another important difference between our simulation results and simpler models for η Car's He ionization zones (e.g. Martin et al. 2006; Humphreys, Davidson & Koppelman 2008; Mehner et al. 2012) is the detailed ionization structure of the gas in the pre-shock η_A wind that borders the WWIR. This is due mainly to the complex structure of the WWIR, which in toy models is too simplistic. The WWIR consists of a region of hot, compressed (by roughly a factor of 4) post-shock η_B wind separated by a CD from a thin region of very-high-density, colder ($T \sim 10^4$ K) post-shock primary wind. The dense, turbulent post-shock η_A wind absorbs most of η_B's He^{0+}-ionizing photons and greatly affects the ionization structure of η_A's pre-shock wind. Detailed examination of Figures 3.7 and 3.8 shows that with the exception of a $r \sim 75$–80 au region about the WWIR apex, the He$^+$ ionization front due to η_B penetrates only approximately half way into the post-shock η_A wind region. Only in the region near the WWIR apex does η_B singly-ionize He in η_A's pre-shock wind. At larger distances from η_A along the walls of the WWIR, He remains neutral in the pre-shock η_A wind. Thus, simple models like that shown in Figure 12 of Humphreys, Davidson & Koppelman 2008 and Figure 5a of Mehner et al. 2012 are only partially correct[2], and very dependent upon scale-lenght (Martin et al. 2006; Humphreys, Davidson & Koppelman 2008 and Mehner et al. 2012 show only a small region near the stars at apastron). The He$^+$ region around the WWIR apex is also thinner and more geometrically similar to the WWIR in such models than we find in our simulations. The He$^+$ region in the pre-shock η_A wind in our simulations is more similar to Figure 5b of Mehner et al. (2012), but with the wings of He$^+$ not bending back farther than the location of η_A.

Mehner et al. (2012) used their Figure 5 to illustrate their interpretation for why the strength of the He I P Cygni absorption observed in η Car has been gradually increasing since 1998, with a sudden absorption increase after the 2009 periastron event (Groh & Damineli 2004; Mehner et al. 2010, 2012). Mehner et al. (2012) attribute the observed increase in absorption, and other changes, to a gradual decrease of $\dot{M}_{\eta_A}$ by a factor of ~ 2–3 between 1999 and 2010. They suggest that a drop in $\dot{M}_{\eta_A}$ would change the He ionization structure of η_A's pre-shock wind, as depicted in their Figure 5. Mehner et al.

---

[2]They appear to neglect the post-shock η_A wind region and CD.

(2012) suggest that the enlarging of the He$^+$ zone in η_A's pre-shock wind with decreasing $\dot{M}_{\eta_A}$ would lead to more He I absorption in line-of-sight.

Our SimpleX simulations show that, in the orbital plane, the behaviour of the He$^+$ ionization zone in η_A's pre-shock wind with decreasing $\dot{M}_{\eta_A}$, as suggested by Mehner et al. (2012), is partially correct. We find that a decrease in $\dot{M}_{\eta_A}$ does enlarge the He$^+$ zone in the pre-shock η_A wind. Moving from Case A to Case B, two large 'wings' of He$^+$ develop in the pre-shock η_A wind that bend backward around η_A. The post-shock η_A wind also becomes more ionized and contains more He$^+$ out to larger radii from η_A. However, the He$^+$ wings in the pre-shock η_A wind do not continuously border the WWIR at all radii in Case B. Near the outer edges of the simulation in the orbital plane, there are clear gaps between the pre-shock η_AHe$^+$ zone and the WWIR. In these small regions, He remains neutral. Moreover, changes to the He ionization structure with decreasing $\dot{M}_{\eta_A}$ are confined mostly to the orbital plane when moving from Case A to Case B. The Case B simulation shows that the He$^+$ ionization zone in the *xz* plane is much smaller and remains concentrated near the WWIR apex, with no large He$^+$ wings extending back behind η_A. Decreasing $\dot{M}_{\eta_A}$ even more from Case B to Case C results in η_B ionizing He throughout the entire simulation domain. As discussed above and in M13, such a low $\dot{M}_{\eta_A}$ appears to be ruled out by numerous observations.

Based on these results, a small-to-moderate decrease (by no more than a factor of two) in $\dot{M}_{\eta_A}$, similar to the simple model suggested by Mehner et al. (2012), may help explain the observed increase in He I absorption. The key question is, how much He I emission and absorption does an ionization structure like that in Case B produce in line-of-sight? One might expect such a large change in the He$^+$ zone within η_A's pre-shock wind to result in a significant detectable change in the amounts of He I and He II emission. An increase in the amount of He$^+$ near the WWIR that is available to be ionized by very soft X-rays generated in the post-shock η_A gas as it radiatively cools should lead to increased He II $\lambda 4686$ emission throughout the binary orbit. Significant changes in the amount of He II $\lambda 4686$ emission during the broad part of η Car's orbit are not observed though, and the behaviour of the $\lambda 4686$ emission during recent spectroscopic events has been amazingly similar (Teodoro et al., in preparation). The lack of any major changes in the observed $\lambda 4686$ emission may imply that the amount of He$^+$ available in the pre-shock η_A wind at phases around apastron is not the key factor in determining the amount of $\lambda 4686$ emission. Rather, there may be a limited number of suitable photons generated in the WWIR that can produce $\lambda 4686$ emission in the available He$^+$ zone. As such, we suggest that the small amount of He II $\lambda 4686$ emission that is observed across η Car's entire orbital cycle originates in the He$^+$ zone in η_A's pre-shock wind that surrounds the apex of the WWIR, with the high-energy photons required for such emission originating in the nearby post-shock η_A wind.

However, the above scenario does not remedy the problem of why there has been no observed increase in the amount of He I emission. If the efficiency for creating He II $\lambda 4686$ emission around apastron is low, even though the amount of He$^+$ in η_A's wind is high, one would expect increased He I emission. A possible explanation for the lack of increased

emission is that the larger volume of ionized post-shock η_A wind is absorbing the He^{0+} photons generated in the larger pre-shock η_A He^+ zone. The details of how the amounts of emission and absorption in line-of-sight change as the WWIR opening angle increases (due to the decreased $\dot{M}_{\eta_A}$ and altered wind momentum ratio) are poorly understood at this time, and it is unclear whether any decrease in $\dot{M}_{\eta_A}$ was gradual (between $\sim$ 1998 and now) or sudden (during/after the 2009 periastron event). More detailed observations and theoretical models are needed to better understand the nature of η Car's He I lines.

Finally, based on our results, we speculate on a possible solution to an interesting problem concerning He^{0+} in η Car, namely, why there are no observed signatures of the broad He I emission lines in spectra obtained before 1944 if η Car is a binary containing a hot companion star (for details, see Humphreys, Davidson & Koppelman 2008). This is seen as a problem because it is assumed that η_B, if it exists and is a hot, massive star, should always ionize a significant volume of η_A's pre-shock stellar wind, leading to detectable He I emission. Such emission is only marginally present (at best) in early spectra obtained between η Car's second eruption in the 1890s and 1944. Humphreys, Davidson & Koppelman (2008) argue that, even if $\dot{M}_{\eta_A}$ was larger in the past, η_B would still have ionized η_A's pre-shock wind, which should lead to He I emission in the early spectra.

As shown in Section 3.3 and discussed above, the results of detailed 3D hydrodynamical and RT simulations can differ substantially from the expectations of a simple model like that in Figure 12 of Humphreys, Davidson & Koppelman (2008). Our Case A simulations show that η_B's He^{0+}-ionizing photons only moderately penetrate the dense post-shock η_A wind at radii $\gtrsim$ 75 au from the star, and that only the pre-shock wind in the inner $\sim$ 75 au around the WWIR apex is He^+. We also see from our Case B and Case C results that a factor of 2–4 change in $\dot{M}_{\eta_A}$ can lead to major changes in the ionization structure of He in η_A's pre-shock wind. *Therefore, we suggest that the reason broad He I lines were not observed in spectra of η Car before 1944 is because $\dot{M}_{\eta_A}$ was larger then (by at least a factor of 2–4, or more) than it is now.*

While SIMPLEX results using 3D SPH simulations that employ a higher $\dot{M}_{\eta_A}$ are needed to test this hypothesis, we can speculate what the resulting He-ionization structure would look like in such a situation where $\dot{M}_{\eta_A}$ is roughly a factor of two or more larger than its present value. Given the results in Figures 3.7 and 3.8, the post-shock η_A wind was probably so dense it absorbed nearly all incoming He^{0+}-ionizing photons from η_B, preventing ionization of the He^{0+} in η_A's pre-shock wind. There was also probably much less He^+ in the post-shock η_A wind since any such He^+ that formed there would likely quickly recombine due to the extremely high densities in that region. There would moreover be little-to-no intrinsic He I emission from η_A itself, since the inner He^+ zone in its pre-shock wind would extend to $r < 2.5$ au^3 from the star. Because the wind momentum ratio would be dominated by η_A's much denser wind, the opening angle of the WWIR would be much smaller, bringing the two arms of hot, post-shock η_B wind closer together. Conceivably, the two arms could be so close they practically overlap, in which

---

[3]The exact value requires a specific assumed value of $\dot{M}_{\eta_A}$ and detailed spectroscopic modeling with e.g. CMFGEN.

case the wind of η_B would be dominated by collisionally-ionized He^{2+}, with perhaps only a very narrow region of He^+ extending behind η_B (caused by photoionization of the remaining receding pre-shock wind). With practically no He^+ present in the inner η Car system, there would be no, or only marginal, He I emission detectable, thus explaining the early spectral observations.

An enhanced $\dot{M}_{\eta_A}$ between the 1890s and 1944 is quite possible, and even likely, since η Car had just experienced its second eruption, wherein it ejected $\sim 0.1\ M_\odot$ and formed the 'Little Homunculus' (Ishibashi et al. 2003; Smith 2005). The dense, slow-moving near-equatorial circumstellar ejecta known as the Weigelt blobs (Weigelt & Ebersberger 1986) were also ejected around this time. It is therefore not unreasonable to suggest that the LBV primary had a larger mass loss rate following these events, which slowly decreased to a more stable and 'normal' value by ~ 1944. During this period of higher $\dot{M}_{\eta_A}$, the ionizing flux from η_B was probably more confined and could not penetrate the denser WWIR, leading to the absence of any significant He I emission.

3.5   Summary and Conclusions

We investigated the effects of the hot secondary star's ionizing flux on η Car's inner winds and WWIR, focusing on the ionization structure of helium during the spectroscopic high state (i.e. orbital phases around apastron). We used SimpleX to post-process 3D SPH simulation output of the innermost region of the η Car system. Compared to our previous work, we implemented several changes and improvements in the RT simulations. Assigning to the SimpleX cells the SPH number density, instead of a Voronoi cell-volume approach, results in density distributions in SimpleX that are less affected by local differences in the SPH particle distribution. Sampling the η_B black body spectrum with three frequency bins and the use of DCT also lead to more physically realistic results, and hence more precise ionization fractions and front locations for H and He. Below we summarize our most important results.

1. The inclusion of the He^+ ionization volumes around the primary star η_A does not produce relevant differences in the final ionization results for simulations with high $\dot{M}_{\eta_A}$ (Cases A and B). The exception is Case C, wherein $\dot{M}_{\eta_A}$ is so low η_A fully ionizes H everywhere, and singly-ionizes He out to a radius of ~ 120 au. η_B is thus able to completely singly-ionize He throughout the entire computation domain in Case C. We are therefore able to rule out Case C as a possible current value for $\dot{M}_{\eta_A}$.

2. The SimpleX results show that η_B's He^{0+}-ionizing photons are able to penetrate the WWIR and reach the unperturbed η_A wind to varying degrees, depending on the value of $\dot{M}_{\eta_A}$. The geometry and extent of the He-ionization structures in the pre- and post-shock η_A wind depend strongly on $\dot{M}_{\eta_A}$.

3. He^{0+} is confined to the pre- and post-shock η_A wind for higher $\dot{M}_{\eta_A}$. The volume of He^+ in the pre- and post-shock η_A wind increases as $\dot{M}_{\eta_A}$ decreases. As expected, η_B

singly-ionizes He in its pre-shock wind. He^{2+} is produced, through collisional ionization, in the hot post-shock η_B wind.

4. The different extents of the He-ionization fronts into η_A's wind in both the orbital and *xz* planes might be caused by differences in the density and temperature state of the WWIR. Small holes or regions of lower density in the unstable post-shock η_A wind region may also allow He^{0+}-ionizing photons to penetrate the WWIR and ionize different portions of η_A's pre-shock wind.

5. The location of the He^+ region in our simulations provides further support for binary orientations in which apastron is on our side of the system (Damineli et al. 2008a; Okazaki et al. 2008; Parkin et al. 2009, 2011; Madura et al. 2012, 2013). The SimpleX results favor a formation scenario for the He I lines that is mostly consistent with that proposed by Damineli et al. (2008a).

6. Based on our results, a small-to-moderate decrease (by no more than a factor of two) in $\dot{M}_{\eta_A}$, similar to the simple model suggested by Mehner et al. (2012), may help explain the observed increase in He I absorption in η Car. However, numerous questions remain regarding this scenario, such as why such a decrease in $\dot{M}_{\eta_A}$ does not also lead to an increase in He I emission.

7. We suggest that the small amount of He II $\lambda 4686$ emission observed across η Car's entire orbital cycle originates in the He^+ zone in η_A's pre-shock wind that surrounds the apex of the WWIR, with the high-energy photons required for such emission originating in the nearby post-shock η_A wind.

8. Finally, we suggest that broad He I lines were not observed in spectra of η Car between its 1890s eruption and 1944 (Humphreys, Davidson & Koppelman 2008) because $\dot{M}_{\eta_A}$ was larger then (by at least a factor of 2–4, maybe more) than it is now. During this period of higher $\dot{M}_{\eta_A}$, the ionizing flux from η_B was probably more confined and could not penetrate the denser WWIR, leading to the absence of any significant He I emission.

Our investigation of the He-ionization structure of η Car's inner winds and WWIR helps constrain not only $\dot{M}_{\eta_A}$, but also the nature of the unseen companion η_B. We have shown that our results help explain, and are in qualitative agreement with, available observations of η Car's He I and He II lines. In future work, we plan to use these simulations to generate synthetic spectra for comparison to observational data in order to help place tighter constraints on the binary orientation, $\dot{M}_{\eta_A}$, and η_B's luminosity and temperature. Future improvements to SimpleX will allow us to use specific spectral energy distributions for η_B generated from detailed spectroscopic modeling with CMFGEN. These results, together with the ionization structure of He during the spectroscopic low state around periastron (investigated in a subsequent paper), will help us better understand the numerous observed spectral features that arise in the inner ~ 150 au of the system. Our numerical

work also sets the stage for future efforts to couple SIMPLEX with modern 3D SPH and grid-based hydrodynamics codes for even more physically-realistic 3D time-dependent radiation-hydrodynamics simulations of η Car and other colliding wind binaries.

3D radiative transfer simulations of η Carinae's inner colliding winds – II: Ionization structure of helium at periastron
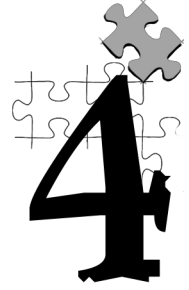
Spectral observations of the massive colliding wind binary Eta Carinae show phase-dependent variations, in intensity and velocity, of numerous helium absorption and emission lines throughout the entire 5.54-yr orbit. Approaching periastron, the 3D structure of the wind–wind interaction region (WWIR) gets highly distorted due to the eccentric ($e \sim 0.9$) orbit. The secondary star (η_B) at these phases is deep within the dense primary's wind photosphere. The combination of these effects are thought to be the cause of the particularly interesting features observed in the helium lines at periastron. We perform 3D radiative transfer simulations of η Car's interacting winds at periastron. We post-process with the SIMPLEX radiative transfer algorithm 3D smoothed particle hydrodynamics simulations of the inner 150 au of the system, for two different primary star mass-loss rates ($\dot{M}_{\eta_A}$). Using previous results from simulations at apastron as guide for the initial conditions, we compute 3D helium ionization maps. We find that, for higher $\dot{M}_{\eta_A}$, η_B He^{0+}-ionizing photons are not able to penetrate into the pre-shock primary wind. He^+ due to η_B is only present in a thin layer along the leading arm of the WWIR and in a small region close to the stars. Lowering $\dot{M}_{\eta_A}$ allows η_B's ionizing photons to reach the expanding unshocked secondary wind on the apastron side of the system, and create a low fraction He^+ in the pre-shock primary wind. With apastron on our side of the system, our results are qualitatively consistent with the observed variations in strength and radial velocity of the helium emission and absorption lines, which helps constrain the regions where these lines arise.

N. Clementel, T. I. Madura, C. J. H. Kruip and J.-P. Paardekooper
submitted to MNRAS

4.1   Introduction

The massive colliding wind binary Eta Carinae (η Car) is one of the most luminous stellar objects in the Galaxy ($L_{\text{Total}} \gtrsim 5 \times 10^6$ L$_\odot$). During its highly eccentric ($e \sim 0.9$), 5.54 yr orbit, the slow but high-density wind of the primary star η_{A} ($v_\infty \approx 420$ km s^{-1}, $\dot{M}_{\eta_{\text{A}}} \approx 8.5 \times 10^{-4}$ M$_\odot$ yr^{-1}; Hillier et al. 2001; Groh et al. 2012a) collides with the faster ($v_\infty \approx 3000$ km s^{-1}; Pittard & Corcoran 2002; Parkin et al. 2009), but less dense ($\dot{M}_{\eta_{\text{B}}} \approx 1.4 \times 10^{-5}$ M$_\odot$ yr^{-1}) wind of the secondary star η_{B}. Every periastron, orbital motion and the binary's large eccentricity highly distort the stellar winds and wind-wind interaction region (WWIR), causing η_{B} to become deeply embedded within the denser η_{A} wind (Okazaki et al. 2008; Parkin et al. 2011; Madura et al. 2012, 2013). At periastron, the dense distorted η_{A} wind and WWIR trap the ionizing radiation from η_{B} that is responsible for the formation of numerous high-ionization (ionization potential $\gtrsim 13.6$ eV) emission and absorption lines observed during the broad part of the orbit around apastron (Verner, Bruhweiler & Gull 2005; Damineli et al. 2008a; Gull et al. 2009, 2011; Madura & Groh 2012; Madura et al. 2012, 2013).

In a recent paper, Clementel et al. (2014b, hereafter Chapter 3) presented results from 3D radiative transfer (RT) simulations focusing on the ionization structure of helium, due to η_{B}'s ionizing radiation, in the inner ~ 155 au of the η Car system at an orbital phase of apastron. As summarized in Chapter 3, helium spectral features provide important information on both the geometry and physical properties of the η Car binary and the individual stars. While various helium features are present throughout the entire orbit, they show their most interesting behavior during periastron passage (Nielsen et al. 2007; Damineli et al. 2008a; Teodoro et al. 2012).

The goal of this paper is to extend the work of Chapter 3 and analyze the effects of η_{B}'s ionizing radiation during the spectroscopic low state at periastron. As in Chapter 3, we focus on the inner ~ 155 au of the η Car system and apply the SIMPLEX RT algorithm (Ritzerveld & Icke 2006; Ritzerveld 2007; Paardekooper, Kruip & Icke 2010; Kruip et al. 2010; Kruip 2011) to 3D smoothed particle hydrodynamics (SPH) simulations of η Car's colliding winds (Madura et al. 2013, hereafter M13) to compute 3D maps of the ionization structure of He. This work sets the stage for future efforts to compute synthetic He line profiles for direct comparison with available observations. The aim is to eventually constrain where and how the observed broad He emission and absorption lines form during the periastron event. We further aim to explain the temporal behavior of the broad He lines as the η Car system moves from apastron through periastron. Again, we note that we focus solely on interpreting the broad emission and absorption features of He that arise in the stellar winds and WWIRs, and not the narrower ($\lesssim 50$ km s^{-1}) features that form in the Weigelt blobs and other dense, slow-moving near-equatorial circumstellar ejecta (Weigelt & Ebersberger 1986; Damineli et al. 2008a).

The rest of this paper is organized as follows. In Section 4.2, we summarize our numerical approach. Section 4.3 describes the results. A discussion of the results and their implications is in Section 4.4. Section 4.5 summarizes our conclusions and outlines the

direction of future work.

4.2   Methods

The numerical approach in this paper, both for the SPH and RT simulations, are identical to those in Chapter 3. As in previous works, we use the SIMPLEX algorithm (Ritzerveld & Icke 2006; Ritzerveld 2007; Paardekooper, Kruip & Icke 2010; Kruip et al. 2010; Kruip 2011) to post-process 3D SPH simulation output (M13). For further details, we refer the reader to Chapters 2 and 3 and references therein. We also retain the naming convention used in M13, and Chapters 2 and 3 when referring to the SPH and SIMPLEX simulations in this paper, namely, Case A ($\dot{M}_{\eta_A} = 8.5 \times 10^{-4}$ $M_\odot \, yr^{-1}$), Case B ($\dot{M}_{\eta_A} = 4.8 \times 10^{-4}$ $M_\odot \, yr^{-1}$), and Case C ($\dot{M}_{\eta_A} = 2.4 \times 10^{-4}$ $M_\odot \, yr^{-1}$). In the following, we briefly describe only the key aspects and differences that are directly relevant to this work.

Due to the high eccentricity of the η Car system ($e \sim 0.9$), as the stars approach periastron, both the 3D structure and the dynamical evolution of the individual stellar winds and WWIR change drastically, compared to the majority of the orbital period. The stellar separation drops to ~ 1.5 au and orbital speeds increase greatly, becoming comparable to the wind speed of η_A (see Section 4.3 for details). The rapid orbital motion during periastron thus leads to major changes in the structure of the winds and WWIR on relatively short time-scales of the order of a few days (Okazaki et al. 2008; Parkin et al. 2011; Madura et al. 2012; M13).

To properly resolve this complex situation, we use two different SPH simulation domain sizes from M13. The larger domain is the same as the one used in Chapters 3 ($r = 10\,a = 155$ au), and allows for a direct comparison of the results in this paper with those at apastron in Chapters 3. The smaller domain simulations have a computational domain radius $r = 1.5\,a = 23$ au and eight times the number of SPH particles used in the $r = 10\,a$ simulations, leading to a roughly factor of two improvement in the overall spatial resolution compared to the $r = 10\,a$ simulations. The high-resolution simulations also focus only on phases around periastron ($\phi = 0.97$–1.03), with output written every $\Delta\phi \approx 8 \times 10^{-4}$, which is approximately every 1.6 days of the 2024-day orbit. These smaller, higher-resolution simulations ensure that we are adequately resolving the stellar winds and WWIR directly between the stars, as well as any possible WWIR 'collapse' that may affect the escape of η_B's ionizing radiation (M13). The higher resolution $r = 1.5\,a$ simulations are also useful for checking the accuracy of the $r = 10\,a$ results.

We consider the ionization of hydrogen and helium atoms by both collisional- and photoionization, and assume the same abundance by number of He relative to H as Hillier et al. (2001), $n_{He}/n_H = 0.2$. We employ a single photoionizing source located at the position of η_B. As in Chapters 3, we consider η_B to be an O5 giant with $T_{eff} \approx 40,000$ K, we assume a total ionizing flux for H and He of 3.58×10^{49} photons s^{-1} (Martins, Schaerer & Hillier 2005), and we use three bins to sample the stellar spectrum, which we approximate

with a black body. The width of each frequency bin is set by the ionization energy of each species. The first bin ranges from the ionization frequency of H^{0+} ($\nu_{H^{0+}} = 3.28 \times 10^{15}$ Hz) to that of He^{0+} ($\nu_{He^{0+}} = 5.93 \times 10^{15}$ Hz), the second from $\nu_{He^{0+}}$ to $\nu_{He^{+}}$ (1.31×10^{16} Hz), and the third from $\nu_{He^{+}}$ to a maximum frequency equal to ten times $\nu_{H^{0+}}$. We use an effective cross-section representation to determine the correct number of absorptions within each frequency bin. We set the black body temperature to the value that produces the correct ratio photons$_{H^{0+}}$/photons$_{He^{0+}}$ (in this case $T_{bb} = 49{,}000$ K), in accordance with the $q_{H^{0+}}/q_{He^{0+}}$ ratio in Martins, Schaerer & Hillier (2005). $q_{He^{+}}$ is effectively zero for η_B.

In figures displaying our SimpleX results for density and temperature, we visualize the average of the four vertices that compose each Delaunay cell. Unfortunately, this approach leads to cell values which are difficult to interpret if the vertex values differ by several orders of magnitude. In our simulations, this might occur for the fractions of He^{0+}, He^{+} and He^{2+}. In order to visualize results for these quantities in an understandable way that more truthfully represents the physics of our RT simulations, we adopt the visualization approach described in Section 3.2.2.5 of Chapters 3. In all figures showing ionization structure, we display the minimum vertex value for the fraction of He^{0+} and the maximum vertex value for the fraction of He^{2+}. For He^{+}, we show the maximum value whenever the temperature of the gas is lower then 10^5 K, and the minimum otherwise (for temperatures $> 10^5$ K, the fraction of He^{+}, due to collisional ionization, is $\approx 10^{-3}$ or lower). For the reasons discussed in section 2.3.1 of Chapters 3, we do not include plots of the ionization structure of H. We emphasize that the visualizations are merely to help guide the reader, and neither the physics nor the conclusions of our work depend on them (see Chapters 3 for details).

Using the method described in Section 3.2.3.1 of Chapters 3, we account for the inner He^{+} volume around η_A ($r \sim 3$ au for Case A, and ~ 7.5 au for Case B) based on 1D CMFGEN models of η Car by Hillier et al. (2001, 2006). We do not include the inner He^{2+} zone in η_A's wind in the $r = 10a$ simulations since it is of negligible size ($r < 1$ au), and because η_B produces essentially zero He^{+}-ionizing photons. Due to their smaller domain size, for added accuracy, the 23 au simulations do include the He^{2+} structure in η_A's innermost wind ($r \sim 0.7$ au for Case A, and ~ 0.8 au for Case B).

As discussed in Chapters 3, our results at apastron appear to rule out low values of $\dot{M}_{\eta_A}$, such as that in Case C. This is supported by the work of M13 and recent observations of η Car (T. Gull and M. Corcoran, private communication). Therefore, we focus in this paper on simulation Cases A and B, which more likely represent η_A's current mass loss rate. Moreover, little information would be obtained by including Case C since for such a low mass loss rate η_A already singly-ionizes He throughout the entire computational domain in the $r = 1.5a$ simulations, and nearly the entire domain (out to $r \approx 120$ au) in the $r = 10a$ simulations.

Finally, we note that we use a standard Cartesian coordinate system with the origin located at the system centre of mass and the orbital plane set in the xy plane, with the major axis along the x-axis. The stars orbit counterclockwise if viewed from along the $+z$-axis. In this system of reference, at periastron, η_A is to the right and η_B is to the left.

4.2.1   Initial ionization state of the gas

As in Chapters 3, we post-process the SPH snapshots. This approach works well for the η Car system at apastron, when the ionization state reaches an equilibrium value on a time-scale much shorter than the orbital time-scale. More importantly, at apastron the η_B wind cavity is an almost axisymmetric cone, allowing η_B's ionizing photons to completely ionize the low-density secondary wind. In other words, it is reasonable at apastron to assume that knowledge of the ionization structure of the preceding SPH snapshot is not required for accurate RT results.

In this paper, however, we deal with phases at periastron where, due to rapid orbital motion, the interacting wind structures evolve on a time-scale comparable to the time necessary for the RT simulations to reach a stable ionization state. Moreover, the η_B wind cavity at periastron is strongly asymmetrical and distorted. Regions that were ionized by η_B in an earlier snapshot may not be reachable by η_B's photons in the next snapshot. To tackle these issues, we use a slightly different approach than that in Chapters 3.

Using collisional ionization equilibrium, the results of Chapters 3, and estimates for the recombination time of He^+ as a function of gas density and temperature, we are able to better constrain the initial ionization state of the gas for use as an initial condition in our SIMPLEX simulations. We know that He^{0+} in the cooler ($T \approx 10^4$ K) unshocked gas in the η_B wind on the apastron side of the system is completely photoionized by η_B during most of the binary orbit around apastron Chapters 3. Observations with the *Hubble Space Telescope*/Space Telescope Imaging Spectrograph show that numerous high-ionization lines that require η_B's ionizing flux are present for most of the orbit and do not start to fade until phase $\phi \approx 0.984$ (approximately one month before periastron, Gull et al. 2009; M13). Therefore, we can safely assume that η_B is able to completely ionize He^{0+} throughout its unshocked wind at least until $\phi \approx 0.985$ (and at least for the length scales of interest here, $r \lesssim 155$ au from the stars). After $\phi \approx 0.985$, η_B becomes deeply embedded in the dense wind of η_A and the WWIR becomes so distorted by orbital motion that we can no longer assume that η_B can efficiently ionize He^{0+} in its cool unshocked wind. If the He in the low-density ($n \lesssim 10^6$) unshocked η_B gas is no longer photoionized by the star, then, at $T = 10^4$ K, He^+ should recombine on a time-scale $t_{rec} = 42.4$ days or longer. Thus, around periastron, for gas with $T \approx 10^4$ K and $n \approx 10^6$, the recombination time-scale for He^+ becomes about an order of magnitude larger than the orbital time-scale.

Any gas that recombines very slowly compared to the orbital time-scale around periastron poses a potential problem for the accuracy of our RT simulations, mainly because we are post-processing the SPH simulation output. The SPH output contains no information about the previous ionization state of the gas before we start our SIMPLEX simulations. However, any gas with a low enough recombination rate should remain ionized from one snapshot to next, even though η_B photons no longer reach that material[1]. Therefore, we should preserve the ionization state of low-recombination-rate gas in the initial condition of our RT simulations.

---

[1]Of course, this depends on how long it has been since the supply of ionizing photons has been cut off.

The time difference between phase 0.985 and periastron is ≈ 30 days. The recombination time for gas with $T \approx 10^4$ K and $n \approx 10^6$ is about two weeks longer than this. Lower-density cool gas will have even longer recombination times. If we assume that the η_B ionizing flux becomes trapped by η_A's dense wind and the WWIR at $\phi \approx 0.985$, then at periastron, any such low-recombination-rate gas that was initially photoionized by η_B at $\phi \approx 0.985$ should still be ionized.

Therefore, to mimic the fact that the low-density, cool η_B wind on the apastron side of the system should remain ionized at periastron, we set the He fractions in the η_B wind material with $n < 10^7$ and $T < 4 \times 10^4$ K to be $\sim 97\%$ He$^+$. This should generate an initial condition closer to the previous ionizations state of the photoionized η_B gas. For gas with $n < 10^7$ and $T < 4 \times 10^4$ K, the recombination time-scale is ≈ 4 days or longer. The use of collisional ionization equilibrium as an initial condition for the remaining gas remains a valid approximation even around periastron, since for the pre- and post-shock η_A wind, the high densities allow the gas to recombine almost instantaneously. Hot ($T > 4 \times 10^4$ K) gas in the post-shock η_B wind will be collisionally ionized to He$^+$ or higher.

Due to the shorter dynamical time-scales around periastron, which alter the gas distribution from snapshot to snapshot, we must also run SIMPLEX for a much shorter simulation time, compared to that used at apastron in Chapters 3. In our simulation testing we find that, setting the initial condition of the gas as described above, in Case A, the ionization state reaches an equilibrium value in less than one day. In Case B, the gas reaches ionization equilibrium in ~ 2–3 days. Since significant changes to the gas density and temperature distributions around periastron also occur on a time-scale of ~ 2–3 days, we use a total RT simulation time of 2.5 days and a simulation time-step of ~ 5 minutes in order to achieve an accurate RT calculation of the ionization volumes and fractions. At these time-scales, the gas distribution, even around periastron, can be assumed to be roughly constant.

4.3 Results

To help the reader better understand the RT results, we first briefly describe the density and temperature structure in the *xy*, *xz*, and *yz* planes. For more details on the hydrodynamical simulation results, see M13. Figures 4.1 and 4.2 show the number density (top row) and temperature (bottom row) for the 155 au and 23 au Case A simulations, respectively (the green circles in Figure 4.1 mark the domain size of the 23 au simulations). As described in M13, approaching periastron, the orbital speed of η_A relative to η_B increases to a value of ≈ 360 km s^{-1}, close to η_A's wind speed (420 km s^{-1}), thus highly distorting the WWIR. The small stellar separation at periastron (~ 1.5 au) also prevents η_B's wind from reaching its terminal speed before colliding with η_A's wind. Combined with the effects of radiative inhibition by η_A (M13), this leads to a significant slowing of η_B's pre-shock wind, which alters the wind momentum ratio at the WWIR. This decreases the WWIR opening angle and moves the apex of the WWIR closer to η_B. This behaviour
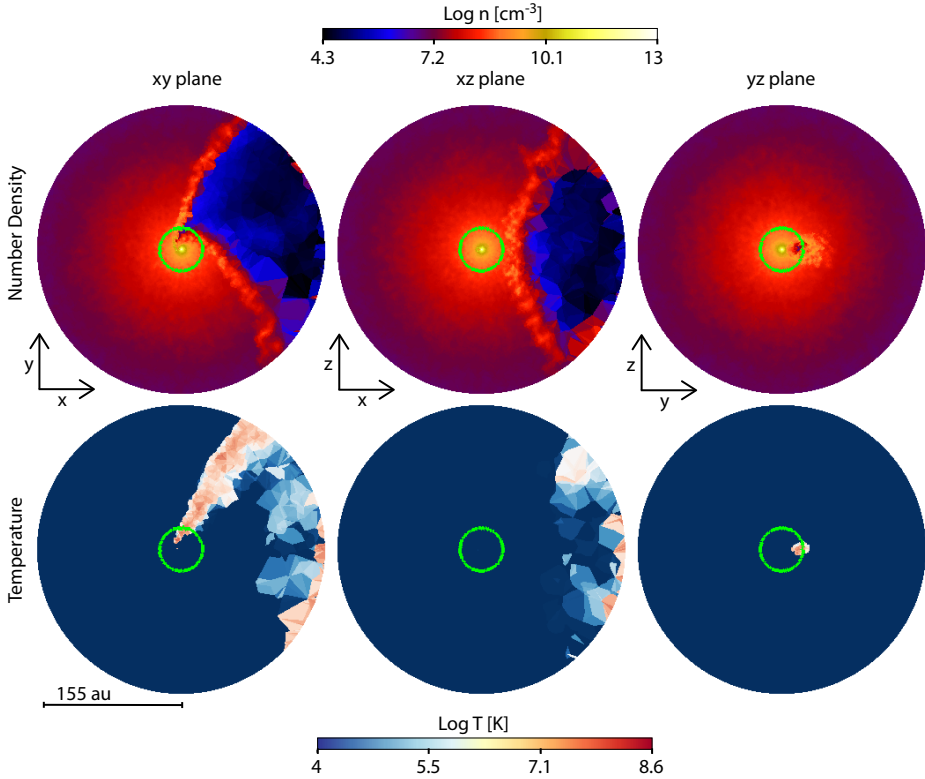
Figure 4.1 – Slices in the *xy* (left-hand column), *xz* (middle column) and *yz* (right-hand column) planes through the larger (10*a*) 3D simulation volume for the Case A simulation at periastron. Top row shows the number density (log scale, cgs units), bottom row shows the temperature (log scale, K). The length scale is shown under the bottom left-hand panel. In the first column (i.e. the orbital plane) η_A is to the right and η_B is to the left. The green circle marks the boundary of the smaller domain simulations (see Figure 4.2).

occurs in the Case B simulations in Figures 4.3 and 4.4 as well, although lowering $\dot{M}_{\eta_A}$ further increases the WWIR opening angle and moves the WWIR apex even closer to η_A.

The above effects create a high asymmetry between the trailing and leading arms of the WWIR at periastron, as η_B becomes deeply embedded in η_A's dense inner wind. The only direction η_B can effectively drive its wind is away from η_A (top left panel of Figures 4.2 and 4.4). This has a strong impact on the location of the shock-heated gas. As shown in the bottom left panel of Figures 4.2 and 4.4, the post-shock secondary wind is heated to temperatures higher than 10^6 K only where the η_B wind collides with the highly distorted leading arm of the WWIR (in red). The trailing wind of η_B is unable to collide with η_A's downstream wind, and so there is no hot shocked gas there. This effect is also visible in the bottom left panel of Figures 4.1 and 4.3. However, some residual hot gas remains at
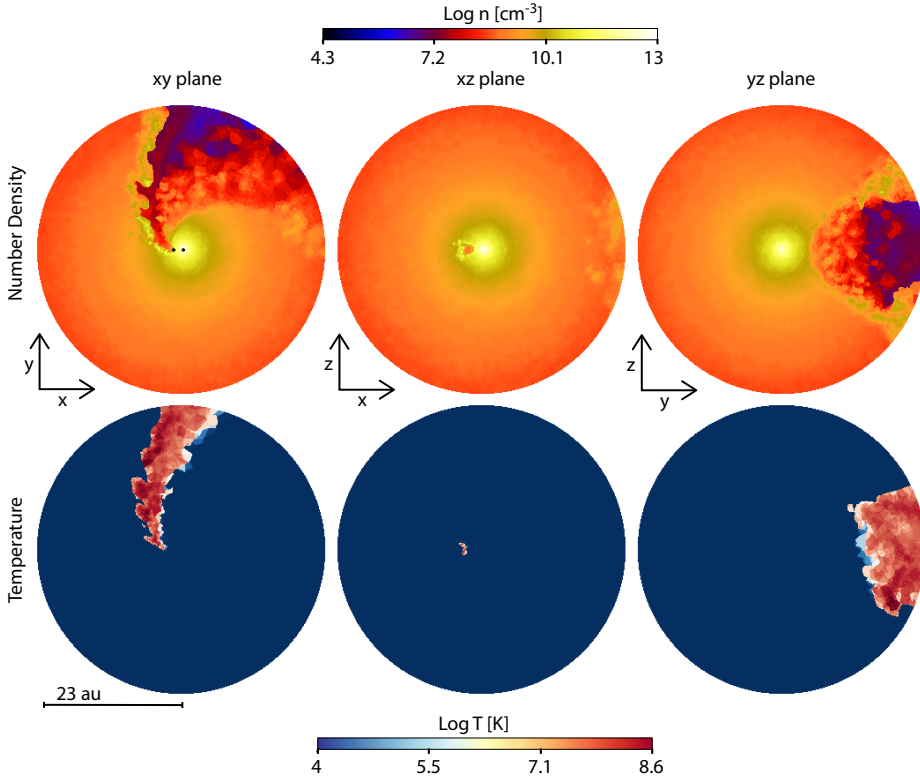
Figure 4.2 – Same as Figure 4.1, but for the smaller (i.e. $1.5\,a$) simulation domain. The black dots in the center of the top left-hand panel mark the position of the stars.

the outermost right edge of the simulation domain in the *xy* and *xz* plane slices. This is the expanding, adiabatically-cooling remnant of the trailing arm of the WWIR from just before periastron.

Looking at the *xz* plane (middle column of Figures 4.1–4.4), during periastron, $\eta_{\rm B}$ passes behind $\eta_{\rm A}$, allowing, for a short period, the primary wind to expand in the apastron $(+x)$ direction. During this time, the apex of the low-density cavity on the apastron side of the system fills with dense primary wind. The thickness and density of this inner primary wind region increases with $\dot{M}_{\eta_{\rm A}}$, since higher $\dot{M}_{\eta_{\rm A}}$ move the apex of the WWIR farther from $\eta_{\rm A}$, allowing the primary wind to fill a larger volume in the apastron direction. Slices in the *xz* plane also sample mostly cold (10^4 K) gas from both winds, although the $\eta_{\rm B}$ wind cavity in the Case B simulations contains warmer material due to the larger WWIR opening angle and less oblique shocks (M13).

Slices in the *yz* plane (right-hand column of Figures 4.1–4.4) simply show that at periastron, the leading arm of the WWIR has passed through the *yz* plane. There are now clear differences in both the density and temperature along the *y* axis. The $-y$ side of the
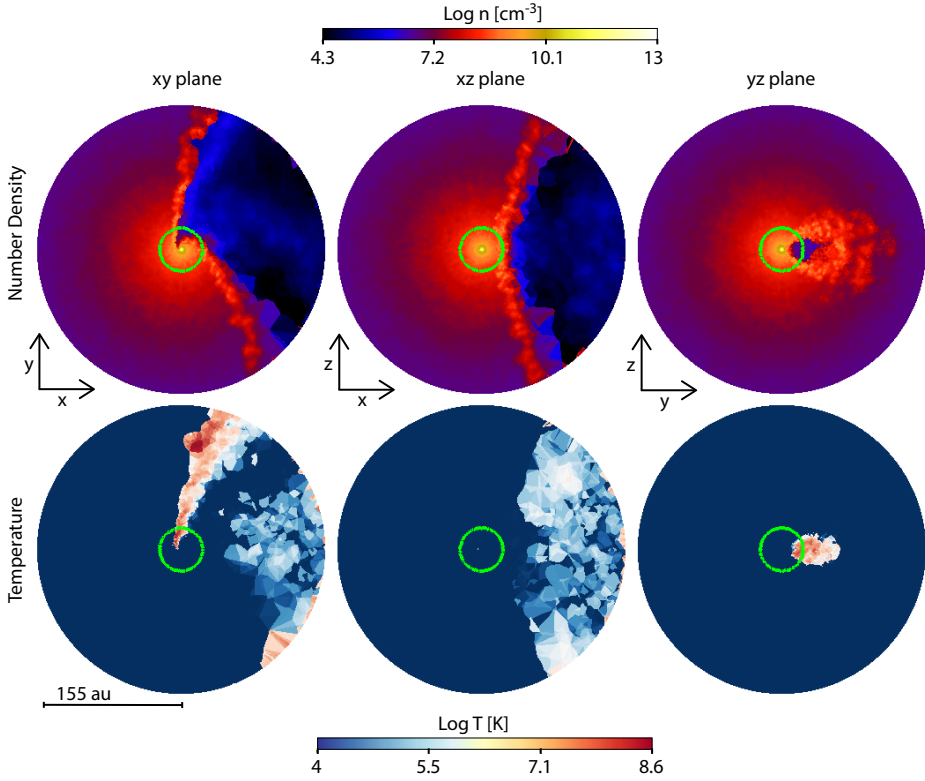
Figure 4.3 – Same as Figure 4.1, but for the Case B simulation.

system still consists of unshocked η_A wind, but to the $+y$ side there is a small cavity filled with hot, shocked η_B wind that is bordered by dense post-shock η_A wind. This cavity is larger in the Case B simulations due to that simulation's larger WWIR opening angle.

4.3.1   Overall He ionization structure and influence of $\dot{M}_{\eta_A}$

4.3.1.1   The orbital plane

Figures 4.5 and 4.6 present the He ionization structure in the orbital *xy* plane for Cases A and B, respectively. Columns illustrate, left to right, the fractions of He^{0+}, He^+ and He^{2+}. Rows display the 23 au domain without the inner ionization volume due to η_A (top), the same domain with the inner He^+ and He^{2+} ionization volumes (middle, filled yellow and blue circles in the left-most panel, respectively), and the larger (155 au) simulation domain with the inner He^+ ionization volume due to η_A included (bottom). The green contour highlights the boundary of the unperturbed pre-shock primary wind. Due to the complex situation at periastron, the green contour is meant more as a guide to
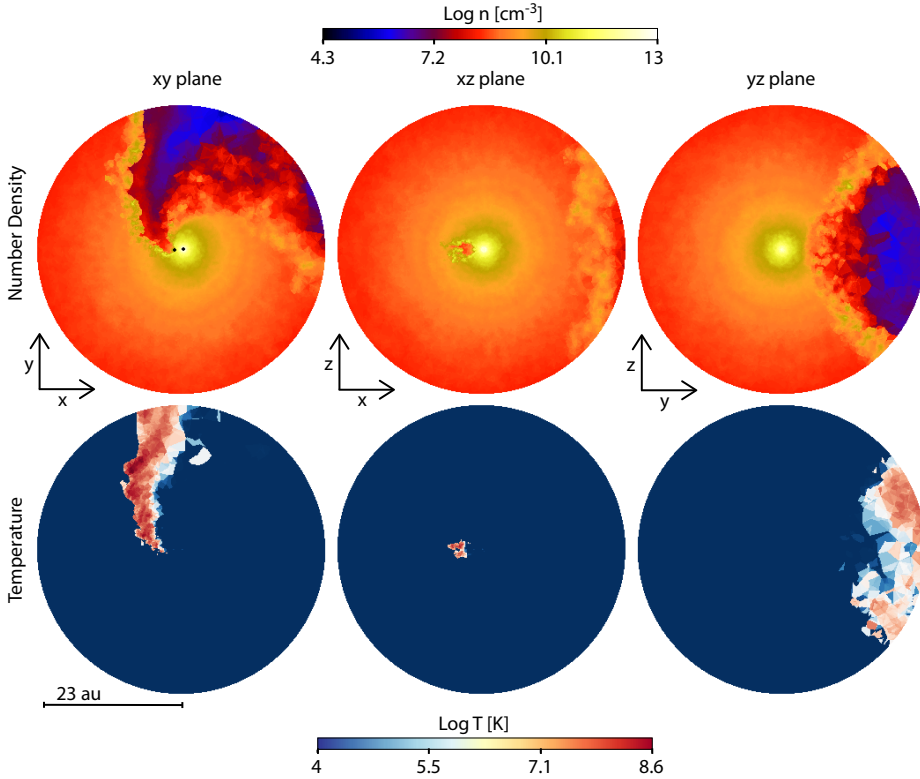
Figure 4.4 – Same as Figure 4.2, but for the Case B simulation.

better understand the results then a precise position for the pre-shock primary wind.

As discussed in Chapters 3, η_B should not have many He^+-ionizing photons and, therefore, He^{2+} is produced principally through collisional ionization. As expected, neglecting the inner He^{2+} region in η_A's wind, He^{2+} is only present in the hottest ($T \gtrsim 10^5$ K) regions of the system, i.e. the shock-heated gas in the leading arm of the WWIR, and the adiabatically-cooling hot gas in the remnant of the trailing arm (from before periastron passage).

Similar to the case at apastron (Chapters 3), η_B ionizing photons create different He^+ structures depending on the value of $\dot{M}_{\eta_A}$. In Case A, the He^{0+}-ionizing photons are only able to ionize a thin layer within the leading arm of the WWIR, and a rather small volume of the diffuse η_A wind that is expanding into the η_B wind cavity located near the remnant of the WWIR's trailing arm (first row of Figure 4.5). The dense primary wind expanding into the η_B wind cavity is able to stop η_B's He^{0+}-ionizing photons. The He^+ present in the cooler, unshocked η_B wind on the apastron side of the system is the previously photoionized gas that is slowly recombining. The inclusion of the inner He^+ and He^{2+} regions due to η_A have basically no effect on the larger-scale He ionization structures in
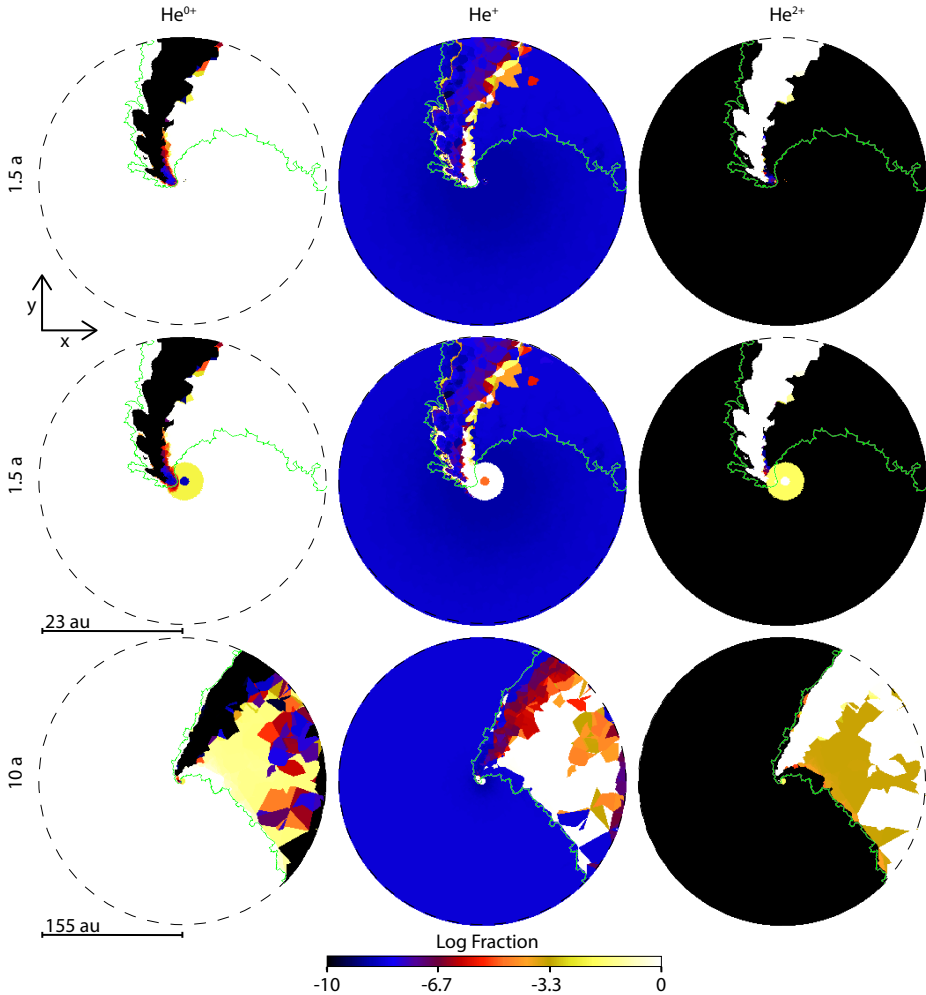
Figure 4.5 – Slices in the orbital plane through the 3D SIMPLEX simulation volume for the Case A. Column, from left to right show the computed fractions of He^{0+}, He^+ and He^{2+} (log scale). Rows show,from top to bottom, the smaller (23 au) simulation domain without the inner ionization volumes due to the primary, the smaller (23 au) simulation domain with the He^+ and He^{2+} inner ionization volumes due to the primary, the bigger (155 au) simulation domain with the He^+ ionization volume due to the primary. In this and Figure 4.6 the green line marks the edge of the pre-shock primary wind.

Case A (compare the top and middle rows of Figure 4.5). The only noticeable difference is that the He^{0+}-ionizing photons are able to penetrate through the leading arm of the WWIR and further ionize a very small area inside the inner 3 au η_A He^+ ionization volume (the red within the yellow circle, close to the center in the $-y$ direction in the first panel of the middle row). For Case A the dense outer primary wind, i.e. the area beyond the green contour, is almost entirely He^{0+}.
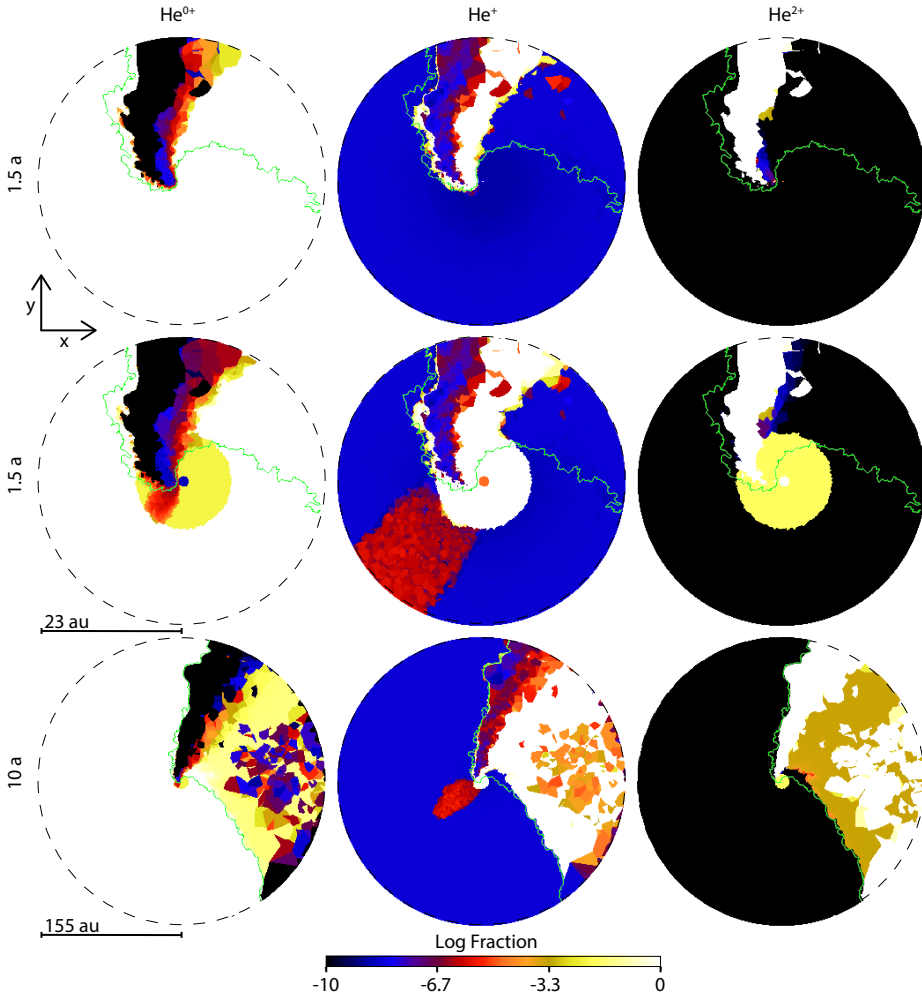
Figure 4.6 – Same as Figure 4.5 but for the Case B.

The larger WWIR opening angle in Case B, due to the lower $\dot{M}_{\eta_A}$, allows the He^{0+}-ionizing photons to escape the inner core and singly-ionize He in a portion of the the expanding primary and secondary winds on the apastron side of the system (right-hand side of the panels in Figure 4.6). Contrary to Case A, introducing the regions of ionized He in η_A's inner wind changes the extent of the ionization front in both the primary and secondary winds. The larger (7.5 au) He^+ zone in Case B allows ionizing photons to penetrate deeper into the receding primary wind, producing a region of He^+ (although the fraction of He^+ remains quite low, see the red region in the middle column in the middle and bottom rows of Figure 4.6). The He^+ on the apastron side of the system is a combination of ongoing photoionization and previously ionized gas which is slowly
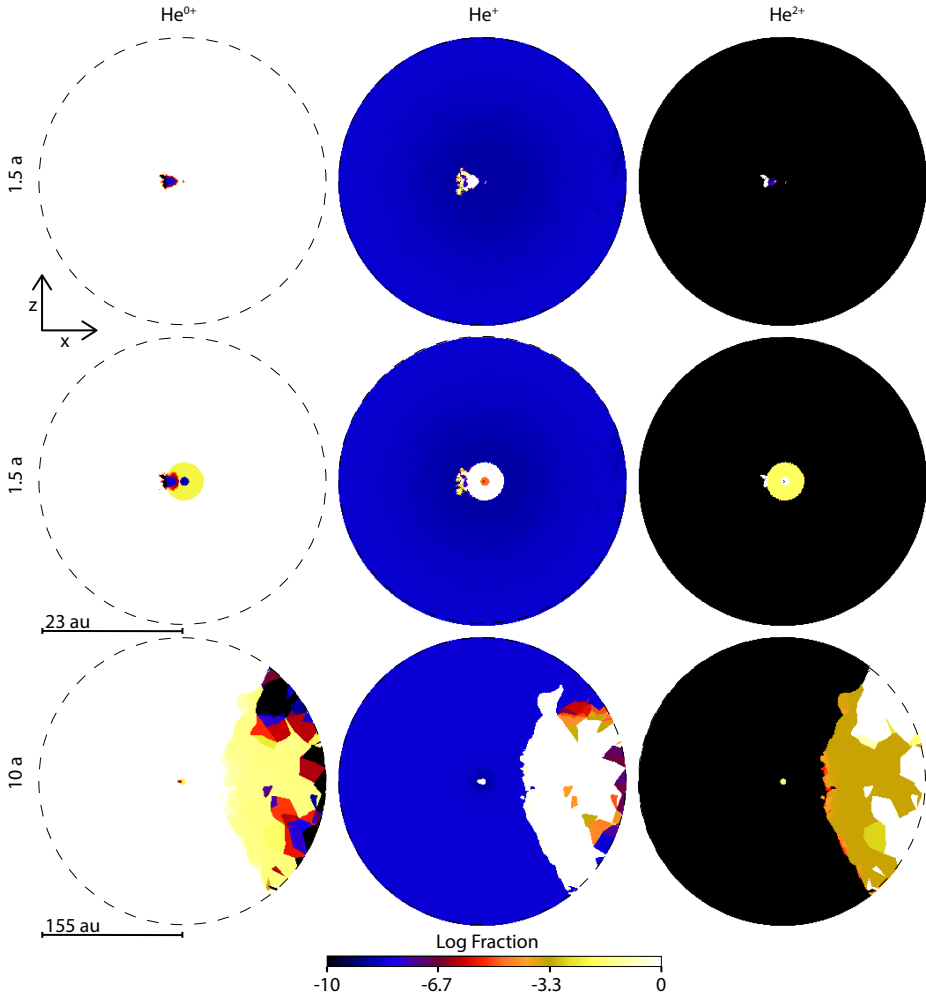
Figure 4.7 – Same as Figure 4.5 but for the *xz* plane.

recombining. However, as in Case A, the dense primary wind is mostly composed of He^{0+} and very effectively traps η_B's He^{0+}-ionizing photons (bottom row of Figure 4.6).

4.3.1.2 The *xz* and *yz* planes

Figures 4.7–4.10 show the ionization fractions in the *xz* and *yz* planes, illustrating the ionization structures below and above the orbital plane. Figures 4.7 and 4.9 further demonstrate that η_A's inner He-ionization zones have no influence on the larger-scale ionization structure in Case A. Again, only Case B shows any clear differences when the η_A He-ionization zones are included.
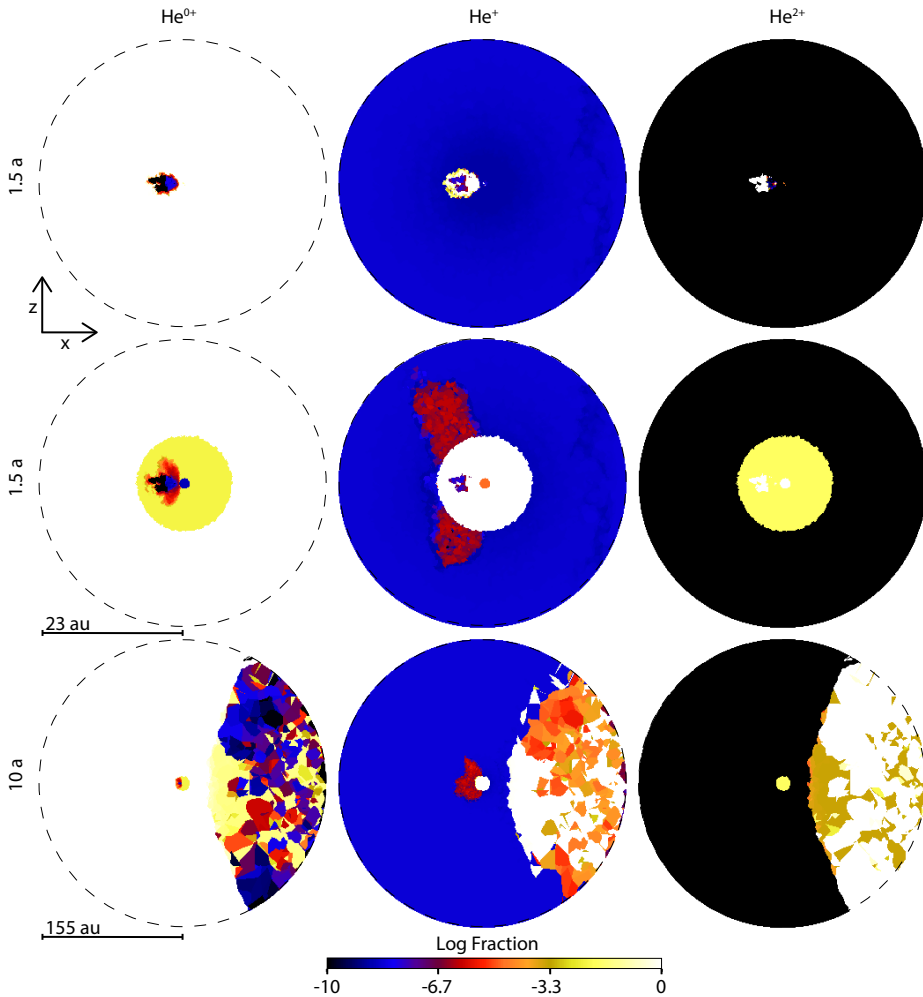
Figure 4.8 – Same as Figure 4.5 but for the Case B *xz* plane.

In the top two rows of Figures 4.7 and 4.8 for the 23 au domain simulations, we see the small central core of He ionization located near the apex of the WWIR in the direction of the leading arm ($-x$ direction). In Case A, there exists only a very small volume of shock-heated gas that is collisionally ionized to He^{2+}, which is bordered by a thin layer of He^+ that arises due to photoionization of the post-shock η_A wind by η_B. A similar situation occurs in Case B, although again the larger η_A He^+ zone allows some η_B He^{0+}-ionizing photons to penetrate into the dense primary wind above and below the orbital plane (areas in red in the central panel of Figure 4.8). However, as before, the fraction of He^+ in these areas is extremely low ($\lesssim 10^{-6}$), so He in the dense η_A wind remains effectively neutral. We see in the bottom row of Figures 4.7 and 4.8 that in both Cases A and B, the hot gas

He^{0+} He$^+$ He^{2+}

1.5 a

1.5 a

10 a

23 au

155 au

Log Fraction

-10 -6.7 -3.3 0
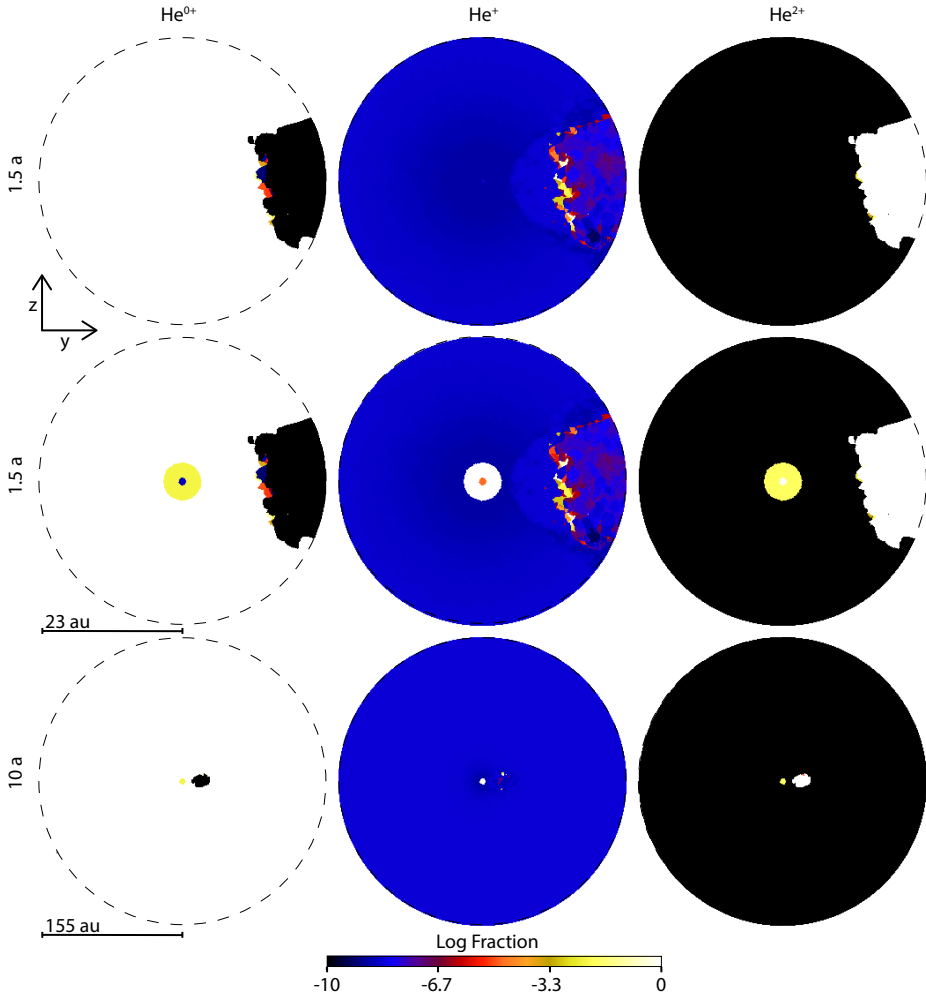
Figure 4.9 – Same as Figure 4.5 but for the *yz* plane.

in the remnant of the trailing arm of the WWIR is collisionally ionized to He^{2+}, while the colder unshocked η_B wind is composed of He$^+$ that has not yet recombined.

Figure 4.9 shows that in this plane, for Case A, only the very hot gas in the WWIR is collisionally ionized, to He^{2+}. The ionization structure in the *yz*-plane in Case B (Figure 4.10) is a bit more complex. As in Case A, very hot gas in the WWIR is collisionally ionized to He^{2+}, but closer to η_A there also exists a volume of He$^+$. Inspection of Figure 4.4 reveals that this is primary wind material expanding into the η_B wind cavity that is photoionized by η_B. The bottom row of Figure 4.10 furthermore shows that η_B is able to ionize He to He$^+$ in a layer of the dense post-shock η_A wind that borders the cavity of hot η_B wind (see the white oval line extending to the right in the bottom row middle
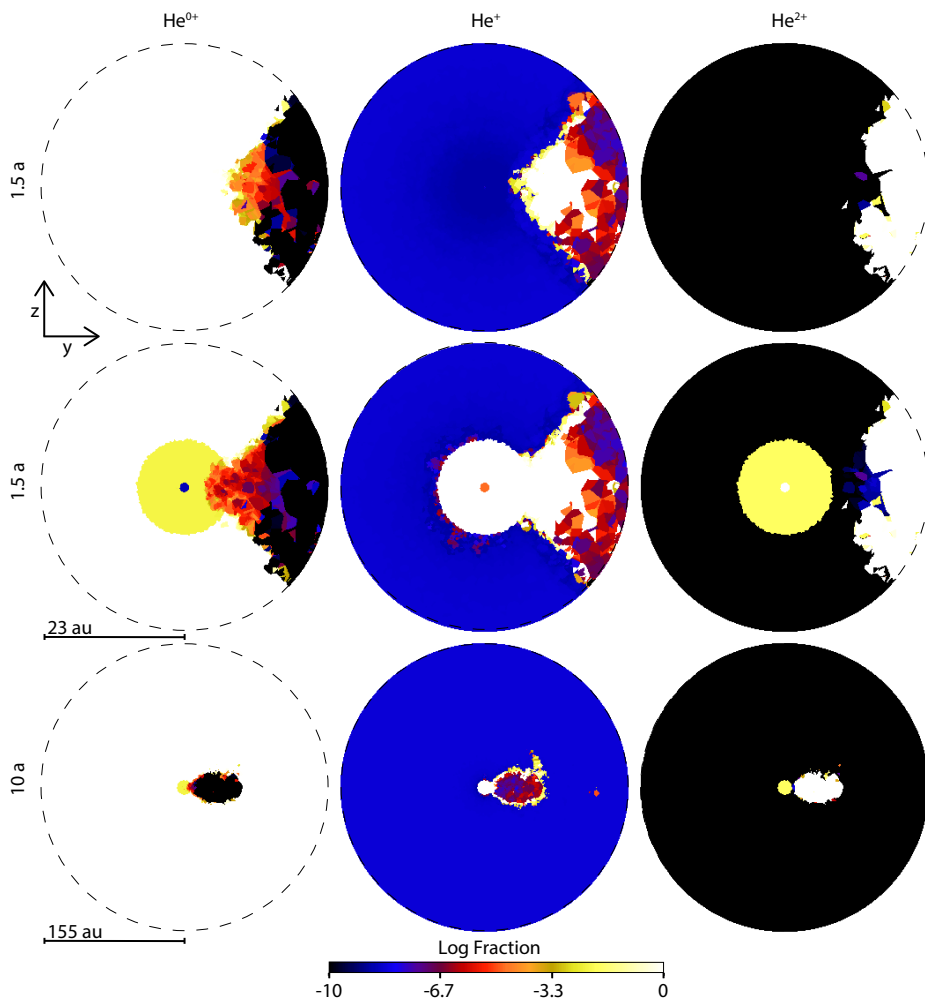
Figure 4.10 – Same as Figure 4.5 but for the Case B *yz* plane.

panel of Figure 4.10).

4.4   Discussion

From the discussions in Sections 4.2 and 4.3, it is evident that the interpretation of the results at periastron is much more difficult then at apastron, especially in terms of trying to understand how the results relate to observations of the various He line profiles (Nielsen et al. 2007; Damineli et al. 2008a). Nevertheless, we can use our results to try to better constrain the regions where the He emission and absorption features are generated. We focus on the Case A simulation results, since as discussed in M13, Chapters 3, and

above, they most likely better represent the current value of $\dot{M}_{\eta_A}$. We note that spectroscopic phase, defined by e.g. the disappearance of the narrow component of the He I lines (Damineli et al. 2008a, or alternatively, the minimum in the observed X-ray light curve, Corcoran et al. 2010), may differ from true orbital phase by up to one month.

Our results show that, at periastron, η_B is able to singly-ionize He in only a very thin layer of the post-shock η_A wind along the WWIR leading arm, and a very small region close to the stars. The denser η_A wind, expanding into the secondary wind cavity, is effectively able to stop the He^{0+}-ionizing photons. Therefore, the lower-density receding secondary wind on the apastron side and the adiabatically-cooling trailing arm of the WWIR from before periastron are shielded from ionizing photons from η_B. We do not expect this material to be neutral due to the long recombination time-scales for gas at these densities ($n < 10^7$) and temperatures ($\gtrsim 10^4$ K). The disappearance of the shock-heated region in the trailing arm of the WWIR, caused by the curvature of the WWIR, causes a strong asymmetry in the high temperature gas which is now mainly present in the WWIR leading arm. The He in this very hot region ($T > 10^6$ K) is collisionally doubly-ionized. With the exception of the inner He^+ and He^{2+} ionization regions due to η_A's ionizing flux, He in the extended primary wind is mostly neutral. This includes post-shock gas in the remnant of the trailing arm, and a significant portion of the extended leading arm, of the WWIR.

Observations show that the broad He I lines are generally blueshifted for most of the orbital period, both in emission and absorption. The P Cygni absorption starts increasing approximately three weeks before spectroscopic phase zero, reaching maximum absorption around phase zero, before decreasing to a complete disappearance ~ 20 days after phase zero (Nielsen et al. 2007; Damineli et al. 2008b). The radial velocity of the absorption reaches its maximum blueshifted value ($-610\,\mathrm{km\,s^{-1}}$) shortly before periastron, and then suddenly shifts during periastron down to $\sim -250\,\mathrm{km\,s^{-1}}$. This absorption must be produced by material between the observer and η_A, either in the WWIR or in the pre-shock wind of η_A.

Because the radial velocity variations seen in the He I $\lambda 7067$ absorption are reminiscent of those observed from a star in a highly eccentric orbit, Nielsen et al. (2007) assumed that the He I absorption is associated with the pre-shock wind of η_A, ionized by the far-UV flux from η_B. However, this assumption leads to an unusual, extreme system mass ratio of $q \sim 0.1$, with a mass for η_B of $210\,\mathrm{M_\odot}$ and a mass for η_A of $\sim 20\,\mathrm{M_\odot}$, in strong disagreement with the most commonly accepted values. In contrast, based on the maximum velocity of the absorption seen in the He I line and the requirements of high excitation flux and gas density, Damineli et al. (2008b) conclude that the only plausible locations for the formation of the broad He I absorptions are the walls of the WWIR. Our RT results favour this second scenario. At periastron, η_B is deep within the primary wind and its He^{0+}-ionizing photons are not able to reach the pre-shock η_A wind or penetrate beyond the dense layer of post-shock η_A wind. As shown in Figure 4.5 (central column, middle and bottom rows), He in the pre-shock primary wind is almost entirely neutral. The region of He^+ is confined to the centre of the system.

Modeling of η Car's X-ray light curve and observed broad, extended emission from numerous forbidden emission lines have helped constrain the orbital inclination (i), argument of periapsis (ω), and sky position angle (PA$_z$) of the η Car binary system (Okazaki et al. 2008; Parkin et al. 2009; Madura et al. 2012). It is generally agreed that the η Car binary is inclined away from the observer by roughly $\sim 45°$, with $\omega \approx 240°$–$285°$ and PA$_z \approx 302°$–$327°$, which places apastron on the observer's side of the system and implies that η_B orbits clockwise on the sky. With this orientation of the binary on the sky, at apastron, our line-of-sight (LOS) is more perpendicular to the apex of the WWIR surface. Based on the results in Chapters 3, we propose that the much denser WWIR (specifically, the compressed post-shock η_A wind) should dominate the P Cygni absorption at phases around apastron. However, because our LOS is more perpendicular to the WWIR around apastron, the column density of He$^+$ material between us and the continuum source η_A is relatively modest, resulting in a moderate amount of absorption. Moreover, because we are viewing the WWIR inclined away from us at roughly 45 degrees, material flowing toward us within the wall of post-shock η_A wind will have a maximum LOS velocity of $\sim 300 \, \mathrm{km\,s^{-1}}$, since the maximum true velocity of the gas within the compressed wall of post-shock η_A wind will be roughly equal to the terminal velocity of η_A's wind.

When approaching periastron, the trailing arm of the WWIR sweeps across our LOS. When this occurs, our LOS is parallel to and intersecting the WWIR. This results in a significantly increased column of He$^+$ between us and η_A, producing an increase in the amount of He I absorption. Because we are now looking directly down the WWIR, we are also seeing the fastest material in LOS, resulting not only in an increase in the amount of He I absorption, but also an increase in the blue-shifted velocity of this absorption. This scenario is in qualitative agreement with both the increase in the absorption and its shift toward more blue-shifted velocities of the observed He I P Cygni profiles going into periastron. Just after periastron, the strong He I $\lambda 7067$ absorption component rapidly vanishes. This is also consistent with our results, since we see that at periastron, η_B is no longer able to ionize the WWIR or the primary wind. With the observer on the apastron side of the system, the gas in LOS, further away from the central region, cannot be ionized by η_B, resulting in effectively no He$^+$ between us and the central η_A He$^+$ region, and thus a lack of He I absorption.

Our results in Chapters 3 imply that the He I emission seen around apastron should arise from a combination of the inner η_A He$^+$ zone, the pre-shock η_A wind close to the WWIR apex that is ionized by η_B, and the layer of post-shock η_A wind in the WWIR that is also ionized by η_B. The different regions, depending on the orbital phase, where the He I emission can form might help explain the observed multiple emission components observed in the line profiles (Nielsen et al. 2007). At periastron, as discussed in M13, the WWIR apex is inside η_A's He$^+$ region. The fact that η_B is able to ionize an extremely small region close to the center of the system during periastron means that the dominant source of He I emission at periastron is the inner η_A He$^+$ region. Based on our models, little to no He I emission is expected from the WWIR at and just after periastron.

One other relevant result is connected with the formation of the He II $\lambda 4686$ emission

line. Just before periastron, the He II λ4686 line intensity increases suddenly and then drops sharply to zero, after which it recovers to a second peak before declining back to zero (Steiner & Damineli 2004; Martin et al. 2006; Mehner et al. 2011; Teodoro et al. 2012). Based on the density and energy required for the formation of this line, the most plausible region in which it can form is close to the WWIR apex (Martin et al. 2006; Teodoro et al. 2012). Our results support the scenario proposed by M13 in which the He II λ4686 emission, observed at phases $\phi \sim 0.98$–1.3, is generated in the inner He$^+$ region of η_A's dense wind, with the necessary He$^+$-ionizing photons coming from the radiatively-cooling shocks in the WWIR. Our RT results show that, near periastron, η_B's ionizing flux is unable to produce a significant, extended region of He$^+$ in either the dense pre-shock η_A wind or the densest parts of the WWIR. Even though the unshocked η_B wind remains in the He$^+$ state during periastron, as discussed by e.g. Martin et al. (2006), Teodoro et al. (2012), the much lower-density η_B wind is incapable of adequately explaining the observed He II λ4686 emission. Thus, the only remaining region that can give rise to the observed He II λ4686 emission is the He$^+$ zone in η_A's dense inner wind.

The sharp drop in the He II λ4686 emission near periastron might be caused by a combination of two effects. First, we note that at periastron, the WWIR opening angle decreases considerably due to the much lower wind momentum ratio, caused by a large decrease in the pre-shock velocity of η_B's wind due to the decreased orbital separation and radiative inhibition effects (see Section 4.3 and M13). At periastron, η_B and the narrowed WWIR are also behind η_A and its optically-thick wind. Because the WWIR is much narrower, η_B and the WWIR are both 'eclipsed' by η_A and its dense wind at periastron. Second, if the WWIR 'collapses' at periastron due to the reduced η_B wind speed (see discussions in e.g. Corcoran et al. 2010, Parkin et al. 2011; M13), the radiatively-cooling WWIR shocks might disappear. If this occurs, the source of He$^+$-ionizing photons (i.e. the soft X-rays generated in the radiative shocks) necessary to produce the He II emission would also disappear. There would then obviously be no He II emission at periastron. We believe that a combination of a wind-eclipse by η_A and a 'collapse' of the WWIR is currently the best scenario for explaining the observed drop in He II λ4686 emission near periastron.

Finally, we briefly discuss the Case B simulation results, which show a similar behaviour to Case A, but with two major differences. The 1D CMFGEN models (Hillier et al. 2001, 2006) predict a radius for the inner He$^+$ region, due to η_A ionization, of ~ 7 au, more than a factor of two larger than in Case A. Even without this larger ionization region, η_B photons are able to ionize the denser primary wind, expanding into the η_B wind cavity, and reaching the expanding unshocked secondary wind on the apastron side of the system. Qualitatively, we expect these differences to produce variations, compared to Case A, both in the strength and velocity of the He emission and absorption lines. Moreover, the fact that η_B ionizing photons are still able at apastron to reach the periastron side of the system, have important implications on the phases at which these observed features occur. The increase in WWIR opening angle as $\dot{M}_{\eta_A}$ drops should also alter the timing of when specific He emission and absorption features are observed.

4.5   Summary and Conclusion

We presented the ionization structure of helium at periastron (i.e. the spectroscopic low state) in the inner regions of the η Car binary system due to the hot secondary star's ionizing flux. We created He ionization maps by post-processing 3D SPH simulations of the η Car system with SimpleX. Below we summarize our most important results and conclusions.

1. At periastron, the dense η_A wind expanding into the η_B wind cavity is able to stop η_B's He^{0+}-ionizing photons (in the Case A simulation). Helium is only singly-ionized by η_B in a very thin layer along the WWIR leading arm, and in a very small region close to the stars.

2. In Case B, the larger WWIR opening angle and lower $\dot{M}_{\eta_A}$ allow η_B to ionize a region of the lower-density unshocked η_B wind expanding in the apastron direction.

3. The inner He^+ volume due to η_A does not produce relevant differences in the final ionization structures due to η_B in simulation Case A. In Case B, the larger η_A He^+ radius allows the η_B ionizing photons to reach deeper into the dense η_A wind and create a lower ionization fraction in the pre-shock primary wind.

4. Collisional ionization creates He^{2+} in the hot shock-heated gas in the leading arm of the WWIR and in the adiabatically-cooling remnant of the trailing arm from just before periastron.

5. Our RT results support a binary orientation in which apastron is on the observer's side of the system, with the trailing arm of the WWIR sweeping across our LOS as periastron is approached.

6. The small He^+ region at the center of the system is the main region were He I emission can form during periastron. There is little to no He I absorption at periastron because η_B's ionizing flux is effectively trapped by η_A's dense wind, leading to a lack of dense He^+ gas between us and the continuum source η_A. This is consistent with the observed changes in strength and radial velocity of the He I P Cygni lines.

7. A lack of any significant He^+ in/near the WWIR at periastron, due to η_B, implies that the increased He II λ4686 emission that is observed around periastron must arise from the inner He^+ region in η_A's dense wind. Our results favour a scenario in which a combination of a wind-eclipse by η_A and a 'collapse' of the WWIR are responsible for the observed drop in He II λ4686 emission at periastron.

The He-ionization structures at periastron show a qualitative agreement with available observations of η Car's He lines. In the future, we plan to generate synthetic He line profiles for comparison to available observational data in order to place tighter constraints on the orbital, stellar, and wind parameters of η Car. These synthetic spectra, together

with those generated for the spectroscopic high state around apastron, will help us better understand the numerous observed spectral features generated in the inner ~ 150 au of the system. Our final aim is to use 3D time-dependent radiation-hydrodynamics simulations to more properly follow the ionization and recombination of the gas without post-processing. This is particularly important in the rapidly changing conditions and highly asymmetric situation at periastron.

3D printing meets computational astrophysics: deciphering the structure of η Carinae's inner colliding winds
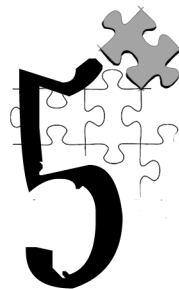
We present the first 3D prints of output from a supercomputer simulation of a complex astrophysical system, the colliding stellar winds in the massive ($\gtrsim$ 120 $M_\odot$), highly eccentric ($e \sim 0.9$) binary star system η Carinae. We demonstrate the methodology used to incorporate 3D interactive figures into a PDF journal publication and the benefits of using 3D visualization and 3D printing as tools to analyze data from multidimensional numerical simulations. Using a consumer-grade 3D printer (MakerBot Replicator 2X), we successfully printed 3D smoothed particle hydrodynamics (SPH) simulations of η Carinae's inner ($r \sim 110$ au) wind-wind collision interface at multiple orbital phases. The 3D prints and visualizations reveal important, previously unknown 'finger-like' structures at orbital phases shortly after periastron ($\phi \sim 1.045$) that protrude radially outward from the spiral wind-wind collision region. We speculate that these fingers are related to instabilities (e.g. thin-shell, Rayleigh-Taylor) that arise at the interface between the radiatively-cooled layer of dense post-shock primary-star wind and the fast (3000 $\mathrm{km\,s^{-1}}$), adiabatic post-shock companion-star wind. The success of our work and easy identification of previously unrecognized physical features highlight the important role 3D printing and interactive graphics can play in the visualization and understanding of complex 3D time-dependent numerical simulations of astrophysical phenomena.

T. I. Madura, N. Clementel, T. R. Gull, C. J. H. Kruip and J.-P. Paardekooper
submitted to MNRAS

5.1   Introduction

The supermassive binary star system Eta Carinae (η Car) is famous for the greatest non-terminal stellar explosion ever recorded (Davidson & Humphreys 1997). In the 1840s, η Car became the second brightest non-solar-system object in the sky and ejected between 10 and 40 $M_\odot$, forming the dusty bipolar "Homunculus" nebula (Smith et al. 2003; Gomez et al. 2010; Steffen et al. 2014). Amazingly, this did not destroy the star(s). Multi-epoch ground- and space-based observations obtained over the past two decades reveal that η Car is a colliding wind binary (CWB) with a current total mass $\gtrsim 120\ M_\odot$ (Hillier et al. 2001, 2006) and a highly eccentric ($e \sim 0.9$), 5.54-yr orbit (Damineli, Conti & Lopes 1997; Whitelock et al. 2004; Damineli et al. 2008b,a; Gull et al. 2009; Groh et al. 2010b; Corcoran et al. 2010; Teodoro et al. 2012).

Because they are so luminous ($L_{\text{Total}} \gtrsim 5 \times 10^6\ L_\odot$, Hillier et al. 2001, 2006), the stars in η Car have powerful radiation-driven stellar wind mass outflows. The Luminous Blue Variable (LBV) primary component, $η_A$, has one of *the* densest known stellar winds ($\dot{M}_{η_A} \approx 8.5 \times 10^{-4}\ M_\odot\,\text{yr}^{-1}$, $v_\infty \approx 420\ \text{km s}^{-1}$; Hillier et al. 2001; Groh et al. 2012a). The less-luminous companion star, $η_B$, has a much lower density, but faster, wind ($L_\star / L_\odot \approx 10^5\text{–}10^6$, $\dot{M}_{η_B} \approx 1.4 \times 10^{-5}\ M_\odot\,\text{yr}^{-1}$, $v_\infty \approx 3000\ \text{km s}^{-1}$; Pittard & Corcoran 2002; Parkin et al. 2009). These winds violently collide, producing strong X-ray emitting shocks (Pittard & Corcoran 2002; Corcoran et al. 2010; Hamaguchi et al. 2014) and a wind-wind interaction region (WWIR) that is thought to be the source of numerous forms of time-variable emission and absorption observed across a wide range of wavelengths (see e.g. Damineli et al. 2008a).

Proper numerical modelling of η Car's WWIR remains a challenge, mainly because it requires a full three-dimensional (3D), time-dependent treatment since orbital motion, especially during periastron, greatly affects the geometry and dynamics of the WWIR. Three-dimensional hydrodynamical simulations of η Car show that the complex time-varying WWIR has a major impact on the observed X-ray emission (Okazaki et al. 2008; Parkin et al. 2011; Russell 2013), the optical and ultraviolet (UV) light curves and spectra (Madura 2010; Madura & Groh 2012; Madura et al. 2012, 2013; Clementel et al. 2014a,b), and the interpretation of various line profiles and interferometric observables (Groh et al. 2010a,b, 2012a,b). While 3D hydrodynamical simulations have helped to increase substantially our understanding of the present-day η Car binary, we are limited by an inability to properly visualize the full 3D time-dependent geometry of the WWIR. However, this is crucial if we are to thoroughly understand how and where various forms of observed emission and absorption originate.

To date, nearly all published figures and animations of 3D simulations of η Car's colliding winds (and CWBs in general) consist of 2D slices through the origin of the typically-Cartesian 3D simulation domain, with color showing a scalar quantity such as density or temperature (see e.g. figures 1 and 2 of Madura et al. 2013, hereafter M13, or figures 8 and 9 of Parkin et al. 2011). In some cases, 2D slices showing physical quantities in the two coordinate planes perpendicular to the orbital plane are also provided (e.g.

appendix B of M13). With the exception of a few 3D isovolume renderings in Parkin et al. (2011), Madura & Groh (2012), Groh et al. (2012b), there has been no attempt to visualize and understand the full 3D structure of η Car's WWIR (or any real CWB's WWIR).

The predominance of 2D figures and animations in the literature is clearly driven by the need to display complex 3D data in a classic paper-journal format. In this sense, the problem of 3D visualization of complex astrophysical simulations and observational data is not limited to η Car or CWBs. However, there is no real reason, in this digital age, that researchers should be limited to 2D graphics when presenting their results in peer-reviewed publications. This is especially true since all major astrophysical journals are now published online. So-called 'augmented articles' (Vogt & Shingles 2013) are now possible, in which 3D interactive models, images, sounds, and videos can be included directly within an *Adobe Portable Document Format* (PDF) article. The inclusion of 3D interactive and animated models in the astrophysics literature, via methods such as those described in Barnes & Fluke (2008), are slowly becoming popular, and several astrophysical journals now fully support the inclusion of 3D interactive figures. Two very recent examples of such 3D interactive figures are figures 1 of Vogt et al. (2014), which presents a novel new way to classify galaxy emission lines via a 3D line ratio diagram, and figures 5 of Steffen et al. (2014), which presents a 3D interactive model of Eta Carinae's bipolar 'Homunculus' nebula that was constructed based on detailed spectral mapping observations obtained with the ESO Very Large Telescope/X-Shooter[1].

While the use of 3D interactive graphics will likely prove to be extremely helpful to astronomers in their quest for understanding and discovery, one should always try to keep an eye on emerging technologies that may further aid the astrophysical research community. One such technology that has been increasing in popularity across many different fields in recent years is additive manufacturing or '3D printing'. 3D printing has the potential to provide an entirely new method for researchers to visualize, understand, interpret, and communicate their science results.

The use of 3D printing in the astronomical community is still very much in its infancy, but several prominent examples have appeared within the past year. The first is a program aimed at transforming *Hubble Space Telescope* (*HST*) images into tactile 3D models using special software and 3D printers, with the goal of communicating the wonders of astronomy to the blind and visually-impaired (Christian et al. 2014). In the peer-reviewed literature there exists a 3D printable version of figures 1 from Vogt et al. (2014) (see their figures 15) and a 3D printable version of the Eta Carinae Homunculus nebula model by Steffen et al. (2014)[2]. Each of these is a unique illustration of how observational data can be used to develop a 3D printable model for increased understanding and communication of complex concepts. However, to date there have been no published attempts to use 3D visualization and printing techniques to aid in the understanding and communication of

---

[1]For other recent examples, see references in Vogt & Shingles (2013).

[2]See also http://www.nasa.gov/content/goddard/astronomers-bring-the-third-dimension-to-a-doomed-stars-outburst/

complicated multi-dimensional output from detailed numerical simulations of astrophysical phenomena.

In an effort to further demonstrate the benefits of using 3D visualization and 3D printing as tools to analyze output from numerical simulations, we present here the first 3D prints of output from a supercomputer simulation of a complex astrophysical system, the colliding stellar winds in the massive binary η Car. Using a consumer-grade 3D printer, we successfully print output from 3D time-dependent smoothed particle hydrodynamics (SPH) simulations of η Car's inner ($r \sim 110$ au) wind-wind collision interface at multiple orbital phases. The main goal is to gain an improved understanding of the full 3D structure of η Car's WWIR and how it changes with orbital phase. The 3D prints and visualizations reveal previously unrecognized 'finger-like' structures at orbital phases shortly after periastron that protrude radially outward from the spiral wind-wind collision region. The success of our work helps highlight the important role 3D printing can play in the visualization and understanding of complex 3D time-dependent simulations.

In the following section (5.2), we describe our methodology and numerical approach, including the SPH simulations, the 3D visualization of the SPH output, and the generation of 3D printable files. Section 5.3 presents the results in the form of standard 2D images, pictures, and 3D interactive graphics. A brief discussion of the results and their implications is in Section 5.4. Section 5.5 summarizes our conclusions and outlines the direction of future work.

5.2 Methods

5.2.1 The 3D SPH simulations

The hydrodynamical simulation snapshots we visualize correspond to specific phases (apastron, periastron, and 3 months after periastron) from the Case A ($\dot{M}_{\eta_A} \approx 8.5 \times 10^{-4}$ $M_\odot \, yr^{-1}$) and Case C ($\dot{M}_{\eta_A} \approx 2.4 \times 10^{-4} \, M_\odot \, yr^{-1}$) small-domain ($r = 10a = 155$ au) 3D SPH simulations of M13. We refer the reader to M13 and references therein for details on the SPH simulations and an extensive discussion of the results. The spherical computational domain size of radius $r = 155$ au is chosen in order to investigate at sufficiently high spatial resolution the structure of η Car's inner WWIRs, since the 'current' interaction between the two winds occurs at spatial scales comparable to the semi-major axis length $a \approx 15.4$ au. The three orbital phases selected are representative of when the WWIR is expected to have its simplest (apastron) and most complex (periastron and 3 months after periastron) geometry. The snapshot at apastron, when the stellar separation is largest and orbital speeds are lowest, provides a reference for the nearly-axisymmetric conical shape of the WWIR during most of the orbital cycle. The periastron snapshot defines the distorted geometry of the WWIR when the stellar separation is smallest and orbital speeds are greatest. The snapshot at an orbital phase 3 months after periastron ($\phi = 1.045$) corresponds to a time when the WWIR has a distinct Archimedean-spiral-like shape in the orbital plane due to the rapid orbital motion of the stars around periastron (Okazaki et al.

2008; Parkin et al. 2011; Madura et al. 2012, 2013). Simulations assuming two different mass loss rates for η_A (Cases A and C) are used to investigate how changes to the wind momentum ratio alter the WWIR opening angle, apex distance, 3D geometry, and dynamics.

We use a standard *xyz* Cartesian coordinate system and set the orbit in the *xy* plane, with the origin at the system centre of mass and the major axis along the *x*-axis. The stars orbit counter-clockwise when viewed from along the $+z$-axis. By convention, periastron is defined as $t = 0$ ($\phi = t/2024 = 0$). Simulations are started at apastron and run for multiple consecutive orbits.

5.2.2 Grid construction and density distribution

SPH is a mesh-free method for solving the equations of fluid dynamics (Monaghan 2005) that is widely used in the astrophysical community. However, visualizing SPH data is far from straightforward since the data are highly adaptive and unstructured, defined on a set of points that follow the motion of the fluid. Simple interpolation to a uniform structured grid is often not an option since the grids are so immense in size they cannot be handled efficiently, or significant interpolation errors are introduced in areas of high particle density (Linsen et al. 2011). Due to these complications, several programs have been developed specifically for the visualization of SPH data. A popular, freely-available tool that allows for visualization of slices through the simulation volume, direct volume rendering, and particle rendering is SPLASH (Price 2007). Unfortunately, SPLASH does not currently allow 3D isosurface extraction, which is required if we want to visualize η Car's stellar winds and WWIR as solid 3D surfaces. A more recent program designed for the interactive visual analysis of SPH data is SMOOTHVIZ (Linsen et al. 2011). SMOOTHVIZ allows isosurface extraction and direct volume rendering, but is currently limited to producing standard screenshots for use in research papers, as it uses OpenGL instead of graphics libraries such as PGPLOT (Molchanov et al. 2013).

Since our goal is to create 3D interactive figures and 3D printable files, we employ an alternative approach. We choose to generate a tetrahedral mesh from the SPH particle data in order to facilitate easier visualization with standard software such as VISIT[3] and PARAVIEW[4]. The generation of tetrahedral meshes from particle data has a long tradition, with the widely accepted results of Delaunay tetrahedrization dating to 1934 (Du & Wang 2006; Linsen et al. 2011). We therefore employ the same methodology as that in Chapters 2 and 3 to generate our unstructured 3D mesh. Using the SPH particles themselves as the generating nuclei, we tessellate space according to the Voronoi recipe: all points in a grid cell are closer to the nucleus of that cell than to any other nucleus. The Voronoi nuclei are then connected by a Delaunay triangulation.

We assign to the nucleus of each Voronoi cell the corresponding SPH quantities of particle mass, density, temperature, and velocity, computed using the standard SPH cubic

---

[3]https://wci.llnl.gov/simulation/computer-codes/visit
[4]http://www.paraview.org/

spline kernel (Monaghan 1992). This helps ensure that each scalar variable visualized on our mesh closely matches that of the original SPH simulations, since the kernel samples a larger number of particles over a larger volume, resulting in quantities that are less affected by local differences in the SPH particle distribution (Chapter 3). Comparison with a direct visualization of the SPH density using SPLASH (Price 2007) shows that this approach indeed matches well the density distribution of the original SPH simulations (see Figures 3.1 of Chapters 3). Figure 3.2 of Chapters 3 shows an example of the unstructured mesh and number density at apastron for one of our 3D SPH simulations of η Car.

5.2.3   Visualization

When visualizing scalar variables on our unstructured mesh, we would ideally like to render quantities that are centred on the original Voronoi cells that compose our 3D grid. Unfortunately, the Voronoi cells consist of a series of irregular n-sided polygons, which makes their visualization quite complex. Instead, it is much more straightforward to visualize the corresponding Delaunay triangulation. In 3D, the Delaunay cells are tetrahedra, which can be visualized using standard visualization tools. Since the Delaunay cells are tetrahedra, the quantity we visualize is the average of the four vertices that define the tetrahedron cell (i.e. the average of the four Voronoi nuclei). This approach works well for visualizing most physical quantities (e.g. temperature, density, velocity), and is suitable for our work. However, if neighbouring Voronoi nuclei have values which are significantly different (i.e. by several orders of magnitude), this 'volume-average' approach may lead to tetrahedral-cell values that are difficult to understand and interpret (see Chapters 3 for details).

Since we are most interested in the 3D structure of η Car's WWIR, we must find a way to visualize it separately from the individual stellar winds. It would also be useful to visualize in 3D the denser wind of η_A, which is modified greatly by the faster, lower-density wind from η_B. Doing the latter is straightforward since η_A and η_B have very different mass-loss rates ($\dot{M}_{\eta_A}/\dot{M}_{\eta_B} \approx 60$). Due to this difference in $\dot{M}$, our SPH simulations use different particle masses for each stellar wind. Based on the SPH particle mass, we are able to isolate the pre- and post-shock η_A winds and visualize them while keeping the entire pre- and post-shock η_B winds transparent (see e.g. the middle column of Figures 5.1–5.6).

For the WWIR, we choose to visualize the thin, dense post-shock η_A wind region that is located between the contact discontinuity (which separates the colliding wind shocks) and the pre-shock η_A wind. In order to isolate this specific region, we use its unique density and temperature distribution. Because the post-shock η_A wind cools radiatively rather than adiabatically (Parkin et al. 2011; M13), it remains at the floor temperature of $T = 10,000$ K set in the SPH simulations (M13). For the post-shock η_A wind, we therefore consider only regions with $T = 10,000$ K. This separates this part of the WWIR from the much hotter ($T > 10^6$ K) post-shock η_B gas.

Radiative cooling of the post-shock η_A gas also increases substantially its density, by at least an order of magnitude. Thus, there is a large difference in density between the

pre- and post-shock η_A winds. Since the SPH simulations use constant, spherical mass loss rates, the density dependence with radius from the stellar surface in each pre-shock stellar wind in the simulations is roughly given by $\rho_{\text{spherical}}(r) = \dot{M}/[4\pi r^2 v(r)]$, where $v(r) = v_\infty(1 - R_\star/r)^\beta$ is the standard 'beta-velocity law' ($\beta = 1$ for our simulations), with v_∞ the wind terminal velocity and $R_\star$ the stellar radius (M13). By defining a quantity $\delta \equiv \rho_{\text{SPH}}/\rho_{\text{spherical}}$, we can determine at each location the contrast in density between what is provided in the SPH simulations (ρ_{SPH}), and what the density at that location would be in an undisturbed spherical stellar wind. Within the pre-shock wind, $\delta \approx 1$, while in the post-shock wind, δ is greater than one, usually much greater. Therefore, we isolate the dense, post-shock η_A wind (from here on referred to generally as the WWIR) by computing δ for η_A's wind and selecting only those regions with $\delta > 2$ and $T = 10,000$ K (see e.g. the last column of Figures 5.1–5.6).

5.2.4 Generation of 3D interactive figures

So that readers can directly experiment with and see for themselves the full 3D structure of η Car's WWIR, we augment this article by incorporating directly into the PDF 3D interactive figures of both our SPH simulation results and the final 3D print models. We embed our 3D graphics directly into the PDF document in order to facilitate easy direct sharing of the 3D results. Nearly every figure in this paper has a 3D interactive counterpart that can be accessed using the freely-available software *Adobe Acrobat Reader v.8.0*[5] or above. Unfortunately, interactive 3D graphics in PDFs can currently only be viewed using *Adobe Reader*. Other PDF viewers will display only the standard 2D images shown in each figure.

The 3D interactive graphics allow the reader to fully rotate, zoom, and fly around each 3D model. This is a very efficient tool for revealing the structure of η Car's WWIR. In some cases, the 3D figures allow for the display (or not) of different components of the model (e.g. modified η_A wind versus WWIR only), providing the reader control over what he/she wants to see. Pre-defined 'views' to help guide the reader to specific orientations or features are also implemented, such as the orientation of the η Car binary on the sky as seen from Earth. We highly recommend after selecting and clicking on a specific 3D interactive figure, that the reader right-mouse-click the model and select from the available drop-down menu the option "View in Floating Window". This will open the interactive 3D model in a small (although adjustable) side window that permits continued reading of the text and simultaneous viewing of other figures with minimal inconvenience. Numerous other options are available in the toolbar associated with each 3D figure and we encourage the reader to fully explore these.

To create our interactive 3D graphics, and in an effort to encourage others to use such 3D figures in their work, we rely on robust freely-available visualization software. The most difficult part is converting a particular 3D visualization into the U3D format required for embedding within the PDF document (Barnes & Fluke 2008; Vogt & Shingles 2013).

---

[5] http://get.adobe.com/reader

We start by using either VISIT or ParaView to open and visualize our unstructured grid data. The choice of VISIT or PARAVIEW is optional, and any suitable scientific visualization program may be used, provided it outputs the created data to the required format. Once we create our visualization, we export the model as either an OBJ or X3D file, depending on what we want to show. Both formats preserve the detailed geometry of the 3D models, but we find that X3D is better at preserving the color table used in a detailed scientific visualizations, whereas OBJ is suitable for situations where only the overall geometry and a solid surface color/transparency is needed.

Once an OBJ or X3D file is created it can be read directly into the freely-available 3D mesh processing software MESHLAB[6], where the 3D model can be adjusted and corrections applied if needed, and then exported directly to the required U3D format. Another option is to read the OBJ or X3D file into the professional (but still free) 3D rendering and animation software BLENDER[7]. In BLENDER, textures and colors can be improved, added, subtracted, etc., and additional objects or meshes can be inserted (or removed). Numerous visualization possibilities exist with BLENDER, and we find that it is more stable and easier to use than MESHLAB. However, BLENDER does not support exporting directly to the U3D format. Nonetheless, one can create their final 3D model for visualization using BLENDER and export it as either OBJ or X3D. Then, one need only use MESHLAB to quickly and easily convert the OBJ/X3D file to the U3D format. In order to create the best possible visualizations, we employ BLENDER in this work, with a conversion to U3D using MESHLAB. The above process for creating a U3D file may seem cumbersome, but we find that is in fact quite straightforward. The interested reader that does not require free software can alternatively purchase programs such as PDF3DREPORTGEN[8] for the creation of U3Ds and 3D PDFs.

Once a U3D file is available, incorporating it into a PDF can be done using either standard commercial software or, as astronomers generally prefer, the free typesetting package LaTeX. The `movie15` and `media9` LaTeX style files fully support the embedding of 3D annotations in PDF documents. Using and calling the `movie15` and `media9` packages is incredibly straightforward and requires almost no more effort than inserting a standard 2D figure. For this paper, we use the `movie15` package.

5.2.5   Generation of 3D print files and printing the results

Unfortunately, having a 3D model and mesh, even one that looks very nice on a computer screen, does not necessarily mean that it is suitable for 3D printing. Beside the requirement of converting the 3D model to the appropriate file format for use with a 3D printer (generally the STL format), a 3D design that is to be 3D printed must meet a few basic requirements. These ensure that the 3D model prints correctly.

A 3D design file to be printed must be closed, or "watertight" as it is typically referred.

---

[6]http://meshlab.sourceforge.net/
[7]http://www.blender.org
[8]http://www.pdf3d.com/

All components in the 3D model should be connected to create a solid. Objects must typically also be manifold, i.e. have no edges that are shared between more than two faces. There should also be no parts of the model that have zero thickness. Individual and floating points, lines, and planes should be removed, since these do not have three separate directions necessary for printing. Finally, surface normals need to all be pointing in the same direction outward from the surface of the model. This ensures that the 3D printer does not 'confuse' the internal and outer surfaces of the model. Finally, as may be obvious, the 3D model must have the appropriate physical dimensions to be printed on the specific printer of choice (i.e. your model must fit in the printer).

While different 3D printers and 3D 'slicing' software may have more stringent requirements, we found in our work that the above were the minimal requirements necessary for a successful 3D print of our models. Creation of a 3D printable STL file follows nearly the same procedure as that outlined above for generating a U3D file for PDF display. One key distinction though is that most 3D printers are monochromatic, meaning they print using a single-color material per extruder. As such, the 'color' of the 3D model to be printed does not matter, since typically only one or two solid colors at most will be available. Color information is also (usually) not stored in the STL file to be printed, and the choice of color is more of a manual 'real-world' decision than something chosen in the file creation phase. Since we are mostly interested in the 3D geometry and dynamics of the WWIR, the main concern is preserving the overall 3D geometry of the design to be printed.

Thus, to create our 3D print files, we again visualize our SPH simulation data with VISIT or PARAVIEW, but once satisfied with a particular visualization, we export our design in the OBJ file format. In order to fit our 3D model in our printer, while at the same time preserving as much interesting detail as possible, we crop the outer spherical edge and choose to visualize and print only the region extending to radius $r = 7a \approx 108$ au from the system centre-of-mass. This is a fairly small cropping of the model, and for the orbital phases of interest, no crucial information is lost.

Once we create an OBJ file, we import it into BLENDER, which has useful tools for detecting and correcting non-manifoldness, mesh holes, loose objects, and inverted normals. We find that in most cases, the most prominent problem with 3D OBJ files exported by VISIT or PARAVIEW is that they have a large number of inverted normals. Luckily, these are easily corrected in BLENDER via a few simple mouse clicks. Once the normals are corrected, we use BLENDER to remove any floating points, lines, or faces that may lead to printing errors, and we close any open 'holes' that make the model non-watertight. Here, we must be careful to mention that a large 'hole' can exist in a model in a general physical sense and still allow that model to be 3D printable (see Results below). Instead, what matters is that the entire surface of the 3D model itself be closed, with all edges/faces connected.

To help guide the reader, using BLENDER, we add to our model two small spheres that are connected by a small thin cylinder, which represent the stars and illustrates their location and separation with respect to each other, the dense η_A wind, and the WWIR. In order to make the individual stars more visible at the scale of our models, we have increased

the radius of each sphere to be a factor 3.5 times larger than the correctly-scaled stellar radius. Thus, the spheres depicting the stars in Figures 5.7–5.15 have radii equivalent to 210 and 105 $R_{\odot}$ for η_A and η_B, respectively. The correct stellar separation to scale is used at each phase.

We make one other final adjustment in BLENDER before exporting our model to the STL format. This adjustment further ensures that our model fits the 3D printer and has a stable base on which to stand once it is printed. To provide an interesting scientific reference point for anyone viewing our 3D printed models, we rotate them to the correct derived orientation that the η Car binary has on the sky as seen from Earth, with an inclination $i = 138°$, argument of periapsis $\omega = 263°$, and position angle on the sky of the orbital angular momentum axis of $PA_z = 317°$ (see Madura et al. 2012; M13). Once rotated, we remove a small portion of the bottom of the model so that it has a flat base. We are careful to not remove any of the WWIR or cavity carved within the η_A wind by η_B. Only a small portion of the undisturbed outer spherical η_A wind is removed. This has no effect on our results or conclusions, but allows the 3D printed models to be placed on a flat surface and oriented to provide the viewer with an idea of how the system and WWIR appear on the sky, assuming North is up and East is left (see Figure 5.15).

To print our 3D models, we use a consumer-grade MakerBot Replicator 2X Experimental 3D Printer, which has dual-extrusion capabilities. We import our STL files into the freely-available MakerWare[9] 3D printing software and create the X3G files specific to the MakerBot printer. Since our 3D models are incredibly complex and, in many cases, contain free-hanging unsupported edges, we print our models in one color using one of the MakerBot's extruders, and use the second extruder to print dissolvable support material. Once printed, we place our model in a limonene bath, which safely dissolves away the support material. We use the highest layer resolution possible when printing (100 microns), and a physical size that occupies nearly the entire available build volume (model diameter ≈ 6 inches across its widest part).

Each 3D printed model consists of two parts, joined by small metal pins. The bottom half of each model consists of the dense η_A wind and the hollow η_B wind cavity, while the top half consists solely of the WWIR (dense post-shock η_A wind region). The two pieces are separable to allow the viewer to see the internal regions of the cavity carved by η_B in η_A's wind, or the WWIR by itself (see e.g. Figures 5.10 and 5.14). Additionally, we add two small beads connected by a short pin to represent the individual stars and illustrate their orientation and separation. The radii of the beads and their separation is to scale with the rest of the printed model, although as described above, the stellar radii have been increased by a factor of 3.5 to make the stars more easily visible.

Finally, we note that each 3D printable STL file is attached to this article as supplementary online material. Thus, anyone with access to a suitable 3D printer can in principle print their own η Car wind model(s). The STL format should be compatible with most, if not all, 3D printers currently on the market. The STL file should be 'ready to print'

---

[9]https://www.makerbot.com/desktop

without additional modifications, but due to differences in printers and printing software, we cannot guarantee that absolutely no modifications are necessary. At the very least, the model will need to be adjusted to physically fit the 3D printer being used. We also have only tried printing the models on a 3D printer with dual extrusion and dissolvable support material, and are unsure of the results of using a single-extrusion printer. We welcome readers with questions about 3D printing the models, the model creation/design, and/or the file creation process to contact us directly.

5.3 Results

5.3.1 The 3D visualizations

Figures 5.1–5.6 present the results of our 3D visualizations of η Car's inner WWIR, with color showing the logarithm of the density. Embedded within each 2D figure is an interactive 3D version of the model. Figures 5.1–5.3 correspond to the higher $\dot{M}_{\eta_A}$ Case A simulation, while Figures 5.4–5.6 correspond to the lower $\dot{M}_{\eta_A}$ Case C simulation. Case A is more representative of η_A's current $\dot{M}$ (M13), while Case C is included mainly to investigate how changes to $\dot{M}_{\eta_A}$ affect the overall 3D geometry of the WWIR. Each model shown has a radius $r = 7a \approx 108$ au, measured from the system centre-of-mass.

Figures 5.1 and 5.4 show that at apastron, the WWIR and cavity carved by η_B in η_A's dense wind have the expected nearly-axisymmetric conical shape, with the WWIR opening angle increasing with decreasing $\dot{M}_{\eta_A}$ (M13). However, one does not fully appreciate how dramatic the change in WWIR opening angle is until it is visualized in 3D. In Figure 5.1, the WWIR is conical, whereas in Figure 5.4, it is nearly a plane. Another interesting feature more clearly visible in the 3D renderings is the very slight distortion of the WWIR in the direction of orbital motion. This is due to the additional component to the wind velocities caused by the non-zero velocity of the stars about the system centre-of-mass.

We also see in Figures 5.1 and 5.4 that the WWIR is not a clean, smooth surface. Rather, it is corrugated and contains many smaller-scale bumps and protrusions that arise as a result of various instabilities, such as non-linear thin shell and Kelvin-Helmholtz (Parkin et al. 2011; M13). While somewhat difficult to see in the density-colored models of Figures 5.1 and 5.4, Figures 5.7 and 5.11 clearly show that the WWIR in the Case C simulation appears to contain much more detailed structure, including large trenches that extend into and around the surface of the WWIR that faces the observer. We are unsure if this means that the Case C result is intrinsically more unstable, or if the WWIR is simply better resolved as this SPH simulation used more SPH particles (by a factor of ~ 1.5) and had a slightly better numerical resolution.

Figures 5.2 and 5.5 illustrate the twisted 3D geometry of the WWIR at periastron. In both figures we find that the leading arm of the WWIR (near the apex) is highly twisted in the direction of orbital motion, whereas the spatially-extended outer remnant of the WWIR trailing arm, created before periastron, maintains some of its initial axisymmetric
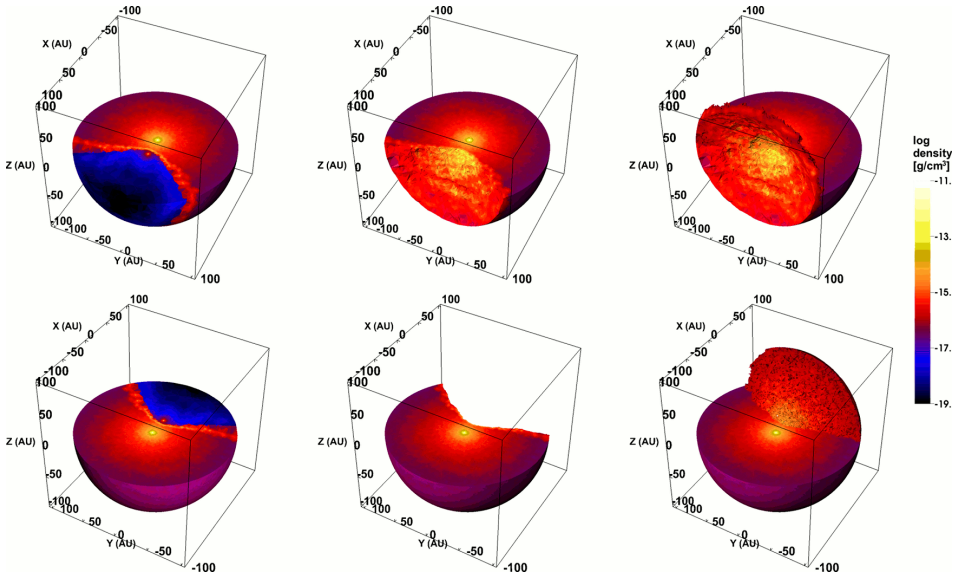
Figure 5.1 – 3D view of η Car's WWIR at apastron for the Case A ($\dot{M}_{\eta_A} = 8.5 \times 10^{-4}$ M$_\odot$ yr^{-1}) SPH simulation. The top left panel shows a (arbitrary) view looking down on the orbital plane, with the low-density η_B wind cavity opening toward the observer. The top half of the 3D model is transparent in order to clearly show the orbital plane. The top middle panel is the same as the first, but with the low-density η_B wind made completely transparent in order to better show the 3D structure of the η_B wind cavity. The top right panel is identical to the top middle panel, but also includes the 3D surface of the WWIR that exists above the orbital plane. Panels in the bottom row are identical to those in the top row, but show a 180° rotated view. Color shows log density in cgs units in all panels. Click the image for a 3D interactive version of the model (Adobe Reader® only. We suggest selecting "View in Floating Window" in the right-mouse-click drop-down menu). A small white sphere in the 3D interactive model marks the location of the companion η_B.

geometry. There is also more curvature of the WWIR apex in the Case A simulation than in the Case C simulation. In Case C (Figure 5.5), the WWIR is still amazingly flat and planar in shape, although with a 'twist' of the apex and a spatial displacement of the leading edge of the WWIR further into the pre-shock η_A wind.

One particularly interesting feature in the WWIR at periastron, visible in both $\dot{M}_{\eta_A}$ cases, is the large hole in the trailing arm near the WWIR apex. This WWIR hole is prominently located above (and below) the orbital plane, and is something not noticed in previous works that relied on 2D image slices through the orbital plane. This hole is a direct result of the fact that, at those locations where the hole exists, there is no longer a WWIR. Because of the extremely high orbital eccentricity and embedding of η_B within η_A's dense wind at periastron, η_B's outwardly expanding wind is unable to collide with η_A's downstream wind. The wind of η_B becomes trapped in specific directions at periastron and there is no longer any wind-wind collision at certain locations in the trailing wind. As a result, the unshocked primary wind starts expanding and filling in the low-density cavity that was carved by η_B's wind during the broad part of the orbit. The outermost
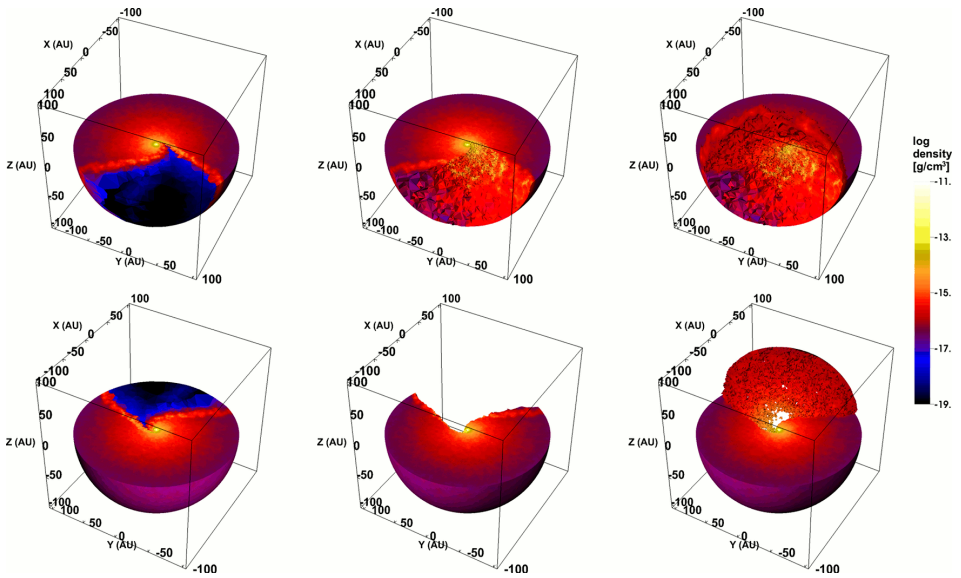
Figure 5.2 – Same as Figure 5.1, but at periastron. Click image for a 3D interactive model (Adobe Reader®) only).
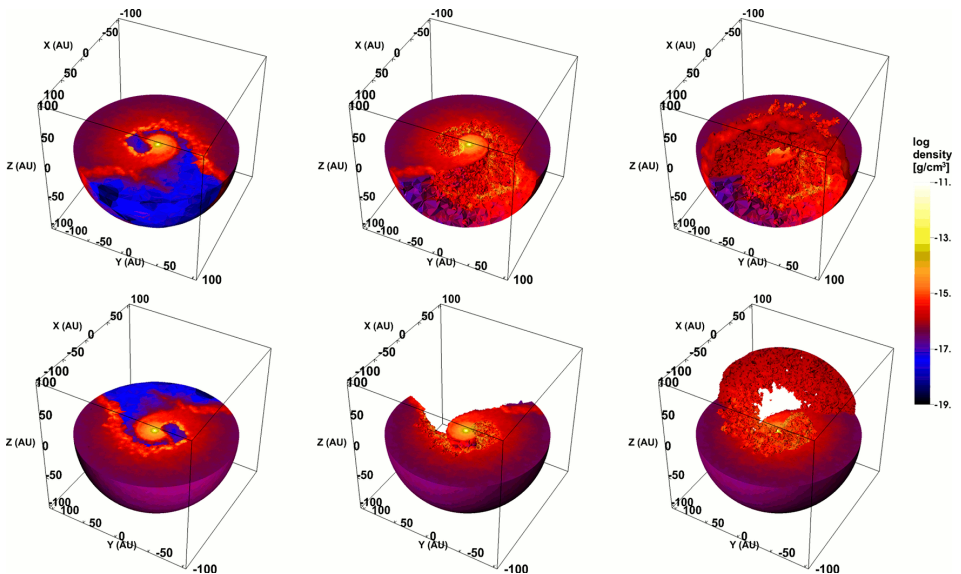
Figure 5.3 – Same as Figure 5.1, but at ≈ 3 months after periastron ($\phi = 1.045$). Click image for a 3D interactive model (Adobe Reader® only).

WWIR-trailing-arm located downstream from the hole remain intact at periastron simply because of time-delay effects; the hole near the apex has not had enough time to expand

and propagate downstream.

The size of the hole at periastron also appears to depend on $\dot{M}_{\eta_A}$, with Case A having a larger hole than Case C. This is consistent with the change in wind momentum ratio and WWIR opening angle as $\dot{M}_{\eta_A}$ is lowered. The fast wind from η_B is able to better compete against η_A's wind in Case C, and thus able to better maintain the trailing arm of the WWIR at periastron.

Of the three phases studied, that at ~ 3 months after periastron ($\phi = 1.045$, Figures 5.3 and 5.6) contains the most fascinating 3D WWIR geometry. As expected based on previous 3D simulations, a spiral cavity is carved within the dense wind of η_A by η_B's fast wind. However, the full 3D geometry of this cavity has never been visualized before, and we observe some interesting new features and phenomena that occur in both $\dot{M}_{\eta_A}$ simulations.

First, as alluded to above, as the 3D geometry of the WWIR evolves with time following periastron, the hole created near the WWIR apex at periastron expands and propagates downstream along the WWIR's old trailing arm. Thus, the new spiral WWIR created during periastron essentially has no trailing arm, and consists predominately of a leading arm and structures above and below the orbital plane. The hole created at periastron grows as the system moves through periastron and slowly eats its way into the remnant of the WWIR that was created during the broad part of the orbit. This effect is more prominent the higher the value of $\dot{M}_{\eta_A}$.

Next, we see that the spiral wind cavity carved by η_B within the back side of η_A's wind during periastron passage is much shallower than the cavity carved during the broad part of the orbit. This is due to the short amount of time η_B spends on the far side of η_A during periastron. The spiral wind cavity and new WWIR formed during periastron have yet to expand outward to a size comparable to the remnant cavity on the apastron side of the system.

The most surprising new set of features found at phase 1.045 are the protrusions or 'fingers' that extend radially outward from the spiral WWIR. More detailed examination reveals that these fingers are actually tubes that consist of a thin shell of cold ($T \sim 10,000$ K), dense, compressed post-shock η_A wind that is filled with hotter ($T \gtrsim 10^5$ K) post-shock η_B wind. Theses tubes penetrate into the unshocked η_A wind expanding on the periastron side of the system and extend slightly above and below the orbital plane from the leading arm of the WWIR. They do not extend perfectly vertically above or below the orbital plane. Instead, they point radially outward away from the stars. The fingers extend in the same direction that η_B's fast wind is able to collide with η_A's wind during periastron passage, and their location appears to be tied to the direction and speed of orbital motion around periastron.

The spatial extent of the protruding fingers is also quite impressive, being larger than the stellar separation at this phase (i.e. $\gtrsim 7$ au). Their diameter is on the order of several au. We expect that as the system evolves back toward apastron, the fingers will slowly expand and mix with the surrounding unshocked η_A wind.

We also find that $\dot{M}_{\eta_A}$ has some interesting effects on the 3D geometry of the WWIR
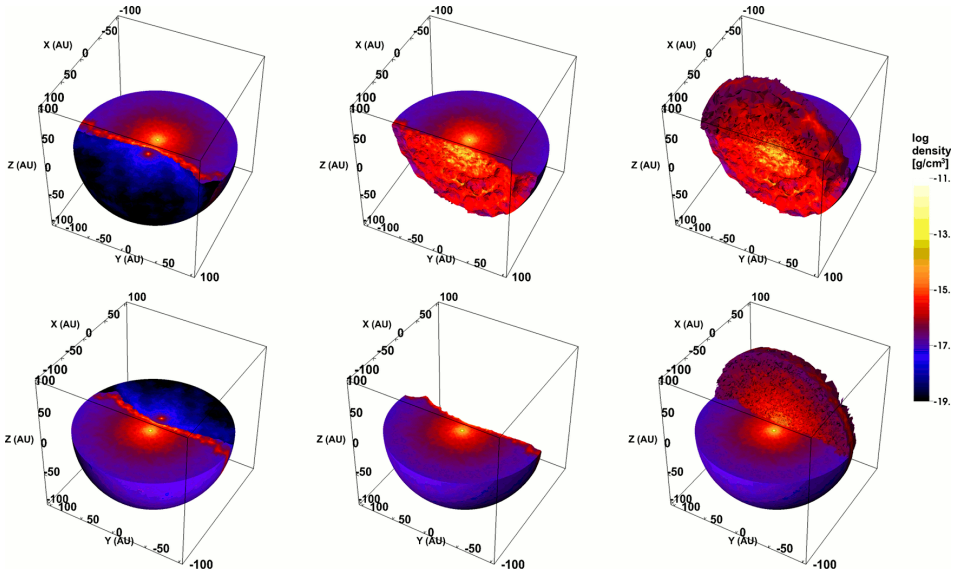
Figure 5.4 – Same as Figure 5.1, but for the Case C SPH simulation ($\dot{M}_{\eta_A} = 2.4 \times 10^{-4}$ M$_\odot$ yr^{-1}). Click image for a 3D interactive model (Adobe Reader® only).
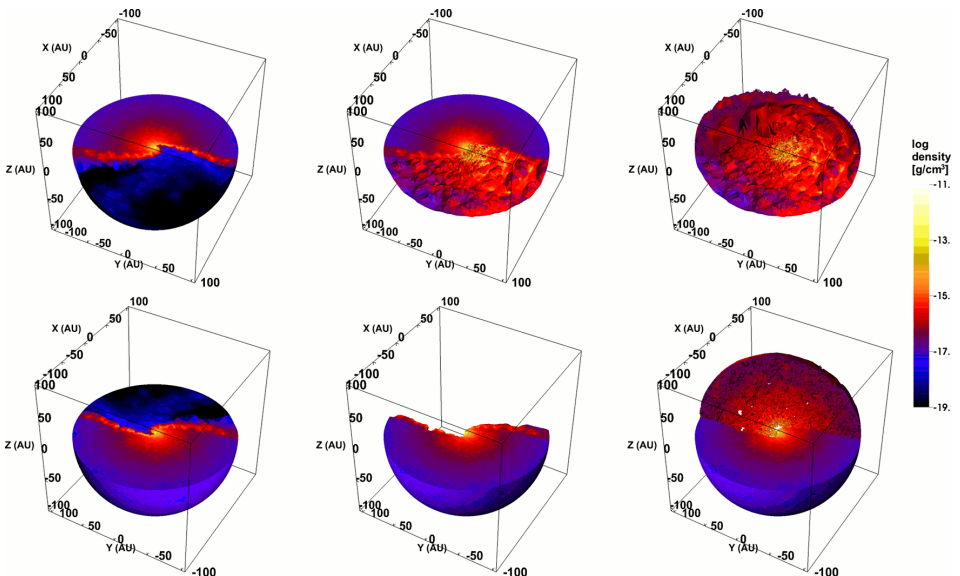
Figure 5.5 – Same as Figure 5.4, but at periastron. Click image for a 3D interactive model (Adobe Reader® only).

at $\phi = 1.045$. The WWIR in Case C appears to have fewer intact fingers. The protrusions present in Case C also appear to be shorter compared to those in Case A. Curiously,
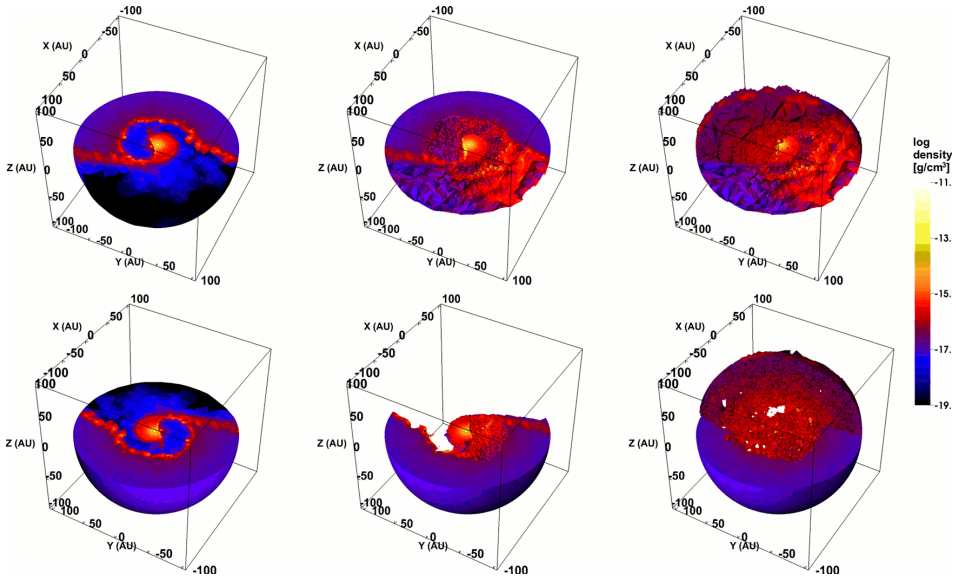
Figure 5.6 – Same as Figure 5.4, but at $\approx$ 3 months after periastron ($\phi = 1.045$). Click image for a 3D interactive model (Adobe Reader® only).

while the Case C WWIR lacks protrusions, it has an abundance of holes. We suspect that these holes in the WWIR are actually indicative of protrusions, ones in which the dense outer shell of post-shock η_A wind that defines the surface of the protrusion/tube has a $\delta < 2$. This idea is supported by examination of the wind cavity carved within η_A's dense wind (Figure 5.12), which exhibits small well-defined tubular cavities that extend into the outwardly expanding unshocked η_A wind. Moreover, the holes in the Case C WWIR all line up and point in the same direction as the protrusions that are present.

The spiral WWIR and wind cavity in Case C are also noticeably broader than in Case A. This is not surprising and is a result of the larger opening angle due to the lower $\dot{M}_{\eta_A}$ in Case C. What is intriguing is that in Case C, the outermost part of the leading arm of the 'current' WWIR between/around the stars is so large that it has caught up to and started to collide and merge with the remnant of the old trailing arm that formed long before periastron. In Case A at $\phi = 1.045$, the current WWIR has yet to reach the remains of the old trailing arm and there is still a large separation between it and the remnants of the trailing arm.

5.3.2   3D printing results

In Figures 5.7–5.14 we present our 3D printing results, showing a direct comparison between the actual 3D printed model and a 3D rendering of the model. We note that in each 3D interactive model, the default starting view has the model oriented at the same position on the sky as the η Car binary (Madura et al. 2012), i.e. the starting view shows

how an observer from Earth would see the system on the sky, with North up and East to the left. Additionally, in the 'Views' menu of the 3D graphics toolbar are options to display only the modified wind of η_A, only the WWIR, or both together. For those unable to view the 3D interactive graphics, we include Figures 5.10, 5.14, and 5.15, which show the model wind cavities and WWIRs at $\phi =$1.045 for Cases A and C, and how each model would appear on the sky to an observer on Earth, respectively. The STL files used for the prints are available as supplementary material in the online version of this article.

As demonstrated by the figures, we find that the 3D printed models reproduce remarkably well all of the key features observed in the 3D interactive visualizations. We were pleasantly surprised that individual features in the 3D unstructured meshes, such as protrusions and trenches, were faithfully reproduced. One can make out in some locations the tetrahedral grid cells used in the mesh. Even the small protruding fingers that extend radially from the WWIR at $\phi =$1.045 were reproduced and remained mostly intact. However, we did have one delicate finger on the Case A model accidentally break off, which was simply just glued back on (Figure 5.9).

The ability to physically hold and inspect the 3D models provides a completely new perspective on their 3D geometry and an improved sense of the scale of the different structures. One appreciates more just how large the 3D WWIR is compared to the stars and stellar separation. The 3D models are also useful for constraining the observer's line-of-sight to the binary system and help demonstrate why certain lines-of-sight are inconsistent with available observations. For example, as illustrated in Figure 5.15, at apastron, for the assumed orbital orientation, the observer's line-of-sight lies within the WWIR cavity, implying that any X-rays generated at the WWIR apex would be detectable to an observer at Earth. However, rotating the apastron model by 90 degrees or more places the observer's line-of-sight through the dense, optically-thick primary wind, which would absorb any X-rays emitted from the WWIR apex. Thus, we may safely rule out such lines-of-sight.

The above is just one very simple example of how the 3D print models can be used. More importantly, we find that the 3D print models are extremely useful as a visual aid to help explain to non-η Car experts, and even non-astronomers, the 3D geometry and dynamics of the binary and WWIR. The 3D prints are a useful tool for illustrating concepts, relationships, and properties that are not easily conveyed by 2D, and even 3D, graphics.

5.4   Discussion

The new 3D features discovered in our results may have some interesting implications for observational diagnostics of η Car and other highly-eccentric colliding wind binaries, such as WR 140. The hole near the apex of the WWIR that appears in the simulation snapshot at periastron will affect the generation of the shock-heated gas responsible for η Car's observed time-variable X-ray emission (Corcoran et al. 2010; Hamaguchi et al. 2007, 2014). Obviously, in areas where there is no wind-wind collision, there can be no shock-heated gas, and thus no thermal X-ray emission. Our 3D models imply that at
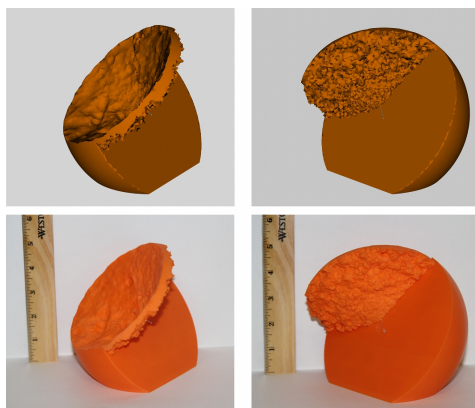
Figure 5.7 – Comparison between the 3D rendering (top row) and 3D printed model (bottom row) of the Case A SPH simulation at apastron. Columns present a (arbitrary) view of the WWIR with the observer looking into the η_B wind cavity (left), and a view of the opposite side with the η_B cavity opening away from the observer (right). Both views are looking down on the binary orbital plane. Click the image for a 3D interactive version of the model (Adobe Reader® only). Pre-programmed views are available under the "Views" menu in the 3D model toolbar. These include the projection of the system on the sky as viewed from Earth (view "LOS", North up, East left), the primary wind and η_B wind cavity only (view "PrimaryWind"), and the wind-wind collision region plus stars only (view "WWCR").
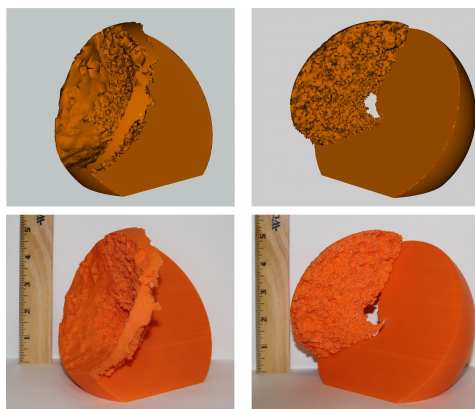
Figure 5.8 – Same as Figure 5.7, but at periastron. Click image for a 3D interactive model (Adobe Reader® only).

periastron, there should be no thermal X-ray emission from along the trailing arm. Furthermore, as $\dot{M}_{\eta_A}$ is lowered, it should take longer for the hot gas, and thus X-ray emission, to vanish from the WWIR trailing arm as periastron is approached.

The WWIR hole at periastron also provides us with information about the amount and type of material in line-of-sight at that time. Since there is no longer a WWIR directly in line-of-sight at periastron, the column density of material between us and the stars
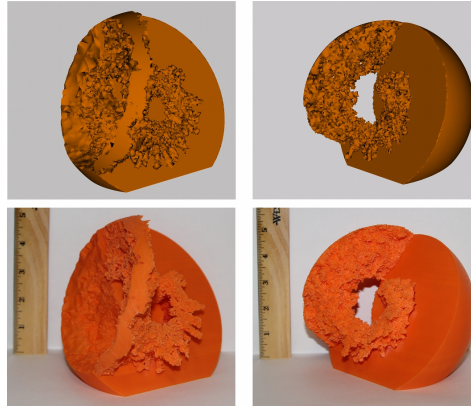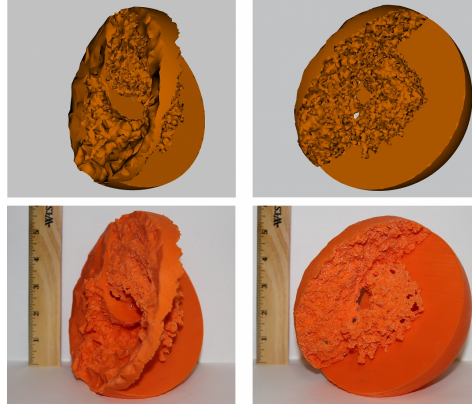
Figure 5.9 – Same as Figure 5.7, but at ≈ 3 months after periastron ($\phi = 1.045$). Click image for a 3D interactive model (Adobe Reader® only).
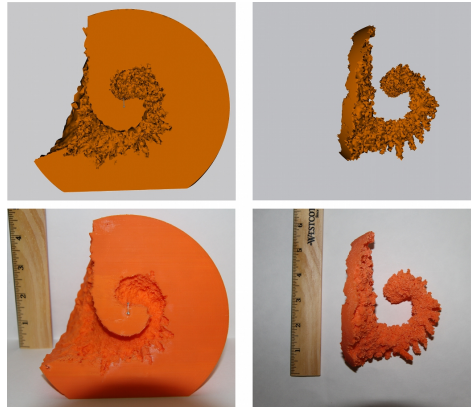

Figure 5.10 – Comparison between a 3D rendering of the Case A simulation at ≈3 months after periastron (top row) and the 3D printed model (bottom row) for the two separable pieces that compose the model. The left column shows the bottom half of the model with the dense η_A wind and η_B wind cavity. The right column shows the top half that consists solely of the WWIR.

is dominated by unshocked primary wind material that is flowing to fill the wind cavity carved by η_B during the broad part of the orbit. Interestingly, this situation makes 'wind-eclipses' by η_A of various observed features (e.g. X-rays, Corcoran et al. 2010, and He II emission, Teodoro et al. 2012) easier to achieve at periastron for two reasons. First, since there is no longer a trailing arm to the WWIR, the overall size of the WWIR and volume of shock-heated gas at periastron is much smaller, and therefore easier to eclipse. Second, the lack of a trailing arm to the WWIR allows the dense η_A wind to expand and fill the η_B cavity in line-of-sight, increasing the size of the eclipsing wind photosphere.

The observational implications of the fingers that protrude from the WWIR at phases ~3 months after periastron are unclear at this time. Unfortunately, if real, they are too
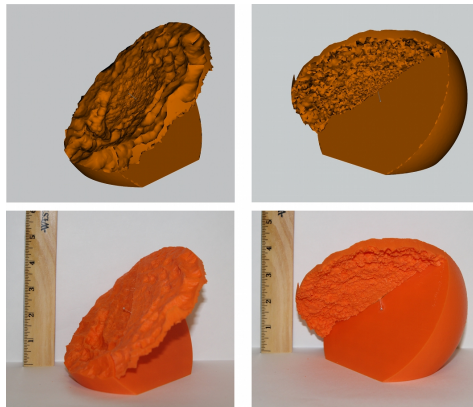
Figure 5.11 – Same as Figure 5.7, but for Case C. Click image for a 3D interactive model (Adobe Reader®
only).
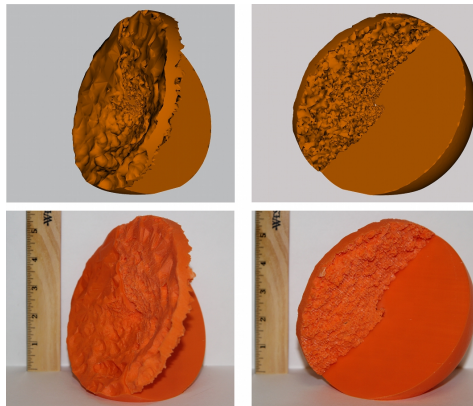
Figure 5.12 – Same as Figure 5.11, but at periastron. Click image for a 3D interactive model (Adobe Reader®
only).

small to spatially resolve, even with *HST*. Hot gas within the tubular fingers may produce
X-rays, but the intensity of any such X-ray emission is likely to be small compared to
that of X-rays generated near the WWIR apex. It is also unclear if the shocks responsible
for producing the fingers could contribute to the He II λ4686 emission observed across
η Car's periastron passage. Portions of the fingers located within η_A's inner He$^+$ zone may
be able to produce a small amount of He II emission if the shocks produce the required
He$^+$-ionizing photons. However, this is very speculative without more detailed modeling.

It is difficult to constrain the observational implications of the WWIR fingers at this
time because we lack a thorough understanding of their physical origins and properties. We
currently speculate that the fingers arise as a result of instabilities at the interface between
the two wind shocks, which undergo rapid complex changes around periastron due to the

Figure 5.13 – Same as Figure 5.11, but at $\approx$ 3 months after periastron ($\phi = 1.045$). Click image for a 3D interactive model (Adobe Reader® only).
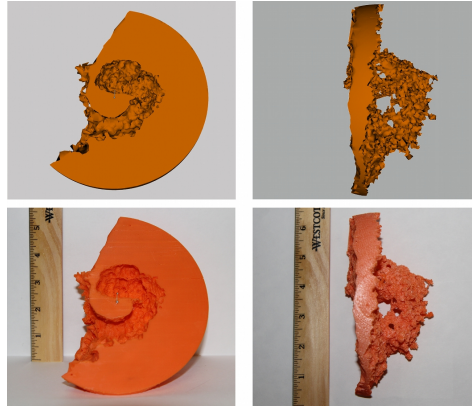
Figure 5.14 – Same as Fig 5.10, but for Case C.

high orbital eccentricity and wind directions. We point out that during the creation of the spiral WWIR, a typical wind-wind collision does not take place, due to the much faster orbital motion of the stars. The leading arm of the spiral WWIR is formed not by a head-on collision of two spherical winds, but rather by the fast receding η_B wind colliding with the much denser and slower *receding* η_A wind. This collision still produces a pair of shocks, but the situation is now more analogous to that which occurs when a stellar wind interacts with a surrounding circumstellar shell (e.g. Toalá & Arthur 2011; van Marle & Keppens 2012), with the post-shock η_A wind forming a thin, dense shell via radiative cooling, and the post-shock η_B wind remaining hot and cooling adiabatically.

Because of the high density contrast between the stellar winds, and because the faster η_B wind is pushing into and accelerating the slower η_A wind, different instabilities, including thin-shell (Vishniac 1983, 1994) and Rayleigh-Taylor (RT Young et al. 2001; Toalá &
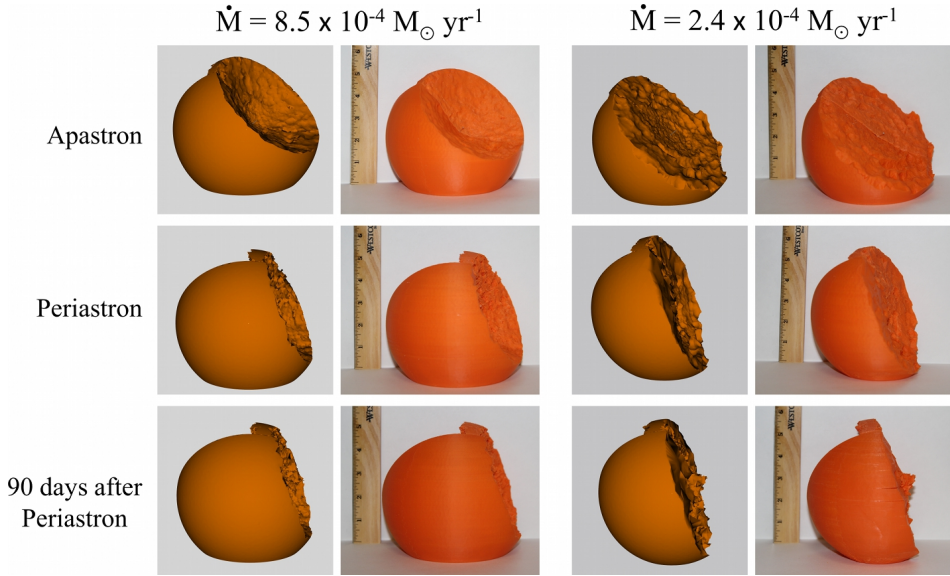
Figure 5.15 – Comprehensive comparison between the 3D renderings and 3D printed models, with all models oriented as the system would appear on the sky to an observer on Earth (North is up, East is left). Rows (from top to bottom) present the three different orbital phases. The first two columns show, respectively, the 3D rendering and the 3D printed model, for Case A. The last two columns are the same as the first, but for Case C.

Arthur 2011; van Marle & Keppens 2012), are expected to arise and greatly distort/disrupt the geometry of the spiral WWIR. Features very similar to the protrusions that we observe in our models are visible in the wind-wind hydrodynamic simulations of Toalá & Arthur (2011) (see e.g. their figures 12). The protrusions that arise in the simulations of Toalá & Arthur (2011) are a result of the thin-shell and RT instabilities. While not quite of the same magnitude as what we observe in our simulations, the 3D binary colliding wind simulations of Pittard (2009, their figures 10) and Parkin et al. (2011, their figures 12 and 13) also show similar features shortly after periastron, wherein the lower-density secondary wind penetrates into the denser primary wind due to thin-shell instabilities. Since Pittard (2009) and Parkin et al. (2011) present mostly 2D slices in the orbital plane of their simulations, we cannot be completely sure that the protrusions we observe are the same as the phenomenon shown in their figures. However, one reason such features may be stronger in our simulations is because our stellar winds have a larger density contrast than those in Pittard (2009), Parkin et al. (2011).

Our interpretation that the fingers are due to strong instabilities that form in the WWIR around periastron makes qualitative sense, but we note that standard SPH schemes are notorious for under-resolving shocks and instabilities (Agertz et al. 2007; Price 2008). Thus, our results should be interpreted with caution until a more detailed analysis is performed. Simulations using a grid-based method are necessary to determine if the fingers are real or an artifact of the SPH scheme. Such simulations will be the subject of future

work. However, the fact that the hydrodynamic simulations of Toalá & Arthur (2011), van Marle & Keppens (2012), Pittard (2009), and Parkin et al. (2011) were performed using grid-based methods and produced qualitatively similar phenomena supports the idea that the protrusions we observe are, to some extent, real. The timing and location of the fingers' appearance also makes physical sense on the grounds that they appear only during the rapid periastron passage, and occur only in the directions in which the fast wind of η_B strongly collides with the slow, dense receding wind of η_A.

5.5 Summary and Conclusions

In this work we present the first 3D prints of output from 3D SPH simulations of a dynamic astrophysical system. We demonstrate the methodology used to incorporate 3D interactive figures into a PDF document and the benefits of using 3D visualization and 3D printing as tools to analyze data from multidimensional numerical simulations. In this paper, we investigate the 3D structure of the WWIR in the the innermost regions of the η Car binary system. Below we summarize our most important results.

1. Several features in the overall geometry of the WWIR (e.g. changes in the opening angle due to different $\dot{M}_{\eta_A}$, distortions of the cone cavity due to the orbital motion, and irregularities on the WWIR surface due to various instabilities) are fully and more easily appreciated with the help of 3D visualization.

2. The inability of η_B's wind to collide with η_A's downstream wind produces a large hole in the trailing arm near the WWIR apex at periastron. The size of this hole is directly connected with the wind momentum ratio, and therefore the WWIR opening angle. As expected, the higher $\dot{M}_{\eta_A}$ in Case A causes a larger hole than that in Case C. After periastron, the hole expands and propagates downstream along the vanishing WWIR trailing arm.

3. The faster orbital motion during periastron passage produces a much shallower spiral wind cavity on the back side of η_A's wind compared to the nearly-axisymmetric conical cavity carved during the broad part of the orbit.

4. The 3D models present new 'finger-like' features at phase 1.045. These protrusions extend radially, above and below the orbital plane, outward from the spiral WWIR for several au. The WWIR in Case C exhibits large holes together with the protrusions. The presence of tubular cavities carved in η_A's dense wind support the idea that these holes are actually indicative of protrusions with $\delta < 2$.

5. We speculate that the newly-identified finger-like protrusions are a result of thin-shell and other instabilities that arise where the receding fast η_B wind collides with the dense, receding η_A wind. Future simulations using grid-based methods are needed to confirm the existence of the fingers and determine their physical origin and properties.

6. The Case C model shows that at phase 1.045, the outermost part of the leading arm of the 'current' WWIR reaches and starts to merge with the remnant of the old trailing arm formed before periastron. In contrast, for Case A, there is still a large gap between the 'current' WWIR and the remnants of the trailing arm.

7. 3D models can be used to better visualize and constrain, for example, the observer's line-of-sight to the binary system, an important parameter to correctly interpret and model available observations. The 3D prints are also very useful for conveying complex ideas to non-experts.

We demonstrate in this paper how software that generates 3D models, together with interactive 3D graphics in PDFs, can be used to produce publication-quality, scientifically instructive figures. Moreover, we show that 3D printed models reproduce extremely well the key features observed in the 3D interactive visualizations. Even if we have only touched on the possible applications of 3D printed models as a tool, this work helps highlight the important role 3D printing can play in understanding complex time-varying astrophysical systems. The ability to physically interact with the 3D models provides a completely new way to visualize, analyse, understand, and disseminate such 3D simulations. 3D print models are also extremely useful to show and explain to a non-expert or non-scientist the 3D geometry and dynamics of numerical simulations of astrophysical phenomena. Thus, 3D printing and visualization have the potential to improve the astrophysical community's ability to convey advances in our disciplines to the wider public, providing an opportunity for them to play a more active role in their learning by 3D printing various models. PDF is also the most widely-used, self-contained electronic document format, implying that funding agencies, governments, and the public can easily interact with instructive, 3D representations of our work (Barnes & Fluke 2008). We hope that this paper motivates others in the astrophysical community to pursue the use of 3D interactive visualization and 3D printing in their research and publications.

Bibliography
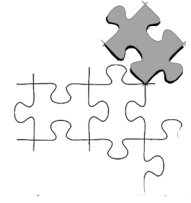
Agertz O. et al., 2007, MNRAS, 380, 963

Barnes D. G., Fluke C. J., 2008, New A, 13, 599

Christian C. A. et al., 2014, in American Astronomical Society Meeting Abstracts, Vol. 223, American Astronomical Society Meeting Abstracts #223, p. 244.16

Clementel N., Madura T. I., Kruip C. J. H., Icke V., Gull T. R., 2014a, MNRAS, 443, 2475

Clementel N., Madura T. I., Kruip C. J. H., Paardekooper J.-P., 2014b, MNRAS

Corcoran M. F., 2005, AJ, 129, 2018

Corcoran M. F., Hamaguchi K., Pittard J. M., Russell C. M. P., Owocki S. P., Parkin E. R., Okazaki A., 2010, ApJ, 725, 1528

Corcoran M. F., Ishibashi K., Swank J. H., Petre R., 2001, ApJ, 547, 1034

Crowther P. A., 2007, ARA&A, 45, 177

Damineli A., 1996, ApJ, 460, L49

Damineli A., Conti P. S., Lopes D. F., 1997, New A, 2, 107

Damineli A. et al., 2008a, MNRAS, 386, 2330

Damineli A. et al., 2008b, MNRAS, 384, 1649

Davidson K., Humphreys R. M., 1997, ARA&A, 35, 1

Du Q., Wang D., 2006, J. Comput. Appl. Math., 195, 8, special Issue: The International Symposium on Computing and Information (ISCI2004)

Fahed R. et al., 2011, MNRAS, 418, 2

Ferland G. J., Korista K. T., Verner D. A., Ferguson J. W., Kingdon J. B., Verner E. M., 1998, PASP, 110, 761

Franco J., Tenorio-Tagle G., Bodenheimer P., 1990, ApJ, 349, 126

Friedrich M. M., Mellema G., Iliev I. T., Shapiro P. R., 2012, MNRAS, 421, 2232

Gayley K. G., Owocki S. P., Cranmer S. R., 1997, ApJ, 475, 786

Gomez H. L., Vlahakis C., Stretch C. M., Dunne L., Eales S. A., Beelen A., Gomez E. L., Edmunds M. G., 2010, MNRAS, 401, L48

Groh J. H., Damineli A., 2004, IBVS, 5492, 1

Groh J. H., Hillier D. J., Madura T. I., Weigelt G., 2012a, MNRAS, 423, 1623

Groh J. H., Madura T. I., Hillier D. J., Kruip C. J. H., Weigelt G., 2012b, ApJ, 759, L2

Groh J. H., Madura T. I., Owocki S. P., Hillier D. J., Weigelt G., 2010a, ApJ, 716, L223

Groh J. H. et al., 2010b, A&A, 517, A9

Gull T. R., Madura T. I., Groh J. H., Corcoran M. F., 2011, ApJ, 743, L3

Gull T. R. et al., 2009, MNRAS, 396, 1308

Hamaguchi K. et al., 2007, ApJ, 663, 522

Hamaguchi K. et al., 2014, ApJ, 784, 125

Henley D. B., Corcoran M. F., Pittard J. M., Stevens I. R., Hamaguchi K., Gull T. R., 2008, ApJ, 680, 705

Hillier D. J., Davidson K., Ishibashi K., Gull T., 2001, ApJ, 553, 837

Hillier D. J. et al., 2006, ApJ, 642, 1098

Humphreys R. M., Davidson K., Koppelman M., 2008, AJ, 135, 1249

Ishibashi K. et al., 2003, AJ, 125, 3222

Kruip C., 2011, PhD thesis, University of Leiden, Leiden, the Netherlands

Kruip C. J. H., Paardekooper J.-P., Clauwens B. J. F., Icke V., 2010, A&A, 515, A78

Lefèvre L. et al., 2005, MNRAS, 360, 141

Linsen L., Molchanov V., Dobrev P., Rosswog S., Rosenthal P., Long T. V., 2011, Smoothviz: Visualization of smoothed particle hydrodynamics data. pp. 3–28

Luo D., McCray R., Mac Low M.-M., 1990, ApJ, 362, 267

Madura T. I., 2010, PhD thesis, University of Delaware

Madura T. I., Groh J. H., 2012, ApJ, 746, L18

Madura T. I. et al., 2013, MNRAS, 436, 3820

Madura T. I., Gull T. R., Owocki S. P., Groh J. H., Okazaki A. T., Russell C. M. P., 2012, MNRAS, 420, 2064

Martin J. C., Davidson K., Humphreys R. M., Hillier D. J., Ishibashi K., 2006, ApJ, 640, 474

Martins F., Schaerer D., Hillier D. J., 2005, A&A, 436, 1049

Mehner A., Davidson K., Ferland G. J., Humphreys R. M., 2010, ApJ, 710, 729

Mehner A., Davidson K., Humphreys R. M., Ishibashi K., Martin J. C., Ruiz M. T., Walter F. M., 2012, ApJ, 751, 73

Mehner A., Davidson K., Martin J. C., Humphreys R. M., Ishibashi K., Ferland G. J., 2011, ApJ, 740, 80

Mellema G., Iliev I. T., Alvarez M. A., Shapiro P. R., 2006, New A, 11, 374

Molchanov V., Fofonov A., Rosswog, S.and Rosenthal P., Linsen L., 2013, in 8th International SPHERIC Workshop, 8th International SPHERIC Workshop, pp. 350–356

Monaghan J. J., 1992, ARA&A, 30, 543

Monaghan J. J., 2005, Reports on Progress in Physics, 68, 1703

Monnier J. D., Tuthill P. G., Danchi W. C., 1999, ApJ, 525, L97

Nielsen K. E., Corcoran M. F., Gull T. R., Hillier D. J., Hamaguchi K., Ivarsson S., Lindler D. J., 2007, ApJ, 660, 669

Okazaki A. T., Owocki S. P., Russell C. M. P., Corcoran M. F., 2008, MNRAS, 388, L39

Osterbrock D. E., Ferland G. J., 2006, Astrophysics of gaseous nebulae and active galactic nuclei

Owocki S., 2007, in Astronomical Society of the Pacific Conference Series, Vol. 367, Massive Stars in Interactive Binaries, St.-Louis N., Moffat A. F. J., eds., p. 233

Paardekooper J.-P., 2010, PhD thesis, Ph. D. thesis, University of Leiden (2010)

Paardekooper J.-P., Kruip C. J. H., Icke V., 2010, A&A, 515, A79

Paardekooper J.-P., Pelupessy F. I., Altay G., Kruip C. J. H., 2011, A&A, 530, A87

Parkin E. R., Pittard J. M., Corcoran M. F., Hamaguchi K., 2011, ApJ, 726, 105

Parkin E. R., Pittard J. M., Corcoran M. F., Hamaguchi K., Stevens I. R., 2009, MNRAS, 394, 1758

Parkin E. R., Sim S. A., 2013, ApJ, 767, 114

Pawlik A. H., Schaye J., 2008, MNRAS, 389, 651

Pelupessy F. I., van Elteren A., de Vries N., McMillan S. L. W., Drost N., Portegies Zwart S. F., 2013, A&A, 557, A84

Pittard J. M., 2009, MNRAS, 396, 1743

Pittard J. M., Corcoran M. F., 2002, A&A, 383, 636

Pittard J. M., Stevens I. R., Corcoran M. F., Ishibashi K., 1998, MNRAS, 299, L5

Price D. J., 2007, PASA, 24, 159

Price D. J., 2008, Journal of Computational Physics, 227, 10040

Ritzerveld J., Icke V., 2006, Phys. Rev. E, 74, 026704

Ritzerveld N. G. H., 2007, PhD thesis, Leiden Observatory, Leiden University, P.O. Box 9513, 2300 RA Leiden, The Netherlands

Russell C. M. P., 2013, PhD thesis, University of Delaware, Newark, DE, USA

Shapiro P. R., Iliev I. T., Alvarez M. A., Scannapieco E., 2006, ApJ, 648, 922

Smith N., 2005, MNRAS, 357, 1330

Smith N., 2006, ApJ, 644, 1151

Smith N., Gehrz R. D., Hinz P. M., Hoffmann W. F., Hora J. L., Mamajek E. E., Meyer M. R., 2003, AJ, 125, 1458

Steffen W. et al., 2014, MNRAS, 442, 3316

Steiner J. E., Damineli A., 2004, ApJ, 612, L133

Stevens I. R., Blondin J. M., Pollock A. M. T., 1992, ApJ, 386, 265

Stevens I. R., Pollock A. M. T., 1994, MNRAS, 269, 226

Teodoro M. et al., 2012, ApJ, 746, 73

Teodoro M., Damineli A., Sharp R. G., Groh J. H., Barbosa C. L., 2008, MNRAS, 387, 564

Teodoro M., Madura T. I., Gull T. R., Corcoran M. F., Hamaguchi K., 2013, ApJ, 773, L16

Toalá J. A., Arthur S. J., 2011, ApJ, 737, 100

Townsend R. H. D., 2009, ApJS, 181, 391

Tuthill P. G., Monnier J. D., Danchi W. C., 1999, Nature, 398, 487

van Marle A. J., Keppens R., 2012, A&A, 547, A3

Verner E., Bruhweiler F., Gull T., 2005, ApJ, 624, 973

Vishniac E. T., 1983, ApJ, 274, 152

Vishniac E. T., 1994, ApJ, 428, 186

Vogt F. P. A., Dopita M. A., Kewley L. J., Sutherland R. S., Scharwächter J., Basurah H. M., Ali A., Amer M. A., 2014, ApJ, 793, 127

Vogt F. P. A., Shingles L. J., 2013, Ap&SS, 347, 47

Weigelt G., Ebersberger J., 1986, A&A, 163, L5

Whitelock P. A., Feast M. W., Marang F., Breedt E., 2004, MNRAS, 352, 447

Williams P. M., Rauw G., van der Hucht K. A., 2009, MNRAS, 395, 2221

Young Y.-N., Tufo H., Dubey A., Rosner R., 2001, J. Fluid Mech., 447, 377

Samenvatting
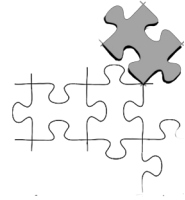
In een met sterren bezaaide nacht op het zuidelijk halfrond zou je, spelend met een telescoop, het sterrenbeeld Carina kunnen tegenkomen. De naam "Carina" (Kiel) verwijst naar het schip van de Argonauten. Laat je niet afleiden door Canopus, de op een na helderste ster aan de hemel, want we willen hier onze aandacht vestigen op de helderste interstellaire wolk aan de hemel: de Carina Nevel. Daarin bevindt zich η (Eta) Carinae, een dubbelster die bestaat uit een paar van de zwaarste en meest lichtsterke sterren die we kennen. Zulke sterren eindigen door een supernova-explosie, waarbij het grootste deel van de massa met vele tienduizenden kilometers per seconde de ruimte in geslingerd wordt. Uiteindelijk zal ook Eta Carinae dit stadium bereiken, zelfs overdag zichtbaar zijn en zoveel licht uitstralen dat je er 's nachts bij kunt lezen.

Sterren met zo'n hoge massa (ongeveer tien tot honderd maal zoveel als de Zon) spelen een zeer belangrijke rol in de geschiedenis en evolutie van het Heelal. Uit waterstof en helium maken zij door kernreacties de zwaardere elementen van onze wereld. Die stoffen verrijken het interstellair medium via sterrenvlammen, sterrenwind, en aan het einde van hun leven via supernova-explosies.

Vanwege hun grote massa zijn deze sterren zeer helder en heet. Ze stoten lichtdeeltjes (fotonen) uit die worden opgevangen door kosmisch gas en stof, en daarna weer uitgestraald. Door die wisselwerking veranderen de golflengte en de trillingsrichting van het licht. Dat kunnen wij waarnemen met onze ogen of door een telescoop. Astronomen gebruiken deze informatie om de bron (sterren) en de eigenschappen van gas en kosmisch stof te bestuderen. De kernfusie gaat in deze extreem hete sterren zeer snel, zodat zij weliswaar zeer helder zijn, maar ook kort leven: enkele tientallen miljoenen jaren. Mede daardoor zijn ze heel zeldzaam, en is onze kennis van deze sterren beperkt, hoewel ze zeer belangrijk zijn voor de evolutie van de kosmos.

Al sinds 1837 heeft Eta Carinae de astronomen geboeid. In die jaren begon haar helderheid te variëren en werd zelfs enige tijd bijna zo fel als Sirius, de helderste ster aan de hemel. Eta Carinae bleef ruim tien jaar zeer helder. Tijdens deze "Grote Uitbarsting" stootte de zwaarste van de twee sterren een flink deel van haar massa uit (waarschijnlijk
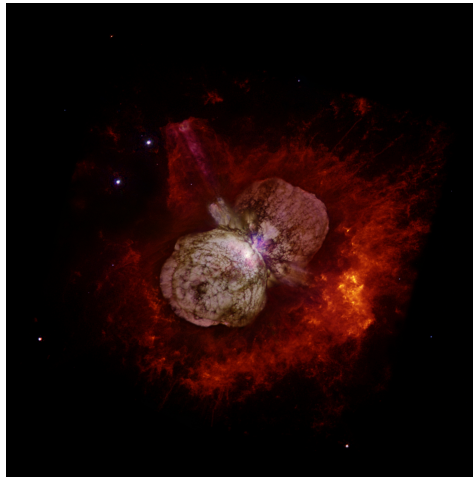
Figuur 5.16 – Wolk van gas en stof rondom de haltervormige "Homunculus" nevel, in het centrum waarvan zich de zware dubbelster Eta Carinae bevindt. Opname met de Hubble Space Telescope door Nathan Smith (University of California, Berkeley), ©NASA

10–20 zonsmassa's). Door deze ontploffing ontstond een nevel in de vorm van het cijfer 8, sindsdien bekend als *Homunculus* (zie Figuur 5.16). Door de explosie en de nieuwe nevel trok Eta Carinae sterk de aandacht. Maar de uitgeworpen materie heeft de ster bijna geheel onzichtbaar gemaakt.

In de afgelopen jaren is Eta Carinae een van de meeste bestudeerde stersystemen van onze Melkweg geworden. Er zijn al veel waarnemingen en theoretische modellen beschikbaar, maar er blijft nog veel te onderzoeken. Eta Carinae is een dubbelster, zodat het niet makkelijk is te bepalen wat daarmee gebeurt. Maar juist daarom is dit stelsel extra interessant. In een dubbelster worden twee sterren bijeengehouden door hun onderlinge zwaartekracht en bewegen in elliptische banen om elkaar heen. De *excentriciteit* (afplatting) van de baan geeft aan hoeveel deze afwijkt van een cirkel. Er zijn twee speciale posities op een elliptische baan: het *apastron*, waar de afstand tussen de sterren het grootst is, en het *periastron* waar die het kleinst is.

Beide sterren van Eta Carinae hebben een grote massa: waarschijnlijk 90 zonsmassa's in de primaire η_A en 30 zonsmassa's in de secundaire η_B ster. Zulke zware sterren zijn zo heet, dat zij hun atmosfeer de ruimte in blazen: een sterrenwind. De sterrenwinden van η_A en η_B hebben verschillende dichtheid en snelheid. Die van η_A is dichter (meer atomen per kubieke meter), die van η_B sneller (meer meters per seconde). Waar de twee winden elkaar ontmoeten, ontstaat een zeer ingewikkeld botsingsgebied. De vorm daarvan, en de manier waarop de gassen door de ruimte stromen, wordt bepaald door de dichtheid en de snelheid van de winden, en natuurlijk door de baanbeweging van de dubbelster. De sterkste wind, die met de grootste impuls (massa vermenigvuldigd met snelheid), buigt de zwakste terug in de vorm van een afgeronde kegel (zie Figuur 5.17). Door de heftige

botsing worden de gassen zeer heet en tot grote dichtheid samengeperst.

Omdat de baan van Eta Carinae een grote excentriciteit heeft, is die zeer afgeplat. Het grootste deel van de omloopstijd (5.5 jaar) bewegen de sterren vrij langzaam in de buurt van het apastron. Dan duiken ze in enkele maanden op elkaar af, vliegen razendsnel langs elkaar heen waarbij ze het periastron passeren, en keren terug naar het apastron. Theoretische berekeningen laten zien dat tijdens zo'n periastron-passage het botsingsgebied tussen de sterren wordt opgevouwen in een ingewikkelde 'knoop' van hete en turbulente gassen (zie Figuur 5.18).
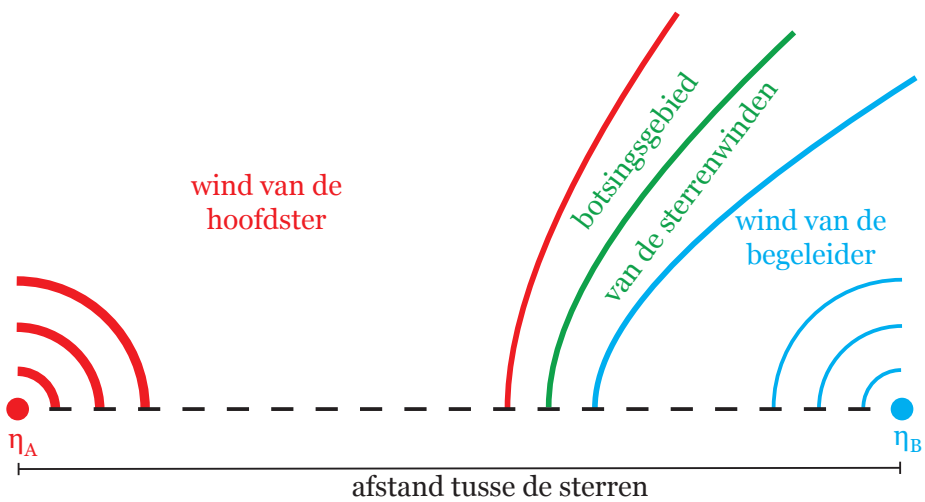
Figuur 5.17 – Schets van de botsing van twee sterrenwinden in een dubbelster. De vorm van het botsingsgebied ontstaat doordat de sterkste wind de zwakkere terugbuigt tot een afgeronde kegel.
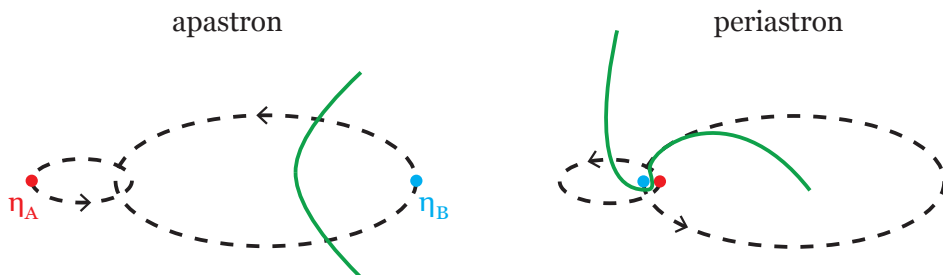
Figuur 5.18 – Schets van de elliptische baanbeweging van een dubbelster, gezien in het baanvlak. Links: toestand omstreeks apastron, rechts: toestand omstreeks periastron. De groene lijn geeft aan waar de winden botsen.

Het onderzoek van zulke ingewikkelde systemen als Eta Carinae vereist vele nauwkeurige waarnemingen met de beste telescopen, en vele modellen op basis van numerieke berekeningen met de beste computercodes. In de theoretische modellen moet zoveel mogelijk van de relevante natuurkunde worden opgenomen: voornamelijk baanbeweging, gasdynamica, thermodynamica, en stralingsprocessen. Vooral dit tweede aspect vormt het onderwerp van dit proefschrift: de ontwikkeling van deze modellen door de berekening van de wisselwerking tussen gas en straling. De baanbeweging volgt uit de klassieke mechanica, de gasdynamica beheerst de beweging van de sterrenwinden en hun botsing, de thermodynamica en de stralingsprocessen bepalen de toestand van de gassen. Door het felle licht van de hete sterren worden elektronen losgeslagen uit de atomen van het gas (*ionisatie*). Om die te berekenen hebben we gebruik gemaakt van driedimensionale simulaties van botsingen tussen de winden in Eta Carinae. Het gedrag van de straling is berekend met behulp van SimpleX, een computercode die berekent hoe de door de sterren uitgezonden fotonen zich verspreiden en wisselwerken met het gas.

Het hoofddoel van dit proefschrift is, de doeltreffenheid van SimpleX te gebruiken, aan te passen en uit te breiden voor de studie van het gas in systemen als Eta Carinae (Hoofdstuk 2). Met deze versie van SimpleX krijgen wij een sterk verbeterd inzicht in de ionisatie, wat nodig is om de modellen met de waarnemingen te vergelijken en die te begrijpen. De vorm, dichtheid en temperatuur van het gebied waar de sterrenwinden botsen hangt sterk af van de samenstelling en beweging van het gas. Vooral het geioniseerde volume is hier gevoelig voor. Bij minder winddichtheid in de eerste ster η_A, neemt het volume van het geioniseerde gas toe. Door de resultaten van de numerieke berekeningen te vergelijken met de waarnemingen kunnen wij een ondergrens stellen aan de dichtheid van het gas weggeblazen door de zwaarste ster (Hoofdstukken 2 en 3).

De talrijke gegevens die door waarnemingen zijn verkregen over Eta Carinae tonen sterke veranderingen als de sterren door het periastron gaan. Vooral het bestuderen van deze fase geeft meer informatie over de geometrie van het systeem en de fysieke eigenschappen van de twee sterren. De simulaties beschreven in Hoofdstukken 3 en 4 onderzoeken de ionisatie van het gas bij apastron en periastron.

De moeilijkheden omtrent het maken van modellen van Eta Carinae strekken zich uit voorbij de numerieke details van de programmatuur en de simulaties. Ook het aanschouwelijk maken van de ingewikkelde resultaten van de driedimensionale simulaties is een delicate zaak. Met behulp van een 3D-printer hebben wij ruimtelijke modelletjes gemaakt op basis van hydrodynamische berekeningen van de botsing tussen de sterrenwinden in Eta Carinae (Hoofdstuk 5). De mogelijkheid om deze voorwerpen ter hand te nemen schept nieuwe manieren om zowel de waarnemingen als de resultaten van simulaties te beschouwen, te analyseren en te tonen. Dat is in het bijzonder belangrijk bij de communicatie met niet-deskundigen.

In de afgelopen jaren heeft men mij meer dan eens gevraagd: "Waarom zou je Eta Carinae bestuderen?" Even afgezien van duidelijk wetenschappelijke motieven, meen ik dat het antwoord zou kunnen zijn: kennis en nieuwsgierigheid. Het is de aandrang, de wens en het plezier, gevestigd in de menselijke geest, om aan een puzzel die niet af is, een

stukje toe te voegen, al is het er maar een. Ter zake van de wetenschap is Eta Carinae, vanwege de nabijheid ervan en de beschikbaarheid van uitstekende waarnemingen, een voortreffelijk laboratorium om de talrijke aspecten van het ontstaan en de evolutie van zware sterren te bestuderen. In het bijzonder de verscheidene wisselwerkingen tussen de sterren in een dubbelster veroorzaken tal van belangrijke verschijnselen, die nog niet geheel begrepen zijn.

Het werk dat in dit proefschrift wordt aangeboden richt zich voornamelijk op het verband tussen de ingewikkelde ruimtelijke structuur van de botsende sterrenwinden enerzijds, en de ionisatie van dit gas door de sterren anderzijds. Het uiteindelijke doel van dit werk is het vervaardigen van theoretische 'waarnemingen' om die te vergelijken met de echte, om die zodoende te onderzoeken en te interpreteren. Dit proefschrift heeft niet de pretentie om antwoorden te geven op alle openstaande vragen over het verleden, het gedrag en de toekomst van Eta Carinae. Veel van de stukjes van Eta's puzzel zitten nog in de doos.

Riepilogo
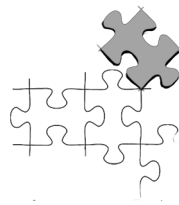
"Navigando" con un telescopio, in una notte stellata, per il cielo dell'emisfero australe può capitate di imbattersi nella 'Carena' (nome di una costellazione) della nave degli Argonauti. Non facendosi distrarre da Canopo, la seconda stella più brillante del cielo, la nostra attenzione verrà catturata dalla 'Nebulosa della Carena', la più brillante della volta celeste. All'interno di questa nebulosa si trova η (eta) Carinae. Eta Carinae è una fra le stelle più massicce e luminose conosciute. Stelle di questa massa terminano la loro vita con spettacolari esplosioni liberando un'altissima quantità di energia. Quando Eta Carinae raggiungerà questo stadio, nella sua evoluzione, sarà probabilmente visibile in pieno giorno e durante la notte si potrà leggere alla sua luce.

Le stelle di grande massa (da decine fino a qualche centinaio di volte la massa del Sole) svolgono un ruolo fondamentale nella storia ed evoluzione dell'Universo. Queste stelle sono la fabbrica dove gli elementi che compongono tutto ciò che ci circonda sono stati e vengono creati. Durante tutta la loro vita arricchiscono il mezzo interstellare (il materiale situato fra le stelle in una galassia) attraverso improvvise eruzioni, potenti venti stellari e, alla fine della loro evoluzione, esplosioni di supernovae. La loro grande massa le rende anche estremamente luminose e calde. I fotoni emessi interagiscono con il miscuglio di gas e polvere circostante che li assorbe e riemette. Queste interazioni modificano le caratteristiche della luce emessa dalle stelle nel suo viaggio fino ai nostri occhi o telescopi. Gli astronomi utilizzano queste informazioni per studiare non solo la sorgente (le stelle), ma anche le caratteristiche del materiale con cui la loro luce ha interagito (gas e polvere). Sfortunatamente le stelle di grande massa sono rare e, a causa della loro maggior luminosità, bruciano il carburante di cui sono composte molto velocemente, avendo quindi una vita di 'solo' qualche decina di milioni di anni. Per questo, nonostante la loro importanza, la nostra conoscenza su come queste stelle si formano ed evolvono resta ancora limitata.

Eta Carinae ha affascinato gli astronomi sin dal 1837 quando la sua luminosità cominciò a variare diventando, in un paio di occasioni, la seconda stella più brillante del cielo notturno. Eta Carinae rimase luminosa per circa un decennio ed in questo straordinario evento, chiamato la 'Grande Eruzione', espulse una considerevole porzione della sua massa
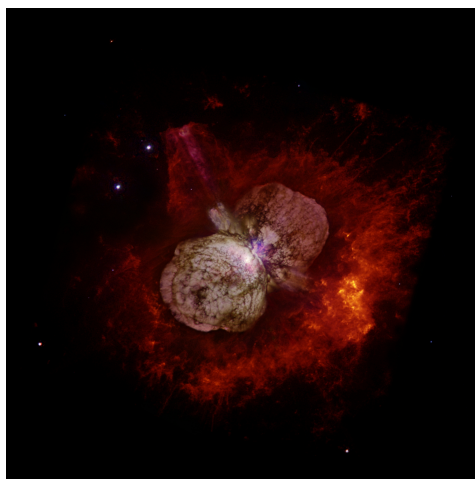
Figura 5.19 – Immagine del Telescopio Spaziale Hubble della nebulosa Homunculus che 'avvolge' Eta Carinae. Crediti: Nathan Smith (University of California, Berkeley), e NASA.

(fra 10–20 masse solari). Tutto questo materiale creò una nebulosa a due lobi conosciuta come 'Homunculus' (vedi Figura 5.19). Questa spettacolare nebulosa se da un lato ha attirato grande attenzione su Eta Carinae, dall'altro ha completamente nascosto al suo interno la stella.

Negli ultimi decenni Eta Carinae è stato uno dei sistemi stellari più osservati della Galassia. I numerosi dati ottenuti sia da osservazioni che da modelli teorici hanno svelato parte dei sui segreti, ma molto ancora resta da spiegare. Uno degli aspetti che rende Eta Carinae interessante, ma allo stesso tempo complessa da studiare, è che non si tratta di una ma di due stelle: quello che viene definito un sistema binario. Una binaria è un sistema in cui due stelle sono legate gravitazionalmente e orbitano una attorno all'altra. In Eta Carinae le orbite percorse dalle due stelle sono ellissi altamente eccentriche. L'eccentricità di un'orbita descrive quanto si discosta da essere circolare. Due posizioni particolari possono essere identificate in un'orbita ellittica. Le due stelle sono ad apoastro quando si trovano alla massima distanza possibile mentre periastro indica il momento in cui sono più vicine.

Entrambe le stelle in Eta Carinae sono estremamente massive (si ipotizza 90 masse solari la primaria η_A e 30 la secondaria η_B) e posseggono forti venti stellari. I venti delle due stelle sono differenti: quello di η_A è molto più denso di quello della compagna η_B che però raggiunge velocità maggiori. I due venti, si espandono indisturbati fino a quando collidono uno contro l'altro. Uno dei principali fattori che definisce la forma della regione in cui i venti interagiscono, è la loro forza (determinata sia dalla loro densità che velocità). Nel caso in cui uno dei due venti prevalga, come in Eta Carinae, questa regione prende una forma quasi conica orientata nella direzione del vento meno potente (vedi Figura 5.20). Il gas, espulso dalle stelle, continua ad accumularsi in questa regione che diventa quindi molto densa e molto calda. Per la maggior parte dei cinque anni e mezzo dell'orbita di Eta

Carinae, questa regione mantiene questa forma quasi conica. Avvicinandosi a periastro, le due stelle non solo si avvicinano tra di loro, ma si muovono anche più rapidamente. La combinazione di questi due effetti modifica in modo significativo le caratteristiche e la forma della regione dove i due venti collidono (vedi Figura 5.21).
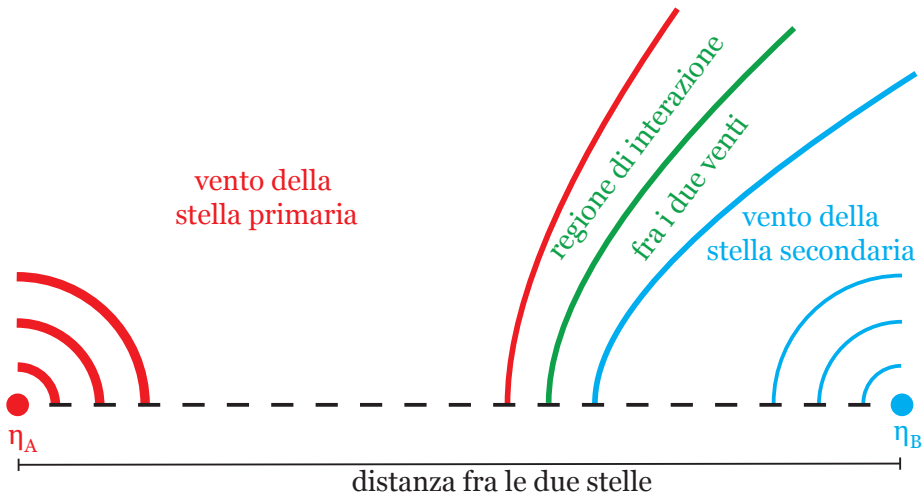

Figura 5.20 – Rappresentazione schematica della collisione dei venti in un sistema binario. La regione di interazione fra i due venti è orientata nella direzione del vento meno potente.
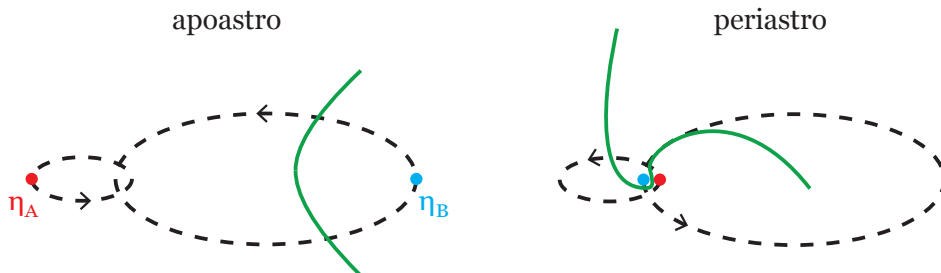
Figura 5.21 – Rappresentazione schematica delle orbite ellittiche delle stelle in un sistema binario. La linea verde mostra la forma della regione di interazione fra i due venti a apoastro e periastro.

Lo studio di sistemi complessi, come ad esempio Eta Carinae, richiede da un lato molteplici ed accurate osservazioni utilizzando telescopi e dall'altro la creazione di modelli attraverso simulazioni numeriche. È in particolare su questo secondo aspetto che questa tesi si concentra. Due sono gli 'attori' principali delle simulazioni discusse in questa tesi: il gas e la radiazione. Il gas (che descrive il contributo dei venti stellari e la loro interazione)

viene considerato come un insieme di particelle che si muovono seguendo le varie leggi dell'idrodinamica. La radiazione prodotta dalle stelle ionizza il gas circostante: i fotoni interagiscono con gli atomi di cui il gas è composto rimuovendo gli elettroni. Per studiare se e dove questo gas è ionizzato, abbiamo preso i risultati di simulazioni tridimensionali della collisione dei venti in Eta Carinae, che ne descrivono la struttura del gas, ed abbiamo 'acceso' le stelle. SimpleX, il codice utilizzato in questa tesi, simula come i fotoni emessi da una stella si propagano ed interagiscono col gas.

Scopo iniziale di questa tesi è di provare l'efficacia di SimpleX nello studiare la ionizzazione del gas in sistemi complessi tipo Eta Carinae (vedi Capitolo 2). La possibilità di creare mappe che mostrino dove il gas viene ionizzato è un tassello fondamentale verso la comprensione delle varie osservazioni. Come accennato in precedenza, la forma, densità e temperatura della regione in cui i due venti stellari interagiscono dipende fortemente dalle loro caratteristiche. Ridurre la densità del vento della stella primaria causa rilevanti differenze nella struttura di questa regione. Queste differenze hanno una diretta ripercussione sul volume di gas che le stelle riescono a ionizzare. Minore la densità del vento di η_A, maggiore il volume di gas ionizzato. Il confronto dei risultati ottenuti numericamente, per differenti valori della densità del vento di η_A, con le informazioni provenienti dalle osservazioni, ci permette di porre un limite minimo alla densità del vento della stella primaria (vedi Capitoli 2 e 3).

I numerosi dati osservativi disponibili su Eta Carinae mostrano notevoli cambiamenti ogni volta che le stelle si trovano vicine a periasto. È soprattutto studiando questa fase dell'orbita che si possono ottenere le maggiori informazioni sulla geometria del sistema e sulle caratteristiche fisiche delle due stelle. Le simulazioni presentate nei Capitoli 3 e 4 investigano la ionizzazione del gas sia ad apoastro che periastro. I risultati ottenuti ci permettono di identificare le possibili cause dei vari dettagli e variazioni nelle osservazioni. Inoltre, la disposizione geometrica delle regioni ionizzate rafforza il modello in cui la secondaria η_B occuperebbe ad apoastro (e quindi per la maggior parte del periodo orbitale) la porzione dell'orbita rivolta verso la Terra.

Le difficoltà connesse con la creazione di modelli di Eta Carinae, non si esauriscono nei dettagli numerici dei codici e delle simulazioni. Visualizzare i complessi risultati di simulazioni tridimensionali è un aspetto altrettanto delicato. Utilizzando una stampante 3D abbiamo creato dei modellini tridimensionali a partire da simulazioni idrodinamiche sulla interazione dei venti di Eta Carinae (vedi Capitolo 5). La capacità di interagire fisicamente con questi modellini crea nuove possibilità per presentare, analizzare e spiegare sia osservazioni che risultati di simulazioni numeriche. Questo aspetto assume un particolare rilievo nella comunicazione con un pubblico non esperto.

In questi anni più di una volta mi è stato chiesto: "Perchè studiare Eta Carinae?". Tralasciando per un momento le motivazioni prettamente scientifiche, penso la risposta possa essere conoscenza e curiosità. È quella spinta, quel desiderio e quella soddisfazione, insiti nell'animo umano, di aggiungere anche una sola tessera ad un puzzle non completato. Sul piano scientifico, Eta Carinae, per la sua vicinanza e gli ottimi dati osservativi disponibili, rappresenta un perfetto laboratorio per studiare numerosi aspetti riguardanti la formazione

ed evoluzione di stelle di grande massa. In modo particolare le varie interazioni fra le due stelle in una binaria, sono considerate alla base di numerosi importanti, ma non ancora completamente compresi, fenomeni astronomici.

Il lavoro presentato in questa tesi si focalizza principalmente sul rapporto fra la complessa struttura geometrica dovuta all'interazione dei venti stellari e la ionizzazione di questo gas da parte delle due stelle. Il fine ultimo di questo lavoro è la creazione di osservazioni sintetiche che confrontate con quelle reali possano aiutarci a interpretarle e spiegarle. Questa tesi non ha la pretesa di rispondere alle numerose domande ancora aperte riguardanti la storia, il comportamento ed il futuro di Eta Carinae. Molti dei pezzi del suo puzzle sono ancora nella scatola.

Dedicato ai miei fratelli, soprattutto a quello che:
"Se non posso diventare uno scienziato,
posso vedere le cose piccole,
prendo i libri e guardo le figure
delle particelle, degli animali, pulci e pidocchi."

Pubblications
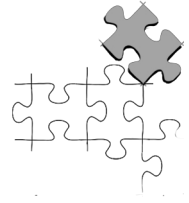
1. *3D radiative transfer in η Carinae: application of the* SIMPLEX *algorithm to 3D SPH simulations of binary colliding winds*
   N. Clementel, T. I. Madura, C. J. H. Kruip, V. Icke and T. R. Gull
   2014, MNRAS, 443, 2475

2. *3D radiative transfer simulations of Eta Carinae's inner colliding winds – I: Ionization structure of helium at apastron*
   N. Clementel, T. I. Madura, C. J. H. Kruip, J.-P. Paardekooper and T. R. Gull
   accepted for publication in MNRAS

3. *3D radiative transfer simulations of Eta Carinae's inner colliding winds – II: Ionization structure of helium at periastron*
   N. Clementel, T. I. Madura, C. J. H. Kruip and J.-P. Paardekooper
   submitted to MNRAS

4. *3D printing meets computational astrophysics: deciphering the structure of η Carinae's inner colliding winds*
   T. I. Madura, **N. Clementel**, T. R. Gull, C. J. H. Kruip and J.-P. Paardekooper
   submitted to MNRAS

Curriculum Vitae
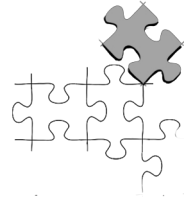
I was born on April 16, 1984 in Tosamaganga, in the middle of Tanzania. I grew up in Sammartini in the countryside around Crevalcore, a small town north of Bologna (Italy). Since the beginning of my education, I discovered that I was particularly interested in science, especially physics and math. It was therefore easy to decide to go to a science-oriented lyceum (Liceo Scientifico Archimede) in San Giovanni in Persiceto.

It was only at the end of high school that I started thinking about astronomy as a follow up of my study. As a result, in 2003, I began the Bachelor (Laurea Trienniale) in Astronomy at Università di Bologna. In December 2006 I graduated with a research project on sub-Eddington low opacity accretion disk model (ADAF) with prof. Luca Ciotti. I continued my study with the Master (Laurea Specialistica) in Astrophysics and Cosmology at the same university. During the last year of my Master, I received an offer for a PhD at Leiden University. As a consequence, in order to speed up both processes, I started working on the topic of the future PhD work for my Master thesis with prof. Vincent Icke and prof. Filippo Fraternali. In December 2009 I defended my thesis on hydrodynamical simulations of the extreme binary star Eta Carinae, and received my Master degree.

Shortly thereafter, in January 2010, I started my PhD at Leiden Observatory, in the Netherlands under the supervision of Prof. Vincent Icke. I continued on my Master thesis topic studying, at the beginning, the hydrodynamics of the colliding wind binary Eta Carinae with different grid-based hydrodynamic codes. In 2012 I started my collaboration with dr. Thomas Madura and dr. Theodore Gull and focused my research on radiative transfer processes. I applied the SimpleX radiative transfer algorithm to 3D SPH simulations of Eta Carinae colliding winds studying the ionization of the gas due to the two powerful stars. During my PhD, I presented my work to international conferences in the Netherlands, United States, Greece, and Mexico.

In the spring 2015, I will move to Cape Town (South Africa) to start a Postdoctoral Research Fellowship at the South African Astronomical Observatory. I will work in collaboration with dr. Shazrene Mohamed on stellar outflows and mass transfer in binary stars.

Acknowledgments
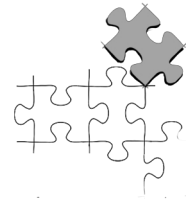
It looks like yesterday, and at the same time another life, when I started this PhD without thinking and knowing what there was between me and this moment. But as every path, this one also had its beginning and, through detours up- and downhill, reached its end. From before all of this started, and also in these years, I did not go through places, experiences, and sometimes the simple passing of time alone. Many have shared with me the good, the bad and the ugly of this experience. I am here facing the hard task to remember them and the part they played, even if simple yet important, and properly thank them.

Starting with the ones more directly connected with this thesis, a special thanks goes to Tom. All of this would not have been possible without your support, help, patience and guidance. Among my collaborators, I'm expecially thankful to Chael, even if you left academia you are still putting energy and time into something you still like. Ted, you gave me a friendly welcome in the Eta Carinae community five years ago, and since then you have always been helpful and supporting. Jan-Pieter: thanks for your availability, and your constructive comments.

Ringrazio i tanti amici lasciati in italia, compagni di studi, viaggi ed avventure che mi hanno portato ad essere qui oggi. Non è stato sempre facile mantenere i contatti in questi anni, ma è sempre un piacere una chiamata su Skype o il reincontrarsi. I was also lucky to meet a lot of new friends in these years in the Netherlands. Alex, Andra, Anna, Carl, Clemént, Cristobal, Carina, Daan, Dan, Elisabetta, Emanuele, Ernst, Francisco, Geiske, Gleb, Heather, Jaya, Jayne, Julia, Kalle, Magnus, Marissa, Mihaela, Monica, Pedro, Sebastian, Steven, Tiffany, Vachail, thanks for the time spent together and the chat during coffee and lunch breaks, borrels, and parties. Mher, Maria, Darko, Alessandro, we shared the house, dinners, and bottles of wine. The physicists crowd for the nice time around green tables, in the afternoon with cues, balls, and beers and in the evening with cards, chips, and whisky. Rafa: the first person I remember from the Observatory, it is always nice to meet you and Lara. Franco per avermi introdotto all'arrampicata. Elena per il tempo passato assieme, fra Leiden, Rotterdam e Groningen e l'aiuto con la parte 'Dutch' di